

TECHNISCHE
UNIVERSITÄT
DRESDEN

Equivalence of Kitaev physics for extended models on the harmonic honeycomb lattices

Master-Arbeit
zur Erlangung des Hochschulgrades
Master of Science
im Master-Studiengang Physik

vorgelegt von

WILHELM G. F. KRÜGER
geboren am 30.01.1996 in BAD SAAROW-PIESKOW

Institut für Theoretische Physik
Fachrichtung Physik
Fakultät Mathematik und Naturwissenschaften
Technische Universität Dresden
2019

Eingereicht am 18. Oktober 2019

1. Gutachter: Prof. Dr. Matthias Vojta
2. Gutachter: Prof. Dr. Carsten Timm

Abstract

Abstract

In this master thesis, we study the Heisenberg-Kitaev model on the three-dimensional hyperhoneycomb lattice in a magnetic field for different field directions and also in the presence of an off-diagonal symmetric Γ term. For the model in the field, large parts of the phase diagrams agree exactly with the corresponding phase diagrams for the planar honeycomb model. The hyperhoneycomb lattice and corresponding models can be projected to the honeycomb lattice. Classical states are compatible with the projection if their ordering wave-vectors lie in the crystallographic ac -plane. Note that the energetics of these states is the same in 3D and 2D since both lattices are tri-coordinated. On the other hand, the Heisenberg-Kitaev- Γ model on the hyperhoneycomb lattice is projected to a honeycomb model, which breaks the honeycomb C_3 rotation symmetry. However, the projected and original honeycomb models are equivalent in the limit of a small Heisenberg coupling due to the presence of a duality transformation. This may explain the similar experimentally observed magnetic structures of α - Li_2IrO_3 and β - Li_2IrO_3 . Although the projection is well defined only in the classical limit, the 3D-2D equivalence holds also for the magnon spectrum obtained by linear spin-wave theory. But quantum corrections generally differ in 3D and 2D due to the different phase space. However, the equivalence is qualitative, since observables like the energy and the magnetization are functions of the model parameter, which have the same form in 3D and 2D. The advertised 3D-2D mapping can be generalized to the so-called harmonic-honeycomb series which includes the hyperhoneycomb lattice. Our results provide an easier access to the physics of three-dimensional Kitaev systems.

Zusammenfassung

Im Rahmen dieser Masterarbeit untersuchen wir das Heisenberg-Kitaev Modell auf dem Hyperhonigwabengitter, zum einen in einem externen Magnetfeld für verschiedene Feldrichtungen und zum anderen mit einem symmetrischen Γ term. Für das Modell im Feld stimmen große Teile der Phasendiagramme mit den entsprechenden Phasendiagrammen für das planare Honigwabengitter exakt überein. Das Hyperhonigwabengitter und entsprechende Modelle können auf das Honigwabengitter projiziert werden. Dabei sind klassische Zustände kompatibel mit der Projektion, wenn ihre Ordnungswellenvektoren in der kristallographischen ac Ebene liegen. Die Energien der Zustände in drei und zwei Dimensionen sind zudem gleich, da beide Gitter die Koordinationszahl drei haben. Andererseits wird das Heisenberg-Kitaev- Γ Modell auf ein Honigwabengitter abgebildet das die C_3 -Rotationssymmetrie bricht. Jedoch existiert im Limes kleiner Heisenberg Kopplung eine Dualitätstransformation, die das projizierte Modell auf das originale Honigwabengitter abbildet. Diese kann erklären, warum die experimentell ermittelten magnetischen Strukturen von α - Li_2IrO_3 und β - Li_2IrO_3 ähnlich sind. Obwohl die Projektion nur im klassischen Limes klar definiert ist, gilt die 3D-2D Äquivalenz auch für das Magnonenspektrum in linearer Spinwellentheorie. Allerdings sind wegen des unterschiedlichen Phasenraums die Quantenkorrekturen in drei und zwei Dimensionen im Allgemeinen verschieden. Da die Energie und die Magnetisierung als Funktion des Modellparameters die selbe Form in drei und zwei Dimensionen haben, ist die Äquivalenz jedoch qualitativ. Die beschriebene 3D-2D Projektion kann auf die sogenannten harmonischen Honigwabengitter verallgemeinert werden. Unsere Resultate liefern einen einfacheren Zugang zur Physik von dreidimensionalen Kitaev Systemen.

Contents

Main Part	3
1 Introduction and motivation	3
1.1 Magnetism and frustration	3
1.2 Kitaev honeycomb model and spin liquids	4
1.3 Real Kitaev materials	5
1.4 Conventions	6
2 Heisenberg-Kitaev model on the hyperhoneycomb lattice in a magnetic field	7
2.1 The hyperhoneycomb lattice	7
2.2 Heisenberg-Kitaev model	9
2.3 Heisenberg-Kitaev model in an external field	12
2.4 Spin-wave theory	12
2.5 Phases and classical phase diagram	14
2.5.1 [1, 0, 0], [0, 1, 0], and [0, 0, 1] directions	14
2.5.2 [1, 1, 1] direction	16
3 3D-2D equivalence of models and ordered states	21
3.1 Projection of the hyperhoneycomb model to a honeycomb model	21
3.1.1 Projection of the lattice	21
3.1.2 Projection of states	23
3.1.3 Projection of the magnon spectrum	23
3.2 Extended models	26
3.2.1 Beyond nearest neighbors	26
3.2.2 Heisenberg-Kitaev- Γ model	26
3.2.3 Duality transformation for the projected model	27
3.3 Harmonic honeycombs	28
3.4 1D Kitaev systems	30
4 Heisenberg-Kitaev- Γ model on the hyperhoneycomb and projected lattices	32
4.1 Methods	32
4.2 Phases and phase diagrams	33
4.3 Relation to the honeycomb model	35
4.3.1 The $J \rightarrow 0$ limit	37
4.3.2 The Heisenberg point $K = \Gamma$, $J = 0$	39
4.3.3 Experimental results	41
5 Quantum corrections in 3D and 2D	43
5.1 Energy corrections	43
5.2 Magnetization	48
5.2.1 Heisenberg-Kitaev phases	49
5.2.2 High-field phase	50

Appendix	53
A Spin-wave theory	53
A.1 High-field/polarized phase	53
A.2 Néel phase	57
B Analytical parametrization of the magnetic unit cell	59
C Luttinger-Tisza Approach	61
D Single-Q ansatz	64
Bibliography	67
Acknowledgment	69

Main Part

1 Introduction and motivation

In this master thesis, we study the Heisenberg-Kitaev model on the hyperhoneycomb lattice, on the one hand in an external magnetic field and on the other hand an extended model. The considered models belong to an actual research field of frustrated magnetism in theoretical physics. They are of theoretical and experimental interest since for these kind of models so-called spin liquids can be realized. This introduction gives a physical motivation for the considered model and a brief overview of (frustrated) magnetism, Kitaev physics and spin liquids.

1.1 Magnetism and frustration

Maxwells equations postulate that magnetic fields are created by charge currents. But magnetic phenomenas also occur for solid states without an electric current. The Bohr-van Leeuwen theorem states, that it is not possible to describe ferromagnetism in a classical theory for which currents are the only reason of magnetic fields. With the beginning of quantum mechanics, the electron spin has been discovered, which is an intrinsic angular momentum $\hbar/2$. Since electrons carry a charge, the spin corresponds to a magnetic moment. For a many-body electronic problem, there occurs a quantum mechanical exchange interaction next to the Coulomb interaction. This exchange interaction can generate effective spin-spin interactions.

Werner Heisenberg has shown, that a quantum mechanical description can in principle explain ferromagnetism for elementar compounds [1]. In the presence of an exchange integral, the spin of an electron can interact with the spin of a neighbored electron. This can be modeled by the so-called Heisenberg model on a lattice

$$\mathcal{H}_H = \frac{1}{2} \sum_{i,j} J_{ij} \vec{S}_i \cdot \vec{S}_j, \quad (1.1)$$

where \vec{S}_i denotes the spin at lattice site i and J_{ij} is a coupling constant which is proportional to the quantum mechanical exchange integral. The factor $1/2$ is a convention due to double counting. Since the coupling J_{ij} typically decreases exponentially with the distance of the two spins, it is sufficient to consider only nearest-neighbor interaction as a first approximation. However, second- and third-nearest-neighbor interactions may also be important for some models. Each spin can be represented by the three operators S^x , S^y , and S^z , which satisfy the commutation relation of angular momenta $[S^k, S^l] = i\varepsilon_{klm} S^m$, with the antisymmetric Levi-Civita symbol ε_{klm} . In the classical limit, the the commutator vanishes and the spins are just normal three-component vectors.

For a nearest-neighbor Heisenberg model, the couplings are usually assumed to be equal, i.e., $J_{ij} = J$ for all pairs of nearest neighbors i, j . This choice of couplings is valid by symmetry reasons for some types of lattices, e.g., the square lattice or the simple cubic lattice. For a ferromagnetic Heisenberg model ($J < 0$), all spins point in the same direction which is the so-called ferromagnetic state. One can show that the ferromagnetic state is also an eigenstate of the Heisenberg model in the quantum case. Since this state simultaneously breaks the SU(2) symmetry of the model, there is a gapless Goldstone mode in the excitation spectrum. On the other hand, a classical antiferromagnetic Heisenberg model ($J > 0$) on a bipartite lattice has the Néel state as the ground state, i.e., neighbored spins are aligned antiparallel. Since the Néel state is not an eigenstate of the

corresponding Hamilton operator, quantum fluctuations may destroy it. Typically, a singlet state is formed for low-dimensional lattices.

When not all interaction terms can be simultaneously minimized, then the magnetic ground state is apart from a conventional Heisenberg ferromagnet or antiferromagnet. This phenomena is called frustration and leads to complicated magnetic orders or topological features. The simplest example is the antiferromagnetic Heisenberg model on the triangular lattice, as displayed in Fig. 1.1 (a). Inside a triangle, two spins can be chosen antiparallel, but the third spin cannot be antiparallel to the former ones. The real ground state is a 120° phase [2] where neighbored spins have a relative angle of 120° . This is an example of geometric frustration because the absence of the Néel phase is due to the lattice geometry.

On the other hand, frustration also occurs in the presence of concurring interactions. Considering a Heisenberg model on the square lattice, which has a nearest-neighbor coupling $J_1 > 0$ and a second-nearest-neighbor coupling $J_2 > 0$. A spin state which minimizes the energy concerning J_1 has parallel second-nearest neighbors, what is energetically unfavorable for J_2 . The ground state is a spiral with an ordering wave-vector that depends on the ratio J_2/J_1 .

In the presence of a magnetic field, frustration leads to the presence of novel phases. Since many different states are nearly degenerate for such systems, it needs complex numerical methods to determine the exact ground state such as large-scale Monte-Carlo simulations. Despite this complication, frustrated systems are subject of current research because these novel phases may have interesting topological features.

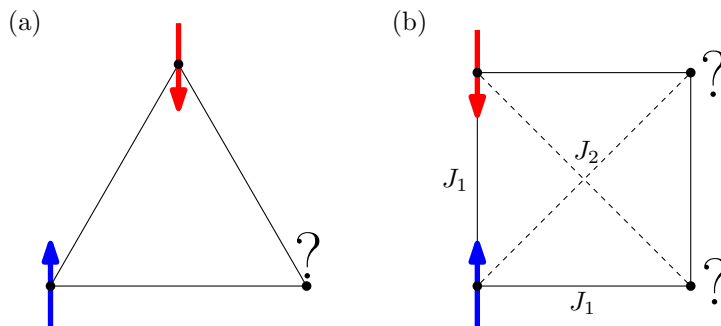


Figure 1.1: Frustration for different models. (a) For an antiferromagnetic Heisenberg model on a triangle, an antiparallel alignment of the spins is preferred, but this can be not done for all three spins simultaneously. (b) For a square lattice model with nearest- and second-nearest-neighbor couplings $J_1 > 0$ and $J_2 > 0$, respectively, J_1 prefers a parallel arrangement of second-nearest neighboring spins while J_2 prefers antiferromagnetic alignment.

1.2 Kitaev honeycomb model and spin liquids

In 2006, Alexei Kitaev showed an exact solution for an Ising-type $S = 1/2$ spin model on the planar honeycomb lattice [3], which is illustrated in Fig. 1.2 (a). There are three types of bonds dubbed x , y and z bonds. Two spins \vec{S}_i and \vec{S}_j which are distinct by an x bond have an interaction of the form $S_i^x S_j^x$ while pairs of spins on the y and z bonds have an interaction of the form $S_i^y S_j^y$ and $S_i^z S_j^z$, respectively. Thus, the Hamilton operator has the form

$$\mathcal{H}_K = \sum_{\langle ij \rangle_\gamma} K^\gamma S_i^\gamma S_j^\gamma, \quad (1.2)$$

where $\langle ij \rangle$ denotes the summation over pairs of nearest neighbors and $\gamma = x, y, z$. Note that the coupling constant K^γ can be different for the x , y and z bonds and may be positive or negative. This model can be solved by representing the spin operators by Majorana fermions. The corresponding fermion spectrum is

gapless if K^x , K^y , and K^z satisfy the triangle inequality

$$|K^x| \leq |K^y| + |K^z|, \quad (1.3)$$

and cyclic permutations of it. The corresponding gapless phase is dubbed B in the phases diagram, which is displayed in Fig. 1.2 (b). The B phase has a \mathbb{Z}_2 gauge field. On the other hand, if Equation (1.3) is not fulfilled, the excitation spectrum has a gap. The gapped phases A_x , A_y , and A_z occur for dominant K^x , K^y , and K^z , respectively, and they are related to each other by the rotation symmetry. The Kitaev honeycomb model is one of the rare examples of a quantum many-body problem that can be solved exactly.

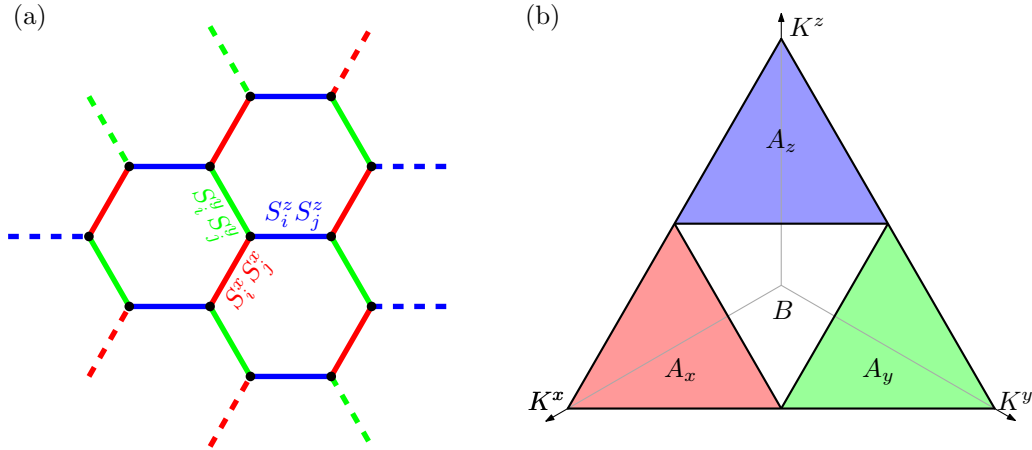


Figure 1.2: (a) The Kitaev honeycomb model with three types of bond interactions. (b) The phase diagram of the Kitaev model. The triangle represents a cross-section with $K^x + K^y + K^z = \text{const.}$ in the positive octant.

The ground state of the Kitaev spin-1/2 honeycomb model is a so-called quantum spin liquid. Such a spin liquid can be described by a resonant valence bound state [4]. Two neighbored spins can form a singlet state, i.e., they form an antisymmetric state $|0\rangle = \frac{1}{\sqrt{2}}(|\uparrow\downarrow\rangle - |\downarrow\uparrow\rangle)$. For a valence bound state, every spin is bound in a singlet state. A different order of the singlets leads to the same energy. Thus, the quantum mechanical ground state is a superposition of all possible valence bound states. This state is dubbed resonating valence bound state.

Conventional magnets have $S = 1$ excitations, which are shown as sharp peaks in the energy in scattering experiments. However, for a resonant valence bound state the $S = 1$ excitation is fractionalized into a pair of $S = 1/2$ quasiparticles, called spinons [5]. This can be understood, as a singlet breaks into two distinct parallel spins. Spinons lead to a continuum of excitations and they have a fractional quantum number.

1.3 Real Kitaev materials

Anisotropic spin interactions like the Kitaev interaction can be present in materials which have both, strong electronic correlations and strong spin-orbit coupling. In an interesting work by George Jackeli and Giniyat Khaliullin [6], they showed a mechanism that generates spin-exchange interaction of the Kitaev type. The material must consist of transition metals in a d^5 configuration such as Ir^{4+} ($5d^5$) or Ru^{3+} ($4d^5$), which are surrounded by ligand ions in an octahedral environment. For instance, in the material Na_2IrO_3 , each Ir^{4+} ion is surrounded by six O^{2-} ions which form an octahedron. In the presence of the octahedral crystal field, the d^5 orbital is splitted into a t_{2g} and an e_g state, see Fig. 1.3. The five electrons fill the lower t_{2g} orbital, which has an effective $l = 1$ orbital moment, up to one hole. When spin-orbit coupling is strong, the t_{2g} state is splitted into a lower $j_{\text{eff}} = 3/2$ and an upper $j_{\text{eff}} = 1/2$ state. In the presence of strong electronic correlations, this leads to a $j = 1/2$ Mott insulator [7, 8].

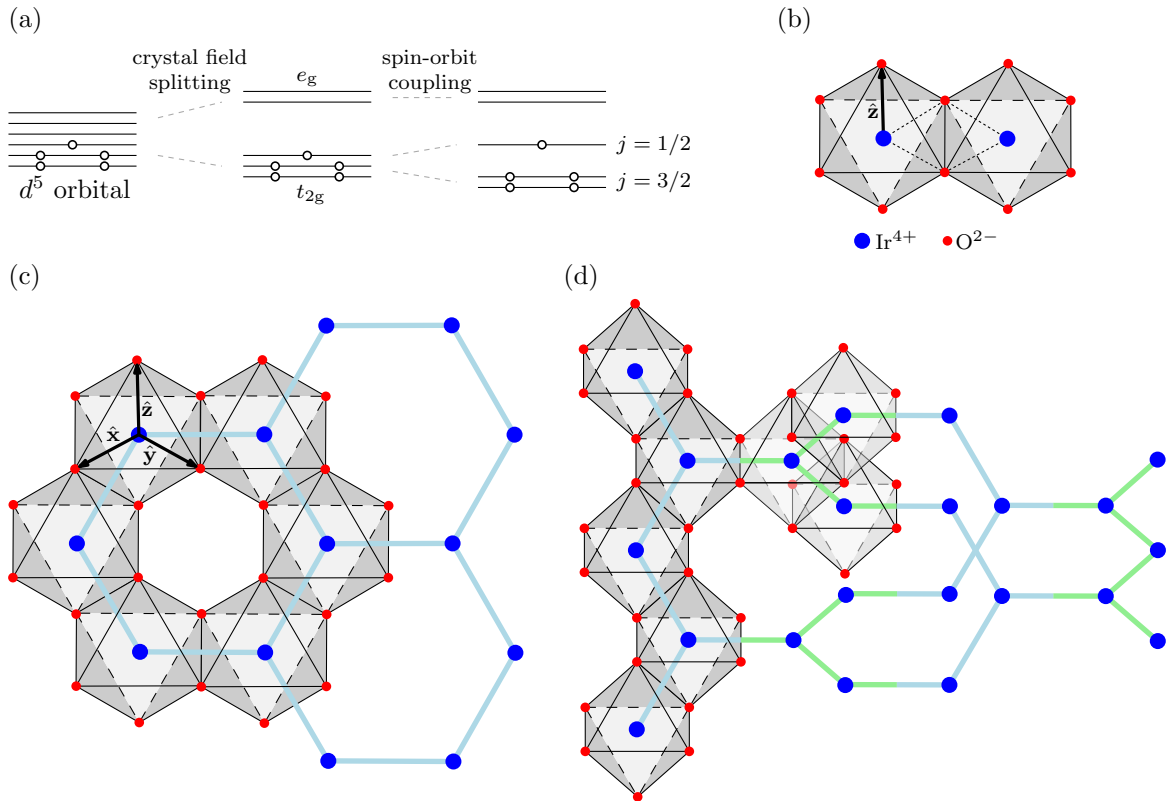


Figure 1.3: (a) In the presence of an octahedral crystal field splitting and strong spin-orbit coupling, a d^5 electronic configuration is transferred to a state which has effectively a spin-1/2 degree of freedom. (b) For a bond-sharing octahedral structure, the two exchange paths between the Ir^{4+} ions along the O^{2-} ions, denoted by the finely dashed lines, lead to a Kitaev coupling of the type $S_i^z S_j^z$, if the exchange paths are in the plane perpendicular to the z axis. Such an octahedral structure is realized in the honeycomb iridate $\alpha\text{-Li}_2\text{IrO}_3$ (c) and in the hyperhoneycomb iridate $\beta\text{-Li}_2\text{IrO}_3$ (d). The Li^+ ions are not shown in the plots. The panels are reproduced from Reference [7].

Jackeli and Khaliullin showed, that the Kitaev type interaction occurs in the leading order of a strong-coupling expansion if neighbored octahedra share bonds, as illustrated in Fig. 1.3 (b). There are two exchange paths between neighboring Ir^{4+} ions along two different O^{2-} ions. This generates an Ising-like coupling, with an Ising axis that is perpendicular to the exchange paths.

This octahedral structure is realized in materials like RuCl_3 [9], Na_2IrO_3 [10], and $\alpha\text{-Li}_2\text{IrO}_3$ [11], where the transition-metal ions form a planar honeycomb structure, as displayed in Fig. 1.3 (c). However, there are also real three-dimensional Kitaev materials like the hyperhoneycomb lattice $\beta\text{-Li}_2\text{IrO}_3$ [12], see Fig. 1.3 (d), or the stripyhoneycomb lattice $\gamma\text{-Li}_2\text{IrO}_3$ [13]. Thus, they are candidates for realizing a Kitaev spin liquid.

There are a lot of experimental and theoretical studies on the planar honeycomb Kitaev system, for extended models and also the magnetic field response [14]. On the other hand, there are a few works on the three-dimensional Kitaev materials [15–22].

1.4 Conventions

In the following, we study the Kitaev model on the hyperhoneycomb lattice in the presence of a Heisenberg coupling for a finite magnetic field and a symmetric off-diagonal Γ interaction, respectively. Since we consider a model which contains spins, we set $\hbar = 1$ for simplicity and include the Landé g -factor in the magnetic field strength. The numerical calculations for minimization, integration, and matrix diagonalization have been done with Wolfram Mathematica using the standard numerical methods. Further, bonds which contain the Kitaev interaction of the form $S_i^x S_j^x$, $S_i^y S_j^y$, and $S_i^z S_j^z$ are marked in the following in red, green, and blue, respectively.

2 Heisenberg-Kitaev model on the hyperhoneycomb lattice in a magnetic field

In this section, we introduce the hyperhoneycomb lattice and study the corresponding Heisenberg-Kitaev model in an external magnetic field for different field directions.

2.1 The hyperhoneycomb lattice

The hyperhoneycomb lattice is part of the so-called harmonic honeycomb series [19, 23]. The nearest-neighbor bonds form open honeycomb plaquettes in a three-dimensional formation. We can choose a primitive unit cell with a four-sublattice structure or a conventional orthorhombic unit cell with 16 sites, see Fig. 2.1. There exist three C_2 symmetry transformations with axes at the center of the blue bonds in the hyperhoneycomb lattice, i.e., the lattice remains invariant under a 180° rotation about an axis parallel to one of the crystallographic \mathbf{a} , \mathbf{b} and \mathbf{c} axes denoted as C_a , C_b , and C_c , respectively. The transformations C_a and C_b interchange sublattices A and B (short notation: A-B) and C-D, respectively, while C_c does not interchange the sublattices. There exists also an inversion symmetry with the inversion center corresponding to the center of the red and green bonds, which exchanges A-D and B-C.

The hyperhoneycomb lattice is characterized by the three primitive lattice vectors

$$\mathbf{a}_1 = [2, 4, 0], \quad \mathbf{a}_2 = [3, 3, 2], \quad \mathbf{a}_3 = [-1, 1, 2], \quad (2.1)$$

and the sublattice positions

$$\mathbf{R}_A = [0, 0, 0], \quad \mathbf{R}_B = [1, 1, 0], \quad \mathbf{R}_C = [1, 2, 1], \quad \mathbf{R}_D = [2, 3, 1], \quad (2.2)$$

where $[\dots]$ denotes the notation in the $[\hat{\mathbf{x}}, \hat{\mathbf{y}}, \hat{\mathbf{z}}]$ basis defined in Fig. 2.1. There are five types of different nearest-neighbor bonds

$$\delta_1 = [0, 1, 1], \quad \delta_2 = [1, 0, -1], \quad \delta_3 = [-1, -1, 0], \quad \delta_4 = [0, 1, -1], \quad \delta_5 = [1, 0, 1], \quad (2.3)$$

where δ_1 (δ_2) connects B-C, δ_3 connects A-B and C-D and δ_4 (δ_5) connects A-D. Alternatively, the lattice is given by the conventional orthorhombic lattice vectors

$$\mathbf{a} = [6, 6, 0], \quad \mathbf{b} = [0, 0, 4], \quad \mathbf{c} = [-2, 2, 0]. \quad (2.4)$$

The corresponding reciprocal lattice is body-centered orthorhombic with

$$\mathbf{a}^* = [-\pi, \pi, 0], \quad \mathbf{b}^* = [0, 0, \pi], \quad \mathbf{c}^* = \left[\frac{\pi}{3}, \frac{\pi}{3}, 0\right]. \quad (2.5)$$

The Brillouin zone of the hyperhoneycomb lattice is illustrated in Fig. 2.2 with the corresponding high-symmetry points. The reciprocal lattice vectors are given by

$$\begin{aligned} \mathbf{b}_1 &= \left[\frac{\pi}{3}, -\frac{2\pi}{3}, \frac{\pi}{2}\right] = \left(-\frac{1}{2}, \frac{1}{2}, -\frac{1}{2}\right), \\ \mathbf{b}_2 &= \left[-\frac{2\pi}{3}, \frac{\pi}{3}, \frac{\pi}{2}\right] = \left(\frac{1}{2}, -\frac{1}{2}, -\frac{1}{2}\right), \\ \mathbf{b}_3 &= \left[\frac{2\pi}{3}, -\frac{\pi}{3}, -\frac{\pi}{2}\right] = \left(-\frac{1}{2}, -\frac{1}{2}, \frac{1}{2}\right), \end{aligned} \quad (2.6)$$

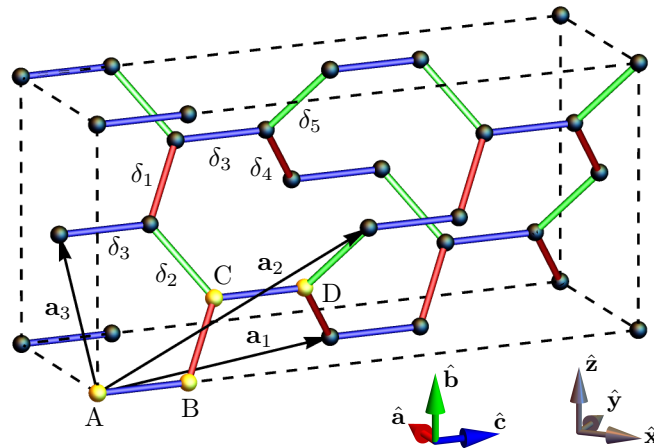


Figure 2.1: The hyperhoneycomb lattice in a face-centered orthorhombic unit cell. Red, green, and blue bonds belong to x , y , and z bonds, respectively. The yellow sites mark the 4 sublattices inside the primitive unit cell while $\delta_1, \dots, \delta_5$ denote the different nearest-neighbor bonds.

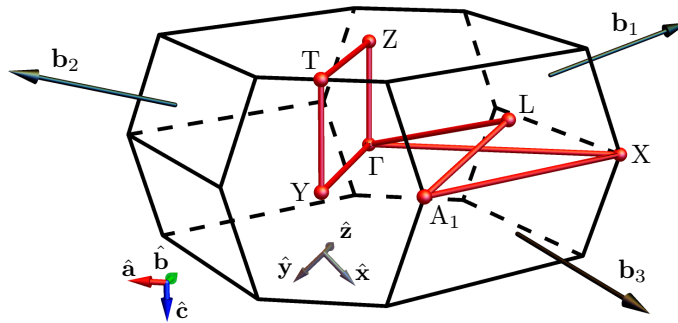


Figure 2.2: Brillouin zone of the hyperhoneycomb lattice with the reciprocal lattice vectors $\mathbf{b}_1, \mathbf{b}_2, \mathbf{b}_3$ and the high-symmetry points $\Gamma = (0, 0, 0)$, $\mathbf{Y} = (0, -\frac{1}{2}, 0)$, $\mathbf{T} = (0, -\frac{1}{2}, -\frac{1}{2})$, $\mathbf{Z} = (0, 0, -\frac{1}{2})$, $\mathbf{X} = (-\frac{29}{72}, 0, 0)$, $\mathbf{X} = (-\frac{11}{72}, -\frac{1}{2}, 0)$, and $\mathbf{L} = (-\frac{1}{4}, -\frac{1}{4}, -\frac{1}{4})$. The red line corresponds to a path along high-symmetry points, which is typically used to show magnon spectra in the following.

where (...) marks the notation in the crystallographic $\{\mathbf{a}^*, \mathbf{b}^*, \mathbf{c}^*\}$ basis. In the following, we will mainly use the $(\mathbf{a}^*, \mathbf{b}^*, \mathbf{c}^*)$ notation to indicate wave-vectors.

The hyperhoneycomb lattice is realized, for instance, in $\beta\text{-Li}_2\text{IrO}_3$ [12, 24]. Here, each Ir^{4+} ion is surrounded by six O^{2-} ions in an octahedral environment. Due to the crystal field splitting and strong spin-orbit coupling, the Ir^{4+} ions have an effective $j_{\text{eff}} = \frac{1}{2}$ degree of freedom. Neighboring octahedra share edges. This geometry leads to an effective spin exchange coupling of the Kitaev type via the Jackeli-Khaliullin mechanism [6]. Since the O^{2-} and Li^+ ions are nonmagnetic, the corresponding magnetic lattice is the hyperhoneycomb lattice.

The experimentally observed crystal structure of $\beta\text{-Li}_2\text{IrO}_3$ deviates from the ideal hyperhoneycomb structure [24]. The orthorhombic lattice constants are $a = 5.9104(3)$ Å, $b = 8.4562(4)$ Å, and $c = 17.8271(9)$ Å. The length of the x and y bonds is found to be 2.9729 Å while the length of the z bonds is 2.9784 Å, which means a difference of around 0.2% in the bond length. Also the angle between the bonds differ from the ideal 120° structure: The angle between the x and y bonds is 120.4° , while the angle between the z and x (y) bonds is 119.8° . These experimental results suggest that the x and y bonds are symmetry connected also in the real material $\beta\text{-Li}_2\text{IrO}_3$.

2.2 Heisenberg-Kitaev model

The hyperhoneycomb lattice is tri-coordinated, so we can define a Kitaev model [15] analogous to that one for the honeycomb lattice with the Kitaev Hamiltonian

$$\mathcal{H}_K = \sum_{\langle ij \rangle_\gamma} K^\gamma S_i^\gamma S_j^\gamma, \quad (2.7)$$

where K^γ is the bond dependent Kitaev coupling, $\gamma = x, y, z$ and $\langle ij \rangle_\gamma$ denotes pairs of nearest neighbors. The x , y , and z bonds on the hyperhoneycomb lattice are defined in Fig. 2.1 and are marked in the following in red, green, and blue, respectively. Unlike the honeycomb lattice, the bonds on the hyperhoneycomb lattice are not all symmetry equivalent even in the idealized lattice structure. We can define two types of pairwise parallel x (y) bonds, while all z bonds are parallel. The lattice symmetry operations C_a and C_c interchange the x and y bonds. When the C_a and C_c rotation is also applied in the spin space, then the $S_i^x S_j^x$ and $S_i^y S_j^y$ interactions are also interchanged, and the model remains invariant under this combined lattice-spin-space rotation. This ensures that the Kitaev couplings on the x and y bonds must be equal. However, the z bonds are not connected to the other types of bonds by symmetry transformations. Nevertheless, inversion symmetry ensures that the two z bonds inside the primitive unit cell have the same coupling strength.

Typically, superexchange interactions generate more terms in the Hamiltonian. An important one is the Heisenberg interaction which is of the form $\vec{S}_i \cdot \vec{S}_j$. Now we can define the Heisenberg-Kitaev model on the hyperhoneycomb lattice

$$\mathcal{H}_{HK} = J \sum_{\langle ij \rangle} \vec{S}_i \cdot \vec{S}_j + 2K \sum_{\langle ij \rangle_\gamma} S_i^\gamma S_j^\gamma. \quad (2.8)$$

Here, J is the strength of the Heisenberg coupling. Note that the factor 2 in front of the Kitaev term is a convention for the pure Heisenberg-Kitaev Hamiltonian, but not for extended models. The Kitaev coupling K is chosen to be equal on each bond. The couplings can be parametrized as $J = A \cos \varphi$ and $K = A \sin \varphi$, where $A > 0$ is an overall energy scale. The classical Heisenberg-Kitaev model on the hyperhoneycomb lattice has been studied before [15] and the phase diagram agrees exactly with that for the Heisenberg-Kitaev model on the honeycomb lattice, see Fig. 2.3. The corresponding phases are found as the exact ground state by the Luttinger-Tisza approach, a detailed explanation of this method is given in Appendix C.

The classical phase diagram contains four ordered states, the Néel, ferromagnetic (FM), zigzag, and stripy phases. The Néel and FM phases are present in parameter regions where all couplings are antiferromagnetic (AF) and FM, respectively, or where the Heisenberg term is the dominant coupling.

The zigzag phase is defined in the following. In the x zigzag phase, all x bonds are AF while the y and z bonds are FM. For the Heisenberg-Kitaev model, the spins are aligned in the $\pm \vec{e}_x$ directions. The resulting zigzag chain along the y and z bonds does not lie in a plane because the z bond connects the two types of pairwise not parallel y bonds as displayed in Fig. 2.4 (a), so the phase is denoted as x skew-zigzag. Similarly, the y skew-zigzag phase is defined by AF y bonds and FM x , z bonds, where spins are aligned in the $\pm \vec{e}_y$ directions in the Heisenberg-Kitaev limit. There exists also a z zigzag phase with AF z bonds what is shown in Fig. 2.4 (b). The corresponding zigzag chains are planar along each type of x and y bonds, respectively. Chains with equivalent spins are parallel, e.g., chains with red spins in Fig. 2.4 (b). Therefore, it is convenient to call this phase z parallel-zigzag. Note, that the z parallel-zigzag phase has the ordering wave-vector $\mathbf{Q} = \mathbf{\Gamma}$ while the x (y) skew-zigzag phase has the ordering wave-vector $\mathbf{Q} = \mathbf{Y}$.

On the other hand, the stripy phase is defined by the existence of one FM and two AF bonds. The Heisenberg-Kitaev x (y) stripy phase where spins are aligned in $\pm \vec{e}_x$ ($\pm \vec{e}_y$) direction, has FM x (y) bonds and AF y (x) and z bonds, see Fig. 2.4 (c). There are two types of stripes of pairwise parallel FM bonds, so the x (y) stripy phase is called skew-stripy, and it has the ordering wave-vector $\mathbf{Q} = \mathbf{Y}$. Like the zigzag phase, there exists a z

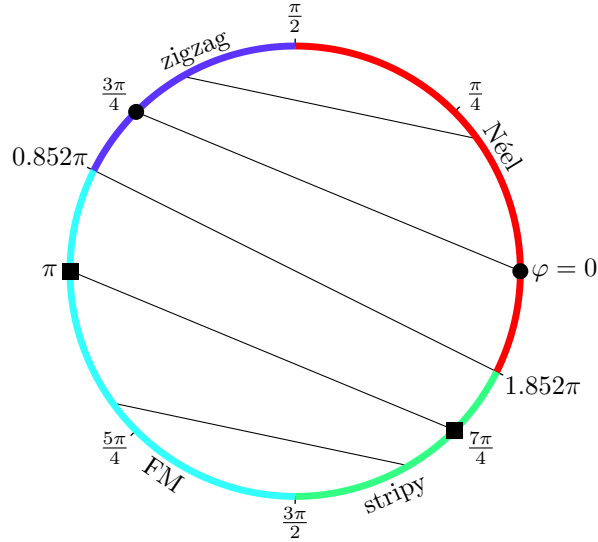
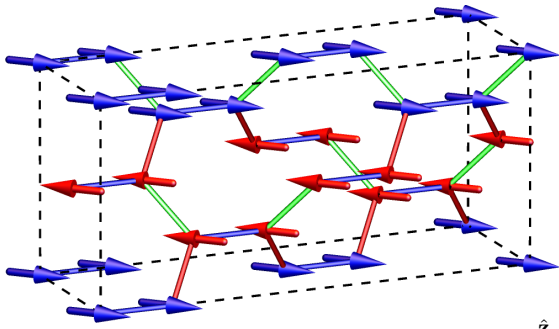
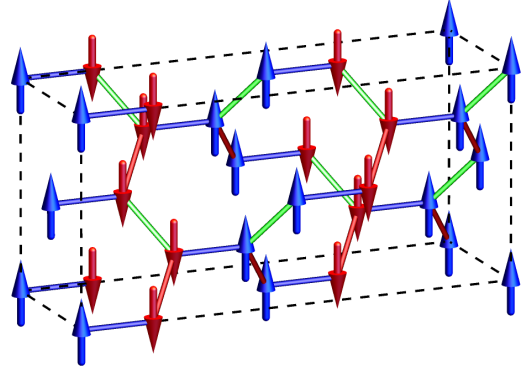


Figure 2.3: The phase diagram of the classical Heisenberg-Kitaev model (2.8) with the parametrization $J = A \cos \varphi$, $K = A \sin \varphi$. Solid lines present the Klein duality transformation which connects the left and the right side of the phase diagram. Black square (circles) mark parameter points which are equivalent to a FM (AF) Heisenberg model. The phase diagram is reproduced from Ref. [15] and can be verified via the Luttinger-Tisza approach, for more details see section 4.1 or Appendix C.

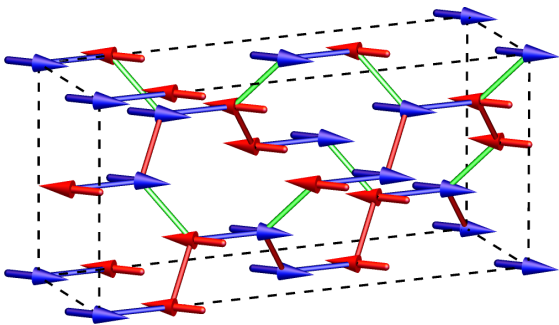
(a) x skew-zigzag



(b) z parallel-zigzag



(c) x skew-stripy



(d) z parallel-stripy

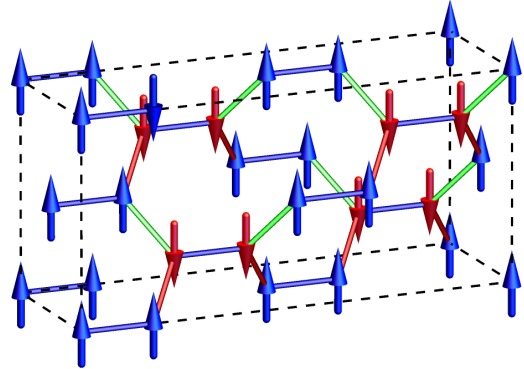


Figure 2.4: Domains of the zigzag and stripy phases of the Heisenberg-Kitaev on the hyperhoneycomb lattice, (a) the skew-zigzag phase with spins pointing in $\pm x$ direction with ordering wave-vector $\mathbf{Q} = \mathbf{Y}$, (b) the z parallel-zigzag phase with $\mathbf{Q} = \mathbf{\Gamma}$, (c) the skew-stripy phase with spins pointing in $\pm x$ direction with ordering wave-vector $\mathbf{Q} = \mathbf{Y}$ and (d) the z parallel-stripy phase with $\mathbf{Q} = \mathbf{\Gamma}$.

parallel-stripy phase with the ordering wave-vector $\mathbf{Q} = \mathbf{\Gamma}$ as shown in Fig. 2.4 (d). We can see stripes of FM bonds with red spins and blue spins which are parallel.

In the zigzag (stripy) regime, there exist more states with exact the same classical energy as the x , y , and z zigzag

(stripy) phases. This highly degenerate ground-state manifold can be understood by the Klein duality and the resulting hidden $SU(2)$ symmetry at certain points in the phase diagram. Like for the honeycomb lattice [25–27], there exists a four-sublattice rotation for the hyperhoneycomb lattice. Note, each of the four sublattices is not a Bravais lattice but has instead a two-site unit cell. The structure of this duality transformation, under which the ordering wave-vector is shifted by $\mathbf{Q} \rightarrow \mathbf{Q} + \mathbf{Y}$, is shown in Fig. 2.5. The spins denoted by black crosses are left unrotated, while the spins marked by red squares, green triangles, and blue circles are rotated by 180 degrees about the \hat{x} , \hat{y} , and \hat{z} axes, respectively.

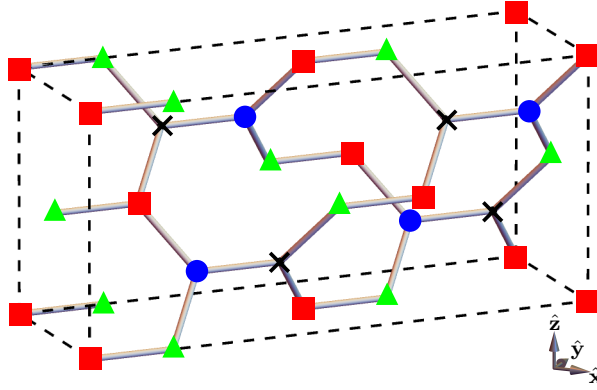


Figure 2.5: Duality transformation for the Heisenberg-Kitaev model. Spins marked by a black cross are left invariant while spins denoted by red square, green triangle and blue circle are rotated by 180 degrees around x , y and z axis, respectively.

In terms of the dual spins \vec{S}'_i the Heisenberg-Kitaev Hamiltonian (2.8) can be written as

$$\mathcal{H}_{\text{HK}} = -J \sum_{\langle ij \rangle} \vec{S}'_i \cdot \vec{S}'_j + 2(K + J) \sum_{\langle ij \rangle_\gamma} S'^{\prime\gamma}_i S'^{\prime\gamma}_j. \quad (2.9)$$

This transformation maps the FM phase onto the stripy phase as well as the Néel phase onto the zigzag phase as denoted by the lines in Fig. 2.3. The so-called Klein points at $\varphi = \frac{3\pi}{4}, \frac{7\pi}{4}$ have a hidden $SU(2)$ symmetry since they are equivalent to the AF ($\varphi = 0$) and FM ($\varphi = \pi$) Heisenberg model. The duality transformation allows us to construct more general zigzag and stripy phases. For a FM state where all spins are aligned in \hat{z} direction, the corresponding dual state is the z parallel-stripy state. Analogously, we find the x (y) skew-stripy phase as the dual state to a FM state with spins in x (y) direction.

On the classical level, we find all directions of FM states have the same energy, also away from the Klein points. For a FM with spins $\vec{S}_i = [S^x, S^y, S^z]$, the nearest-neighbor Kitaev interaction of a single spin has the form $2K(S^x S^x + S^y S^y + S^z S^z)$, which looks like a Heisenberg term in the classical limit. This generates an accidental $SU(2)$ symmetry for the classical model. However, we will call it $SU(2)$ degeneracy instead of symmetry to avoid confusion. This $SU(2)$ degeneracy is transferred to the stripy phase by the four-sublattice rotation. So, the dual state of a FM with an arbitrary spin direction $\vec{S}_i \parallel [n_x, n_y, n_z]$, where at least two components are nonzero, is not one of the before discussed x , y , z stripy phases, but it has the same energy. This state can be denoted as the $[n_x, n_y, n_z]$ domain of the generalized skew-stripy phase. Here we can see why the z stripy phase is special. The FM state with $\vec{S}_i \parallel \hat{z}$ is the only one whose corresponding stripy phase has a magnetic unit cell which is equivalent to the crystallographic unit cell. To sum up, FM states with $\vec{S}_i \in \{\pm\vec{e}_x, \pm\vec{e}_y, \pm\vec{e}_z\}$, $\vec{S}_i \parallel [n_x, n_y, 0]$, $[n_x, 0, n_z]$, $[0, n_y, n_z]$, and $\vec{S}_i \parallel [n_x, n_y, n_z]$ lead to collinear, coplanar, and non-coplanar dual stripy phases, respectively.

An analogous discussion can be done for the duality between the Néel and zigzag phases and leads to the existence of generalized $[n_x, n_y, n_z]$ zigzag states.

2.3 Heisenberg-Kitaev model in an external field

In this section, we introduce the Heisenberg-Kitaev model in an external magnetic field \vec{h} . For this, we add a Zeeman interaction of the form $-\vec{h} \cdot \vec{S}_i$. Now our Hamilton operator has the form

$$\mathcal{H}_{\text{HK}} = J \sum_{\langle ij \rangle} \vec{S}_i \cdot \vec{S}_j + 2K \sum_{\langle ij \rangle_\gamma} S_i^\gamma S_j^\gamma - \vec{h} \cdot \sum_i \vec{S}_i. \quad (2.10)$$

To better understand the behavior in a magnetic field, we first discuss the pure Heisenberg model. For an AF Heisenberg model, the ground state on a bipartite lattice is the Néel state, i.e., neighbored spins are aligned antiparallel. The spin direction is arbitrary due to the SU(2) symmetry of the model. In the presence of an infinitesimal field, this SU(2) invariance is broken and the spins align perpendicular to the field direction as displayed in Fig. 2.6 (a). For an intermediate field strength, the spins rotate continuously in the direction of the field. This is a so-called canted state. Here, the canting is symmetric, i.e., all canting angles are the same, so a continuous phase transition to the polarized high-field phase is possible.

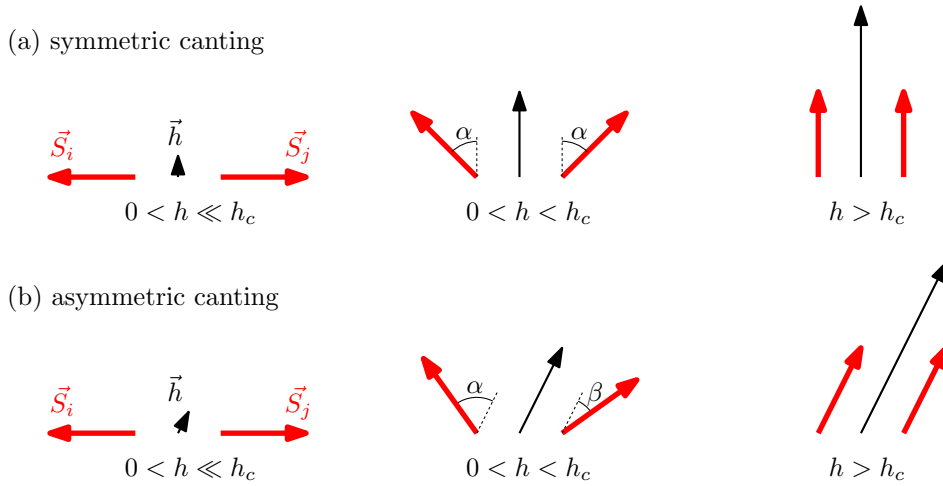


Figure 2.6: Spin canting in the presence of a magnetic field. (a) For a Heisenberg model, the spins can align perpendicular to the field direction in the presence of an infinitesimal field due to the SU(2) symmetry of the model. For $0 < h < h_c$, the spins have a smaller angle to the field direction. In this case all canting angles are equal. In the high-field limit for $h > h_c$, spins are aligned parallel to the field. (b) For an anisotropic model without SU(2) symmetry, the field direction can be chosen such that it has not the same angle to all spins of the zero-field ground state. For intermediate field strengths $0 < h < h_c$, spin canting is possible but with different canting angles due to the asymmetry. Again, spins are aligned parallel to the field for $h > h_c$.

In the presence of an anisotropic interaction like the Kitaev interaction, the SU(2) symmetry is broken and there are field directions which are not perpendicular to the zero-field spin directions, see Fig. 2.6 (b). The angles between field and spins are different so the canting angles in a finite field will be asymmetric. Due to this asymmetry, a continuous transition to the polarized phase is typically not possible. In order to find nontrivial field-induced states, such field configurations are promising, because the asymmetrically canted states are typically unfavorable in terms of energy.

2.4 Spin-wave theory

To search for the ground state of the Heisenberg-Kitaev model on the hyperhoneycomb lattice in an external field, we start with spin-wave theory. In the high-field limit, we can assume the polarized state as the ground state, i.e., all spins are aligned parallel to the magnetic field. The magnon spectrum has a gap for high field strengths. By decreasing the field strength, the gap vanishes at some critical h_{c0} at some instability wave-vector. This indicates a continuous phase transition, as long as there is no first-order transition at some higher $h_c > h_{c0}$. If the transition is continuous, then the ordering wave-vector of the phase below $h_{c,0}$ has to be

the instability wave-vector. On the other hand, there must be somewhere a first-order phase transition or an intermediate phase if the instability wave-vector is not compatible with the ordering wave-vector of the zero-field ground state.

We use the Holstein-Primakoff transformation [28] to express the spin operators by the bosonic operators a_i , b_i , c_i and d_i on the A, B, C and D sublattices,

$$S_i^- = \sqrt{2S}\xi_i^\dagger \sqrt{1 - \frac{\xi_i^\dagger \xi_i}{2S}}, \quad S_i^+ = \sqrt{2S} \sqrt{1 - \frac{\xi_i^\dagger \xi_i}{2S}} \xi_i, \quad S_i^z = S - \xi_i^\dagger \xi_i, \quad (2.11)$$

with $\xi_i = a, b, c, d$ and $[\xi_i, \xi_j^\dagger] = \delta_{ij}$. The classical limit is for $S = \infty$ because the canonical commutation relation $[S^i, S^j] = i\epsilon_{ijk}S^k$ can be written as $[\tilde{S}^i, \tilde{S}^j] = \frac{1}{S}i\epsilon_{ijk}\tilde{S}^k$ where S is the norm of the spin and \tilde{S} is the normalized spin operator. For $S = \infty$, the commutation relation $[\tilde{S}^i, \tilde{S}^j] = 0$ for the normalized spins vanishes and is thus classical. In the semiclassical limit for large S , we can make a $1/S$ expansion of (2.11), leading to

$$S_i^- = \sqrt{2S}\xi_i^\dagger, \quad S_i^+ = \sqrt{2S}\xi_i, \quad S_i^z = S - \xi_i^\dagger \xi_i. \quad (2.12)$$

For $\vec{h} \parallel (\sin\theta \cos\phi \vec{e}_x + \sin\theta \sin\phi \vec{e}_y + \cos\theta \vec{e}_z)$ we use the rotated spin basis

$$\vec{e}_1 = \begin{pmatrix} \cos\theta \cos\phi \\ \cos\theta \sin\phi \\ -\sin\phi \end{pmatrix}, \quad \vec{e}_2 = \begin{pmatrix} -\sin\phi \\ \cos\phi \\ 0 \end{pmatrix}, \quad \vec{e}_3 = \begin{pmatrix} \sin\theta \cos\phi \\ \sin\theta \sin\phi \\ \cos\theta \end{pmatrix}, \quad (2.13)$$

such that the magnetic field lies in the 3-direction. With $S^x = \frac{1}{2}(S^+ + S^-)$ and $S^y = \frac{1}{2i}(S^+ - S^-)$ one can write the spin operators as

$$\vec{S}_i = \sqrt{\frac{S}{2}}(\xi_i + \xi_i^\dagger)\vec{e}_1 - i\sqrt{\frac{S}{2}}(\xi_i - \xi_i^\dagger)\vec{e}_2 + (S - \xi_i^\dagger \xi_i)\vec{e}_3 + \mathcal{O}(1/\sqrt{S}). \quad (2.14)$$

For the calculation, we use the lattice symmetry and the associated conservation of lattice momentum and introduce the Fourier transformed operators

$$\xi_{\mathbf{q}} = \frac{1}{\sqrt{N}} \sum_i e^{-i\mathbf{q}\mathbf{R}_i} \xi_i, \quad (2.15)$$

where \vec{R}_i denotes the lattice position of the spin i and N is the number of unit cells. The calculation is shown in detail in Appendix A. The spin-wave Hamiltonian can be written in matrix form

$$\mathcal{H}_{\text{SW}} = \frac{1}{2} \sum_{\mathbf{q}} \left((\vec{\alpha}_{\mathbf{q}}^\dagger)^T \quad (\vec{\alpha}_{-\mathbf{q}})^T \right) \underbrace{\begin{pmatrix} A(\mathbf{q}) & B(\mathbf{q}) \\ B^\dagger(\mathbf{q}) & A^T(-\mathbf{q}) \end{pmatrix}}_{H_{\text{SW}}(\mathbf{q})} \begin{pmatrix} \vec{\alpha}_{\mathbf{q}} \\ \vec{\alpha}_{-\mathbf{q}}^\dagger \end{pmatrix}, \quad (2.16)$$

where $\vec{\alpha}_{\mathbf{q}}^{(\dagger)} = (a^{(\dagger)}, b^{(\dagger)}, c^{(\dagger)}, d^{(\dagger)})^T$ contains the bosonic creation and annihilation operators and the 4×4 matrices $A(\mathbf{q})$ and $B(\mathbf{q})$ are defined in Appendix A. Because we have bosonic operators we have to calculate the eigenvalues of

$$\begin{pmatrix} \mathbb{1}_{4 \times 4} & 0 \\ 0 & -\mathbb{1}_{4 \times 4} \end{pmatrix} H_{\text{SW}}(\mathbf{q}) \quad (2.17)$$

to get the magnon spectrum [14, 29].

2.5 Phases and classical phase diagram

In this section, we present our results for the ground-state phase diagram of the Heisenberg-Kitaev model in a magnetic field. We distinguish between different field directions.

2.5.1 [1, 0, 0], [0, 1, 0], and [0, 0, 1] directions

First we examine the field directions $\vec{h} \parallel [1, 0, 0]$, $[0, 1, 0]$, and $[0, 0, 1]$. Because the $[1, 0, 0]$ and $[0, 1, 0]$ directions are connected by the C_2 symmetry of the lattice, the phases of the $[0, 1, 0]$ direction can be reproduced from the $[1, 0, 0]$ states with help of the corresponding C_2 transformation. As mentioned in the previous section, the high-field phase is the polarized phase with polarization in field direction. The zero-field phases of the Heisenberg-Kitaev model, except the FM phase, are not adiabatically connected to the polarized phase. So there must be at least one phase transition when decreasing the field strength. A lower bound for the critical field strength h_c , at which there is a phase transition between the polarized phase and another phase, can be computed in spin-wave theory. The magnon spectrum is gapped in the high-field limit and by decreasing the field the gap vanishes at some critical field strength $h_{c,0}$.

In the non-frustrated case, where J and K have the same sign, we expect to find simple canted states due to the $SU(2)$ degeneracy in the classical case. The Néel and FM phases are still the true ground states in the vicinity of the pure Heisenberg points where K has the opposite sign. In this regime, the gap of the magnon spectrum vanishes for all field directions at the same critical field $h_{c,0}$ and the same wave-vector. Fig. 2.9 (a) shows, that in the Néel regime the gap vanishes at $\mathbf{Q} = \mathbf{\Gamma}$ which corresponds to the ordering wave-vector of the zero-field Néel phase. Thus the intermediate phase is just a canted Néel phase. In the vicinity of the FM Heisenberg point the gap vanishes also at $\mathbf{Q} = \mathbf{\Gamma}$ but at $h_{c,0} = 0$ since the FM state is adiabatically connected to the polarized phase.

Fig. 2.7 (a) shows the magnon spectrum above the zigzag phase for $\varphi = 0.62\pi$ at the critical field strength $h_{c,0}$ for the $[1, 0, 0]$ direction. The magnon gap vanishes for this case simultaneously at $\mathbf{Q} = \mathbf{\Gamma}$ and $\mathbf{Q} = \mathbf{Y}$. Because the field is perpendicular to \hat{y} and \hat{z} , simple canting to y skew-zigzag and z parallel-zigzag is possible as described in section 2.3. The instability wave-vectors agree with the ordering wave-vectors $\mathbf{Q} = \mathbf{\Gamma}$ and $\mathbf{Q} = \mathbf{Y}$ of the zero-field phases.

For the same φ but $\vec{h} \parallel [0, 0, 1]$, the gap vanishes at the same $h_{c,0}$ but only at $\mathbf{Q} = \mathbf{Y}$, as Fig. 2.7 (b) shows. In this case, simple canting to the x (y) parallel zigzag phase is possible, which has also $\mathbf{Q} = \mathbf{Y}$ as the ordering wave-vector.

The behavior is qualitatively similar in the parameter regime above the stripy phase. For the $[1, 0, 0]$ direction, the gap vanishes again at $\mathbf{Q} = \mathbf{\Gamma}$ and $\mathbf{Q} = \mathbf{Y}$ while for the $[0, 0, 1]$ direction the gap vanishes only at $\mathbf{Q} = \mathbf{Y}$ but at the same critical field $h_{c,0}$ as shown in Figs. 2.7 (c) and (d), respectively. Again, the instability wave-vectors agree with the ordering wave-vectors of the zero-field phase. Note that for both discussed values of φ the critical field strength agrees with that from the Heisenberg-Kitaev model on the honeycomb lattice [30].

To verify the phase diagram of the Heisenberg-Kitaev model, we investigate different geometries of possible magnetic structures. For that we capture all possible magnetic unit cells with up to 12 sites. This leads to 21 different geometries. We make an analytical parametrization, i.e., we can parametrize each spin \vec{S}_i by two angles θ_i and ϕ_i as

$$\vec{S}_i = S (\vec{e}_1 \sin \theta_i \cos \phi_i + \vec{e}_2 \sin \theta_i \sin \phi_i + \vec{e}_3 \cos \theta_i). \quad (2.18)$$

Now the energy of a possible state can be written in terms of the angles θ_i and ϕ_i . The energy minimization can be done numerically. A more detailed description is given in Appendix B. As a result, the critical field strength h_c agrees with $h_{c,0}$ obtained by spin-wave theory and the corresponding phase transitions are continuous. So

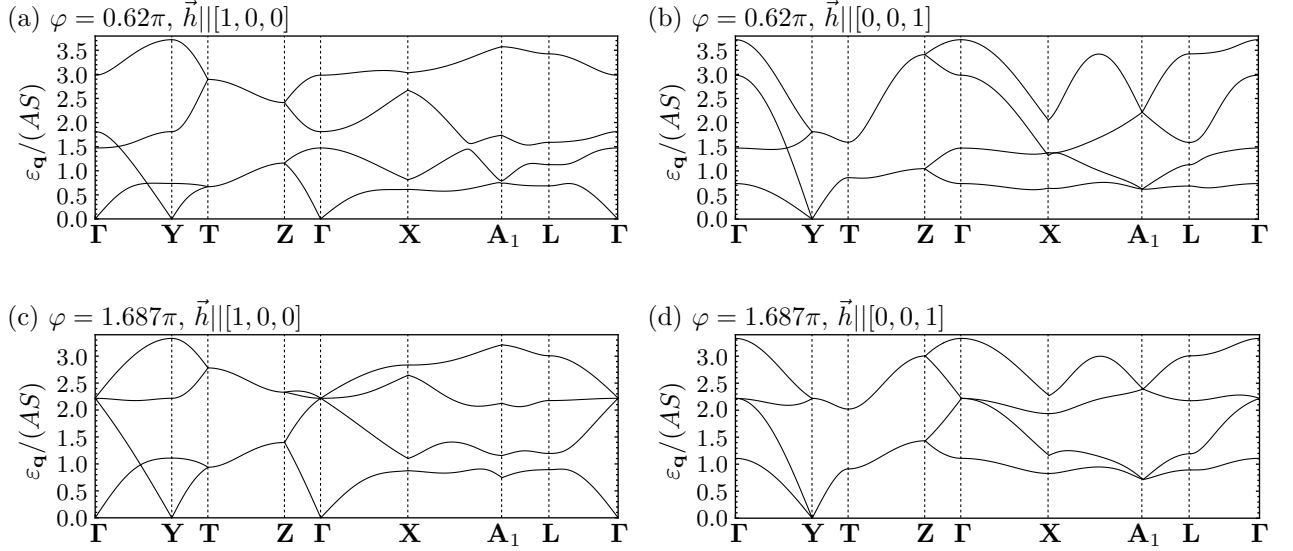


Figure 2.7: Magnon spectra in the high-field phase in the zigzag regime for $\varphi = 0.62\pi$, (a) $\vec{h} \parallel [1, 0, 0]$ and (b) $\vec{h} \parallel [0, 0, 1]$ at the critical field strength $h_{c,0} = 2.98 AS$. Panels (c) and (d) show the same but in the stripy regime for $\varphi = 1.687\pi$ and $h_{c,0} = 2.22 AS$.

Table 2.1: Critical field strength $h_{c,0}$ for field in the $[0, 0, 1]$ and $[1, 0, 0]$ directions obtained by spin-wave theory in the polarized phase and numerical minimization. The critical values of φ are $\varphi_{c,1} = \pi - \arctan \frac{1}{2} \approx 0.852\pi$ and $\varphi_{c,2} = 2\pi - \arctan \frac{1}{2} \approx 1.852\pi$.

φ	$h_{c,0}(\varphi)/(AS)$	phase below h_c
$0 \dots \frac{\pi}{2}$	$6 \cos \varphi + 4 \sin \varphi$	canted Néel
$\frac{\pi}{2} \dots \varphi_{c,1}$	$2 \cos \varphi + 4 \sin \varphi$	canted zigzag
$\varphi_{c,1} \dots \frac{3\pi}{2}$	0	ferromagnet
$\frac{3\pi}{2} \dots \varphi_{c,2}$	$4 \cos \varphi$	canted stripy
$\varphi_{c,2} \dots 2\pi$	$6 \cos \varphi + 4 \sin \varphi$	canted Néel

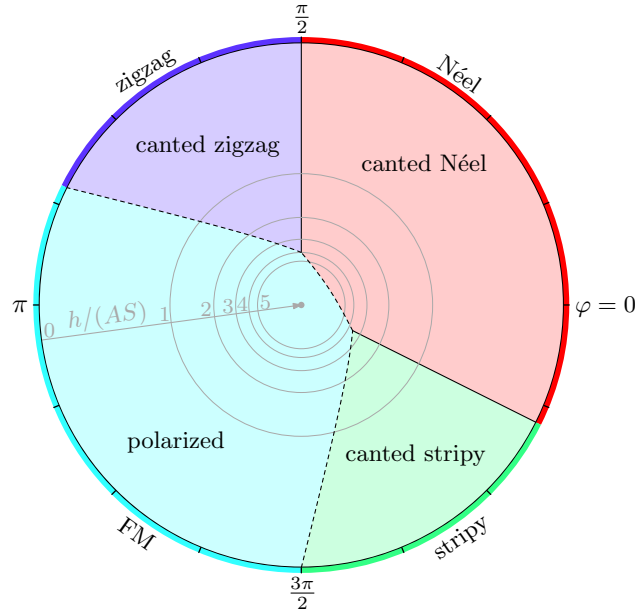


Figure 2.8: Phase diagram of the classical Heisenberg-Kitaev model in a magnetic field $\vec{h} \parallel [1, 0, 0]$. The angle indicates the parameter φ , while the radial component indicates the field strength, such that the zero-field phases are on the border and the high-field phase is in the center of the circle. Solid and dashed lines indicate first-order and continuous phase transitions, respectively.

all intermediate-field phases are simple canted versions of the zero-field phases. The canting angle can be found analytically as $\theta_i = \arccos(h/h_c)$. Also h_c has an analytical form for the simple phases discussed here. When we know the instability wave-vector, we can put it into the spin-wave matrix and get analytical expressions for the eigenvalues. For a given φ , we look for the value of h at which the lowest eigenvalue vanishes. The result is summarized in Table 2.1. The critical field strengths $h_{c,0}$ agree with the result of Reference [16].

The phase diagram is shown in Fig. 2.8. For the field directions $[n_x, n_y, 0]$, $[n_x, 0, n_z]$, and $[0, n_y, n_z]$ where n_x , n_y and n_z are arbitrary numbers, the magnon gap vanishes at $\mathbf{Q} = \Gamma$ above the Néel (FM) phase and at $\mathbf{Q} = \mathbf{Y}$ (for $[0, n_y, n_z]$, $[n_x, 0, n_z]$) and $\mathbf{Q} = \Gamma$ (for $[n_x, n_y, 0]$) above the zigzag (stripy) phase. These are the same wave-vectors as for the $[1, 0, 0]$ direction and also the critical field strengths are the same. Because for these directions simple canting is also possible, the corresponding phase diagrams are predicted to be the same.

2.5.2 [1, 1, 1] direction

For fields in the $[1, 1, 1]$ direction, we expect a more complicated phase diagram, similar to the honeycomb case [30]. We start again with spin-wave theory in the high-field polarized state to obtain the critical field $h_{c,0}$ and the instability wave-vector.

In the Néel regime, the magnon gap vanishes at $\mathbf{Q} = \Gamma$ and some finite $h_{c,0}$ as displayed in Fig. 2.9 (a). This instability wave-vector agrees with that of the Néel phase, so simple canting seems to be possible. For parameters of φ in the ferromagnetic regime, the gap vanishes also at $\mathbf{Q} = \Gamma$ but for $h_{c,0} = 0$, see Fig. 2.9 (b). The spectrum shows quadratic dispersion that is typical for ferromagnetic spin-wave theory. After that analysis, no new phases should occur here.

Something interesting happens in the frustrated regime. For the high-field magnon spectra above the zigzag phase as shown in Fig. 2.9 (c), the magnon gap vanishes between the Γ and X points at the commensurate wave-vector $\mathbf{E} = (-\frac{1}{3}, 0, 0)$. In this case, the instability wave-vector does not correspond to the zero-field ordering wave-vectors $\mathbf{Q} = \Gamma$ and $\mathbf{Q} = \mathbf{Y}$. As explained in section 2.3, the field $\vec{h} \parallel [1, 1, 1]$ is not perpendicular to one of the x , y or z zigzag phases so only an asymmetric canted zigzag phase is possible which has no continuous phase transition to the polarized phase. Now, there are two different possibilities. First, there could be a first-order transition at some $h_c > h_{c,0}$, e.g., to a canted zigzag phase. Second, there can be a continuous phase transition from the polarized phase to a new phase with the ordering wave-vector $\mathbf{Q} = \mathbf{E}$ at the critical field strength $h_{c,0}$. In this case, there must be a first-order transition or yet another intermediate phase at some $0 < h < h_{c,0}$.

In the stripy regime, the gap vanishes also at $\mathbf{Q} = \mathbf{E}$, see the magnon spectrum in Fig. 2.9 (d). This instability wave-vector also does not agree with those of the zero-field stripy state. Thus, an analogous discussion as above applies.

The results of the $[1, 1, 1]$ spin-wave theory are summarized in Table 2.2 and they also agree with Reference [16]. Again, we make an analytical parametrization of spins as denoted in Equation (2.18) and parametrize all possible unit cells with up to 12 spins. The numerical minimization of these geometries leads to a phase diagram with nine different phases as shown in Fig. 2.10. The figure shows that depending on the value of φ , both possibilities (first-order transition vs. intermediate phases) are realized in the frustrated regime.

The occurring phases can be parametrized by fewer parameters than two angles per spin in the magnetic unit cell. The ansatzes are shown in Table 2.3. In the following, we want to discuss the phases.

Canted stripy (zigzag): The canted stripy (zigzag) phase has two different canting angles θ and θ' for a field $\vec{h} \parallel [1, 1, 1]$. The canted versions of the x (y) skew-stripy (skew-zigzag) phase and the z parallel-stripy (parallel-zigzag) phase as shown in Fig. 2.4 (c) and (d) (Fig. 2.4 (a) and (b)), respectively, have the same energy. The canted stripy (zigzag) phase is the ground state for infinitesimal field strength and $\frac{3\pi}{2} < \varphi < \frac{7\pi}{4}$ ($\frac{\pi}{2} < \varphi < \frac{3\pi}{4}$).
FM star: The FM star phase is bordered by the stripy phase at $h = 0$ for $\frac{7\pi}{4} < \varphi < 0.852\pi$. The transition line to the canted stripy phase ends at the Klein point at $\varphi = \frac{7\pi}{4}$. This indicates that in the limit $h \rightarrow 0$

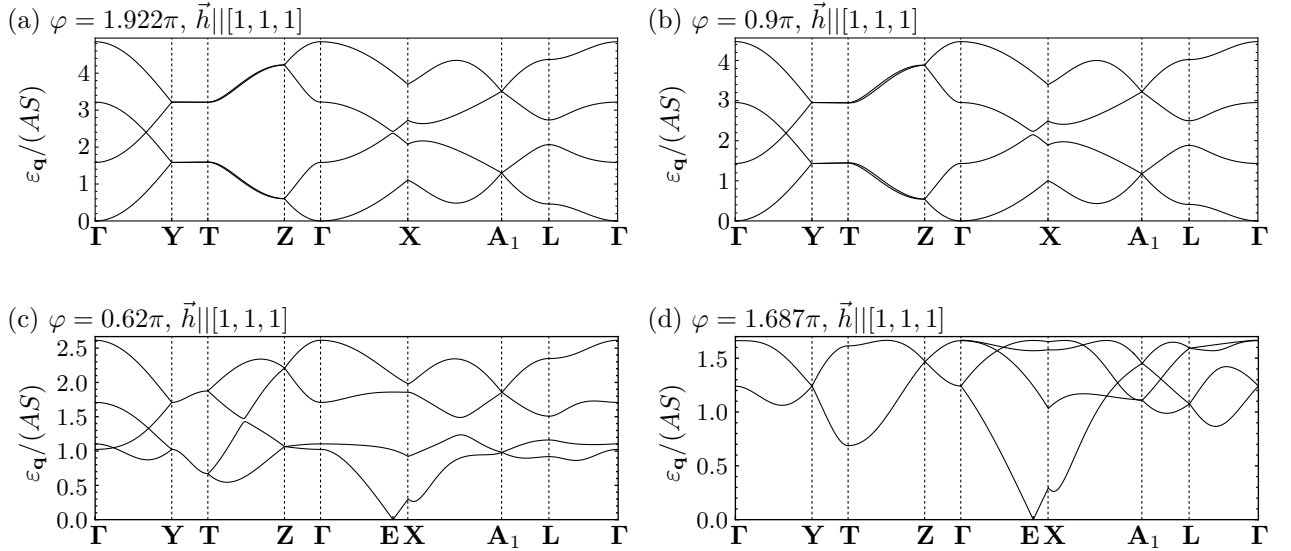


Figure 2.9: Magnon spectra in the high-field phase at the critical field strength $h_{c,0}$ for $\vec{h} \parallel [1, 1, 1]$, (a) $\varphi = 1.922\pi$ and $h_{c,0} = 4.85$, (b) $\varphi = 0.9\pi$ and $h_{c,0} = 0$, (c) $\varphi = 0.62\pi$ and $h_{c,0} = 2.61$, (d) $\varphi = 1.687\pi$ and $h_{c,0} = 1.66$.

Table 2.2: Results from spin-wave theory in the $[1, 1, 1]$ polarized phase. The critical values of φ are $\varphi_{c,1} = \pi - \arctan \frac{3}{4} \approx 0.795\pi$ and $\varphi_{c,2} = 2\pi - \arctan \frac{3}{4} \approx 1.795\pi$.

φ	$h_{c,0}(\varphi)/(AS)$	possible phase below h_c
$0 \dots \frac{\pi}{2}$	$6 \cos \varphi + 4 \sin \varphi$	canted Néel
$\frac{\pi}{2} \dots \varphi_{c,1}$	$3 \cos \varphi + 4 \sin \varphi$	AF vortex
$\varphi_{c,1} \dots \frac{3\pi}{2}$	0	ferromagnet
$\frac{3\pi}{2} \dots \varphi_{c,2}$	$3 \cos \varphi$	vortex
$\varphi_{c,2} \dots 2\pi$	$6 \cos \varphi + 4 \sin \varphi$	canted Néel

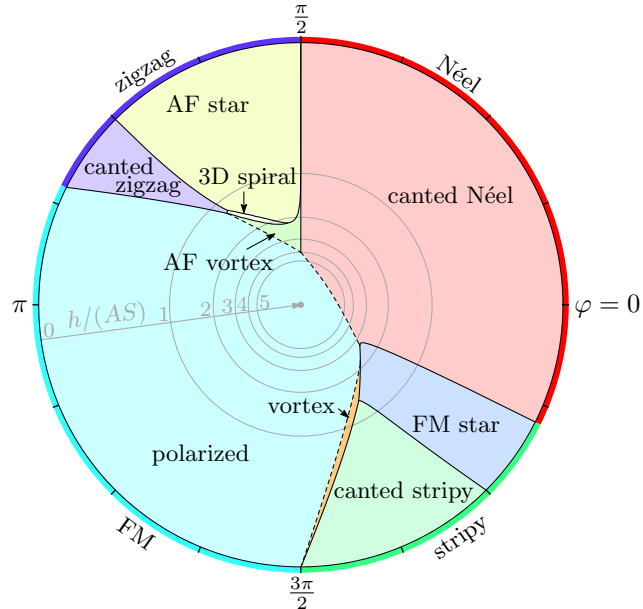


Figure 2.10: Phase diagram of the classical Heisenberg-Kitaev model in a magnetic field $\vec{h} \parallel [1, 1, 1]$. The angle indicates the parameter φ , while the radial component indicates the field strength, such that the zero-field phases are on the border and the high-field phase is in the center of the circle. Solid and dashed lines indicate first-order and continuous phase transitions, respectively.

Table 2.3: Ansatzes for phases in a $[1, 1, 1]$ field. The positions i of spins for $\mathbf{Q} = \Gamma, \mathbf{Y}, \mathbf{E}$ and $\frac{2}{3}\mathbf{Y}$ are shown in Figs. 2.1, 2.11 (a), 2.11 (b) and 2.11 (c), respectively.

Phase	i	ϕ_i	θ_i	Phase	i	ϕ_i	θ_i
polarized	1	0	0	canted Néel	1	0	θ
$\mathbf{Q} = \Gamma$	2	0	0	$\mathbf{Q} = \Gamma$	2	π	θ
	3	0	0		3	0	θ
	4	0	0		4	π	θ
canted z-zigzag	1	0	θ	canted z-stripy	1	0	θ
$\mathbf{Q} = \Gamma$	2	π	θ'	$\mathbf{Q} = \Gamma$	2	0	θ
	3	π	θ'		3	π	θ'
	4	0	θ		4	π	θ'
canted x-zigzag	1	$\frac{5\pi}{3}$	θ	canted x-stripy	1	$\frac{5\pi}{3}$	θ
$\mathbf{Q} = \mathbf{Y}$	2	$\frac{5\pi}{3}$	θ	$\mathbf{Q} = \mathbf{Y}$	2	$\frac{2\pi}{3}$	θ'
	3	$\frac{2\pi}{3}$	θ'		3	$\frac{2\pi}{3}$	θ'
	4	$\frac{2\pi}{3}$	θ'		4	$\frac{5\pi}{3}$	θ
	5	$\frac{2\pi}{3}$	θ'		5	$\frac{2\pi}{3}$	θ'
	6	$\frac{2\pi}{3}$	θ'		6	$\frac{5\pi}{3}$	θ
	7	$\frac{5\pi}{3}$	θ		7	$\frac{5\pi}{3}$	θ
	8	$\frac{5\pi}{3}$	θ		8	$\frac{2\pi}{3}$	θ'
AF star	1	$\frac{2\pi}{3}$	θ	FM star	1	$\frac{5\pi}{3}$	θ
$\mathbf{Q} = \mathbf{Y}$	2	$\frac{\pi}{3}$	θ'	$\mathbf{Q} = \mathbf{Y}$	2	$\frac{\pi}{3}$	θ
	3	0	θ		3	π	θ
	4	0	0		4	0	0
	5	$\frac{4\pi}{3}$	θ		5	$\frac{\pi}{3}$	θ
	6	$\frac{5\pi}{3}$	θ'		6	$\frac{5\pi}{3}$	θ
	7	0	π		7	0	0
	8	π	θ'		8	π	θ
AF vortex	1	$-\delta$	θ	vortex	1	$\pi - \delta$	θ
$\mathbf{Q} = \mathbf{E}$	2	$\pi + \delta$	θ	$\mathbf{Q} = \mathbf{E}$	2	$\pi + \delta$	θ
	3	$\frac{4\pi}{3} - \delta$	θ		3	$\frac{\pi}{3} - \delta$	θ
	4	$\frac{5\pi}{3} + \delta$	θ		4	$\frac{5\pi}{3} + \delta$	θ
	5	$\frac{2\pi}{3} - \delta$	θ		5	$\frac{5\pi}{3} - \delta$	θ
	6	$\frac{\pi}{3} + \delta$	θ		6	$\frac{\pi}{3} + \delta$	θ
	7	$-\delta$	θ		7	$\pi - \delta$	θ
	8	$\pi + \delta$	θ		8	$\pi + \delta$	θ
	9	$\frac{4\pi}{3} - \delta$	θ		9	$\frac{\pi}{3} - \delta$	θ
	10	$\frac{5\pi}{3} + \delta$	θ		10	$\frac{5\pi}{3} + \delta$	θ
	11	$\frac{2\pi}{3} - \delta$	θ		11	$\frac{5\pi}{3} - \delta$	θ
	12	$\frac{\pi}{3} + \delta$	θ		12	$\frac{\pi}{3} + \delta$	θ
3D spiral	1	0	θ_1	3D spiral	7	π	θ_7
$\mathbf{Q} = \frac{2}{3}\mathbf{Y}$	2	π	θ_2		8	0	θ_8
	3	$\frac{4\pi}{3} + \delta_1$	θ_3		9	$\frac{5\pi}{3} - \delta_3$	θ_5
	4	$\frac{5\pi}{3} + \delta_2$	θ_4		10	$\frac{4\pi}{3} - \delta_4$	θ_6
	5	$\frac{\pi}{3} + \delta_3$	θ_5		11	$\frac{2\pi}{3} - \delta_1$	θ_3
	6	$\frac{2\pi}{3} + \delta_4$	θ_6		12	$\frac{\pi}{3} + \delta_2$	θ_4

both phases belong to the $SU(2)$ stripy manifold. The FM star phase for $h \rightarrow 0$ is the duality transformed of the FM phase with spins aligned in the $[1, 1, 1]$ direction. The spin configuration contains $\vec{S}_4 = \vec{S}_7 \parallel [1, 1, 1]$, $\vec{S}_1 = \vec{S}_6 \parallel [1, -1, -1]$, $\vec{S}_2 = \vec{S}_5 \parallel [-1, 1, -1]$, and $\vec{S}_3 = \vec{S}_8 \parallel [-1, -1, 1]$. In a finite field, the spins \vec{S}_4 and \vec{S}_7 are parallel to the magnetic field while the other spins rotate to the field direction with the same angle. For $\varphi \gtrsim \frac{7\pi}{4}$, the AF Heisenberg coupling is the dominant coupling and therefore chooses the FM star phase at finite field for which the canting angle (corresponds to FM component) increases slower with increasing field compared to those of the canted stripy phase. There is a direct phase transition from FM star to the polarized phase but also a transition to the vortex phase.

Vortex: For $\frac{3\pi}{2} < \varphi < \frac{7\pi}{4}$, there is a continuous phase transition from the polarized to the vortex phase. This

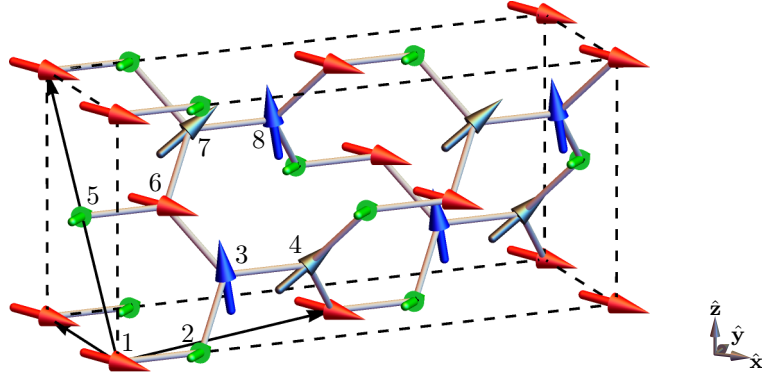
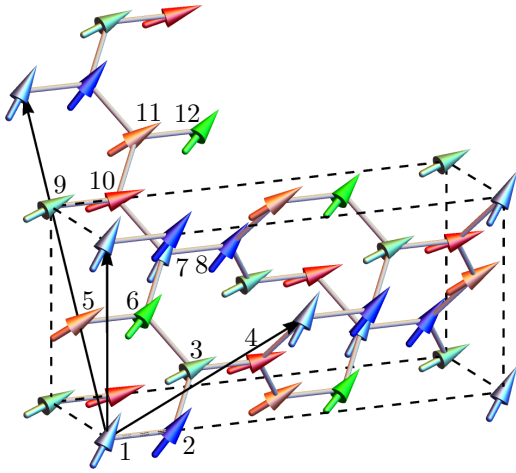
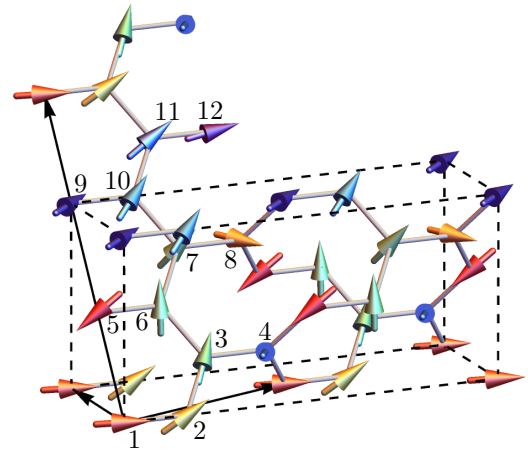
(a) FM star, $\mathbf{Q} = \mathbf{Y}$ (b) vortex $\mathbf{Q} = \mathbf{E}$ (c) 3D spiral, $\mathbf{Q} = \frac{2}{3}\mathbf{Y}$ 

Figure 2.11: (a) FM star phase on the hyperhoneycomb lattice for the parameters $\varphi = 1.687\pi$ and $h = 1.4$ AS. The ordering wave-vector $\mathbf{Q} = \mathbf{Y}$ leads to a magnetic unit cell marked by vectors. (b) Vortex phase for $\varphi = 1.687\pi$ and $h = 1.55$ AS, (c) 3D spiral for $\varphi = 0.58\pi$ and $h = 2.16$ AS. Spins inside a unit cell are labeled by 1 to 8 and 1 to 12, respectively.

transition line is predicted by spin-wave theory and the corresponding vortex phase has the ordering wave-vector $\mathbf{Q} = \mathbf{E}$. The spins begin to cant to the x , y , and z directions, respectively, up to small modulations denoted by $\pm\delta$ in Table 2.3. Each two spins in the magnetic unit cell have the same parametrization. The vortex phase exists only for a small range of h and has first-order phase transitions to the canted stripy and FM star phases.

AF star: For small fields and $\frac{\pi}{2} < \varphi < \frac{3\pi}{2}$, there occurs a new phase called AF star. This can be understood as a canted version of the duality transformed $\pm[1, 1, 1]$ Néel phase. Here, one spin aligns parallel and another one antiparallel to the field while the six other spins in the magnetic unit cell are canted, compare Table 2.3. Due to the relation to the Néel state, the AF star phase has a more AF character as compared to the FM star phase, which is reflected by the two different canting angles θ and θ' .

AF vortex: The AF vortex phase occurs for intermediate field strength between the AF star and the polarized phase. For $\varphi \gtrsim \frac{\pi}{2}$, there is a continuous phase transition to the polarized phase as predicted by spin-wave theory. In this phase with the ordering wave-vector $\mathbf{Q} = \mathbf{E}$, the spins begin to cant in nearly $\pm\hat{x}$, $\pm\hat{y}$, and $\pm\hat{z}$ directions with each the same canting angle. Each two spins inside the magnetic unit cell are equivalent.

3D spiral: Between the AF star and AF vortex phases, the 3D spiral phase is stabilized. It is a period-3 spiral, where there is an AAB pattern of the angles between spins that are connected by the lattice vector \mathbf{b} . The total magnetization differs slightly from the $[1, 1, 1]$ direction. This phase has more parameters than all

other phases in the phase diagram, namely 8 different canting angles and 4 independent modulations of the azimuth angle ϕ_i . This is a hint that the true magnetic unit cell may be larger.

Remarkably, all phases except the 3D spiral occur also in the phase diagram for the Heisenberg-Kitaev model in a field on the honeycomb lattice [30]. A detailed analysis in section 3 shows that the hyperhoneycomb lattice can be mapped to the honeycomb lattice. Under certain conditions, also classical spin states are compatible with that mapping. This 3D-2D equivalence explains, why large parts of the phase diagrams for the hyperhoneycomb and honeycomb lattices agree quantitatively.

However, the model Hamiltonian (2.10) has a higher symmetry than the lattice itself. Since the z bonds are not connected to the x and y bonds by a symmetry transformation, the corresponding coupling constants are in general different. A slightly stronger Kitaev coupling on the z bond, $|K_z| \gtrsim |K_{x,y}|$, will reduce the SU(2) degeneracy for $h = 0$ and chooses the corresponding z domain as the ground state, i.e., the spins are aligned parallel or antiparallel to the z axis. A magnetic field in the $[1, 0, 0]$ direction is perpendicular to this zero-field spin alignment. So simple canting is possible and the phase diagram agrees qualitatively with Fig. 2.8 in the region of canted phases. However, the FM state with spins $\vec{S}_i \parallel [0, 0, 1]$ is not adiabatically connected to the polarized phase with $\vec{S}_i \parallel [1, 0, 0]$. So there is a phase transition in the FM regime at finite field strengths.

On the other hand, a field in the $[0, 0, 1]$ direction is not perpendicular to the zero-field spin state. For instance, the zigzag phase has spins $\vec{S}_i \parallel \pm[0, 0, 1]$, i.e., the spins are parallel and antiparallel to the magnetic field direction, respectively. Such a configuration is typically robust against the external field. Thus, we expect a first-order phase transition to canted zigzag at a finite field. This first-order transition also occurs for the other canted phases. Though, the FM state is now adiabatically connected to the polarized phase and there is no transition between.

The same discussion can be applied to the model in a $[1, 1, 1]$ field. Due to the high frustration, an anisotropic choice of coupling constants may stabilize new phases in the phase diagram.

3 3D-2D equivalence of models and ordered states

In the last chapter, we have presented the phase diagrams of the classical Heisenberg-Kitaev model on the hyperhoneycomb lattice in a magnetic field for the $[0, 0, 1]$ and $[1, 1, 1]$ directions. The $[0, 0, 1]$ phase diagram and almost the whole $[1, 1, 1]$ phase diagram exactly agree with the corresponding phase diagrams of the honeycomb lattice. This interesting fact leads to the question of whether there exists a mapping between these two lattices and further between corresponding models and phases.

3.1 Projection of the hyperhoneycomb model to a honeycomb model

To answer that question, we examine a possible mapping between the hyperhoneycomb and honeycomb lattices and models. Since the spin-wave results for the critical field strengths agree for both lattices, we also look at the magnon spectra.

3.1.1 Projection of the lattice

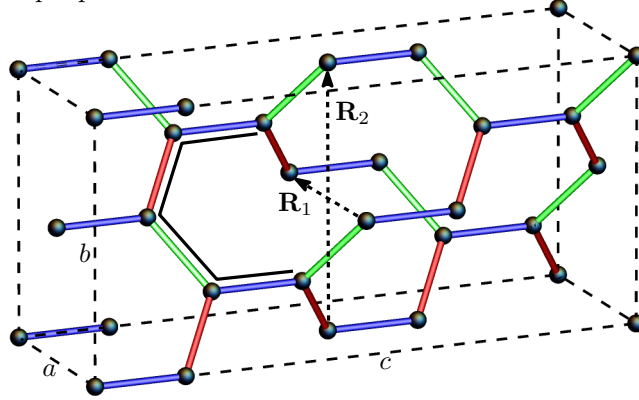
First, we examine the structure of the hyperhoneycomb lattice as shown in Fig. 3.1 (a). Here we can see open honeycombs, i.e., each four coplanar bonds form a part of a honeycomb plaquette. A possible mapping has to close this honeycomb plaquette and is preferably a projection because we want to map a three-dimensional lattice to a two-dimensional lattice. This can be clearly done by rotating two neighboring bonds of the open plaquette into the plane of the plaquette. The two sites which are rotated to the same lattice point should be also mapped to the same point by a suitable projection. The open plaquette displayed in Fig. 3.1 (a) can be closed in this manner by mapping pairs connected by $\mathbf{R}_1 = (-2, 2, 0) = \mathbf{a}$ and $\mathbf{R}_2 = (0, 0, 4) = \mathbf{b}$, what corresponds to a projection of the lattice to the bc-plane and ac-plane, respectively. All other open honeycomb plaquettes can be closed by the same vectors \mathbf{R}_1 and \mathbf{R}_2 by symmetry reasons.

The projection of the hyperhoneycomb lattice to the bc-plane as presented in Fig. 3.1 (b) leads to a distorted honeycomb lattice. However, when the Heisenberg-Kitaev model is also projected one can see that the projected Heisenberg-Kitaev model is not equivalent to the Heisenberg-Kitaev model on the honeycomb lattice because here the x (y) bonds inside a honeycomb plaquette are not on opposite sites. On the other hand, if we look on the projection to the ac-plane as shown in Fig. 3.1 (c), the appropriate Heisenberg-Kitaev model agrees with that one on the honeycomb lattice. The only difference is the elongation of the projected lattice, which does not effect energies of possible states.

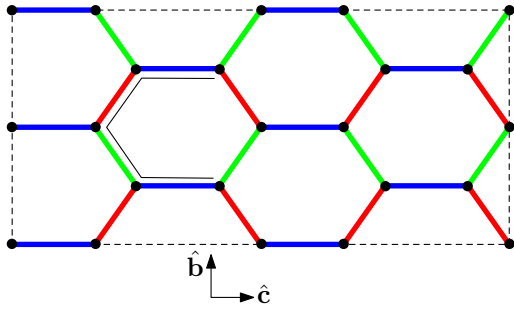
Looking at the hyperhoneycomb lattice from the $\hat{\mathbf{b}}$ direction, as shown in Fig. 3.2, gives an excellent insight into the nature of the projection. As predicted, sites connected by the lattice vector \mathbf{b} are mapped to the same position. Further, bonds connected by \mathbf{b} are also mapped onto each other and the two types of x (y) bonds become parallel under the projection. The same argument works also for states on the hyperhoneycomb lattice: If the spins on pairs of sites connected by \mathbf{b} are equivalent, then the projection maps equivalent spins to the same position on the projected lattice. In this case the projection is useful and we call states with this feature quasi 2D. However, when there exists a pair of non-equivalent spins, they will be mapped to the same position, which makes the projection ambiguous. This kind of phases we call genuine 3D because they do not have an analogous counterpart on the honeycomb lattice.

Since the projection from the hyperhoneycomb lattice to the honeycomb lattice can be visualized in real space, there must be also a mapping in reciprocal space. First we look on a suitable single- \mathbf{Q} state with the commensurate ordering wave-vector $\mathbf{Q} = a\mathbf{b}_1 + b\mathbf{b}_2 + c\mathbf{b}_3$, i.e., a magnetic state for which the relation $e^{i\mathbf{Q}\mathbf{R}} = 1$ is sufficient that the vector \mathbf{R} is a lattice vector of the corresponding magnetic lattice.

(a) open honeycomb plaquette



(b) projection in bc-plane



(c) projection in ac-plane

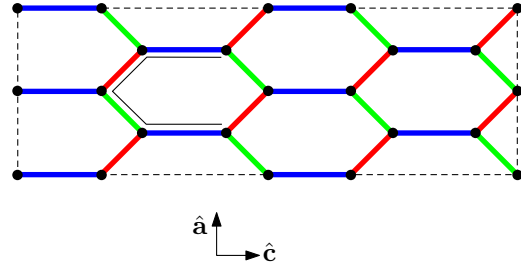


Figure 3.1: (a) Visualization of closing the open honeycomb plaquette denoted by the black solid line on the hyperhoneycomb lattice. The closed honeycomb must have each two x , y and z bonds similar to the honeycomb lattice. So the plaquette can be closed by the two sites connected by \mathbf{R}_1 and \mathbf{R}_2 what corresponds to a projection to the bc -plane and ac -plane, respectively. Projection of the orthorhombic unit cell to the (b) bc -plane and (c) ac -plane leads to distorted honeycomb lattices with different orders of the x , y , and z bonds.

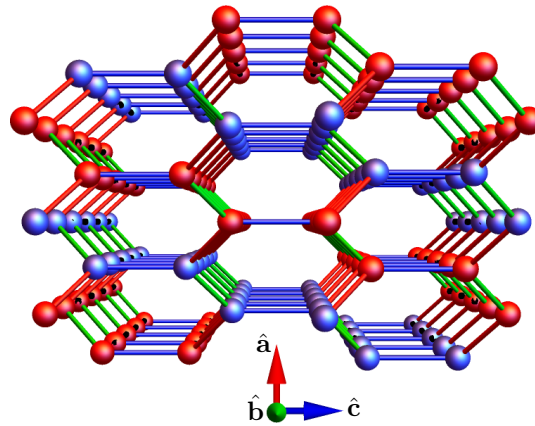


Figure 3.2: View on the hyperhoneycomb lattice from the $\hat{\mathbf{b}}$ direction. Same types of x , y , and z (red, green, and blue) bonds seem to be parallel from that point of view. Blue and red balls belong to spins $\hat{S}_i \parallel \pm \hat{\mathbf{x}}$ and symbolize the x skew-zigzag phase, compare with Fig. 2.4 (a).

For the crucial lattice vector $\mathbf{R} = \mathbf{b} = -\mathbf{a}_1 + \mathbf{a}_2 + \mathbf{a}_3$ that means

$$e^{i\mathbf{Q}\cdot\mathbf{b}} = e^{-2\pi i(-a+b+c)} = 1. \quad (3.1)$$

This is equivalent to the equation

$$-a + b + c = l, \quad l \in \mathbb{Z}, \quad (3.2)$$

which describes planes in the reciprocal space. So there is a family of planes which correspond to quasi-2D order. Equivalently, we can write $\mathbf{b} = [0, 0, 4]$ in the cubic basis, which leads to the plane condition $Q_z = m\pi/2$ with $m \in \mathbb{Z}$. We find $\mathbf{Z} \sim \mathbf{c}^* \sim (\mathbf{b}_1 + \mathbf{b}_2)$ and $\mathbf{X} \sim \mathbf{a}^* \sim (\mathbf{b}_1 + \mathbf{b}_3)$, so the ΓZX -plane belongs to $l = 0$. Similar, we find that the YTA_1 plane (the hexagonal front side of the Brillouin zone) belongs to $l = -1$. As the back side is equivalent to the front side, we find two independent quasi-2D planes in the 3D Brillouin zone, the ΓZX -plane and the hexagonal front side.

Fig. 3.3 displays the Brillouin zone of the hyperhoneycomb lattice, where the front side hexagon can be folded back into the ΓZX -plane, so that all possible quasi-2D wavevectors lie inside a rectangle up to reciprocal lattice vectors. What that means can be seen by a more detailed analysis of the projection. The projected lattice as shown in Fig. 3.4 (a) looks like an elongated honeycomb lattice. One finds that this lattice can be deformed to a honeycomb lattice like in Fig. 3.4 (b) by compressing it by a factor of $\sqrt{3}$ in the $\hat{\mathbf{c}}$ direction. This mapping works also in the reciprocal space. Since the original hyperhoneycomb lattice has a four-site primitive unit cell an analogous four-site unit cell can be chosen on the projected lattice which leads to a rectangular shape of the Brillouin zone which is figured in Fig. 3.4 (c). The corresponding high-symmetry points are equivalent to the high-symmetry points of the hyperhoneycomb lattice. Since the primitive unit cell of the projected lattice has two instead of four sites there exists an extended Brillouin zone with a hexagonal shape. Like the transformation in real space, this Brillouin zone can be transformed to the Brillouin zone of the honeycomb lattice by extending it in $\hat{\mathbf{c}}$ direction by a factor of $\sqrt{3}$, see Fig. 3.4 (d).

3.1.2 Projection of states

As mentioned above, the projection works also for classical spin states on the hyperhoneycomb lattice. In the following, we want to briefly discuss the projective behavior of the phases found in Section 2. For states with the ordering wave-vector $\mathbf{Q} = \mathbf{\Gamma}$, like for the polarized and canted Néel phases or the z domains of the canted zigzag and stripy phases, the projection works since the magnetic unit cell is the crystallographic unit cell. On the other hand, the FM-star and AF-star phases have the ordering wave-vector $\mathbf{Y} = (0, -\frac{1}{2}, 0)$ which has a component in the $\hat{\mathbf{b}}$ direction, but it can be folded back into the ac -plane by a reciprocal lattice vector, as displayed in Fig. 3.3. Thus, the states have no modulation in the $\hat{\mathbf{b}}$ direction, see Fig. 2.11 (a), and they can be projected to the honeycomb lattice. The projection also works for the vortex and AF-vortex phases with $\mathbf{Q} = \mathbf{E}$.

However, the 3D spiral has no counterpart on the honeycomb lattice. The ordering wave-vector is $\mathbf{Q} = \frac{2}{3}\mathbf{Y}$, which does not lie in the ac -plane. Thus, the 3D spiral can not be mapped to the honeycomb lattice. This fact is shown explicitly in Fig. 2.11 (c) by the modulation of the spins in the $\hat{\mathbf{b}}$ direction.

3.1.3 Projection of the magnon spectrum

With the help of the projective equivalence of states, we have a deeper understanding of the spin-wave results. For a field in the $[1, 0, 0]$ direction, the magnon gap vanishes simultaneously at $\mathbf{Q} = \mathbf{\Gamma}$ and $\mathbf{Q} = \mathbf{Y}$ for $\varphi = 0.62\pi$, see Fig. 3.5 (a). On the other hand, the gap for the model on the honeycomb lattice [30] vanishes at $\mathbf{Q} = \mathbf{M}_y$ and $\mathbf{Q} = \mathbf{M}_z$ as shown in Fig. 3.5 (b). As mentioned in Fig. 3.4 (d), the projected four-site unit cell on the honeycomb lattice can be constructed by backfolding the Brillouin zone by \mathbf{M}_z . So the wave-vector \mathbf{M}_z is equivalent to $\mathbf{\Gamma}$ in the projected Brillouin zone. On the other hand, \mathbf{M}_x and \mathbf{M}_y are connected by \mathbf{M}_z and are thus equivalent. However, for a field in the $[0, 0, 1]$ direction, the gap vanishes at $\mathbf{Q} = \mathbf{M}_x$ and $\mathbf{Q} = \mathbf{M}_y$ on the honeycomb lattice. These are both equivalent to \mathbf{Y} , which is the instability wave-vector for

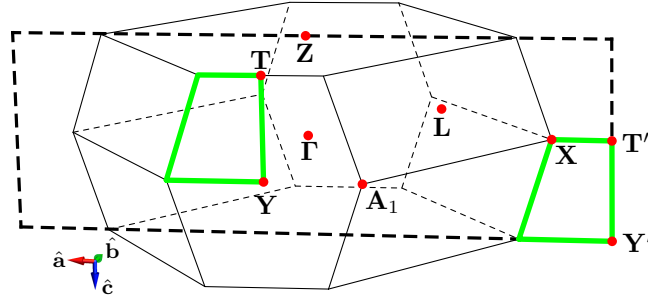


Figure 3.3: Brillouin zone of the hyperhoneycomb lattice with high-symmetry points. The thick black dashed line indicates the Brillouin zone of the projected lattice which can be constructed by folding back the front side hexagon to the ΓZX -plane, here visualized by the green square.

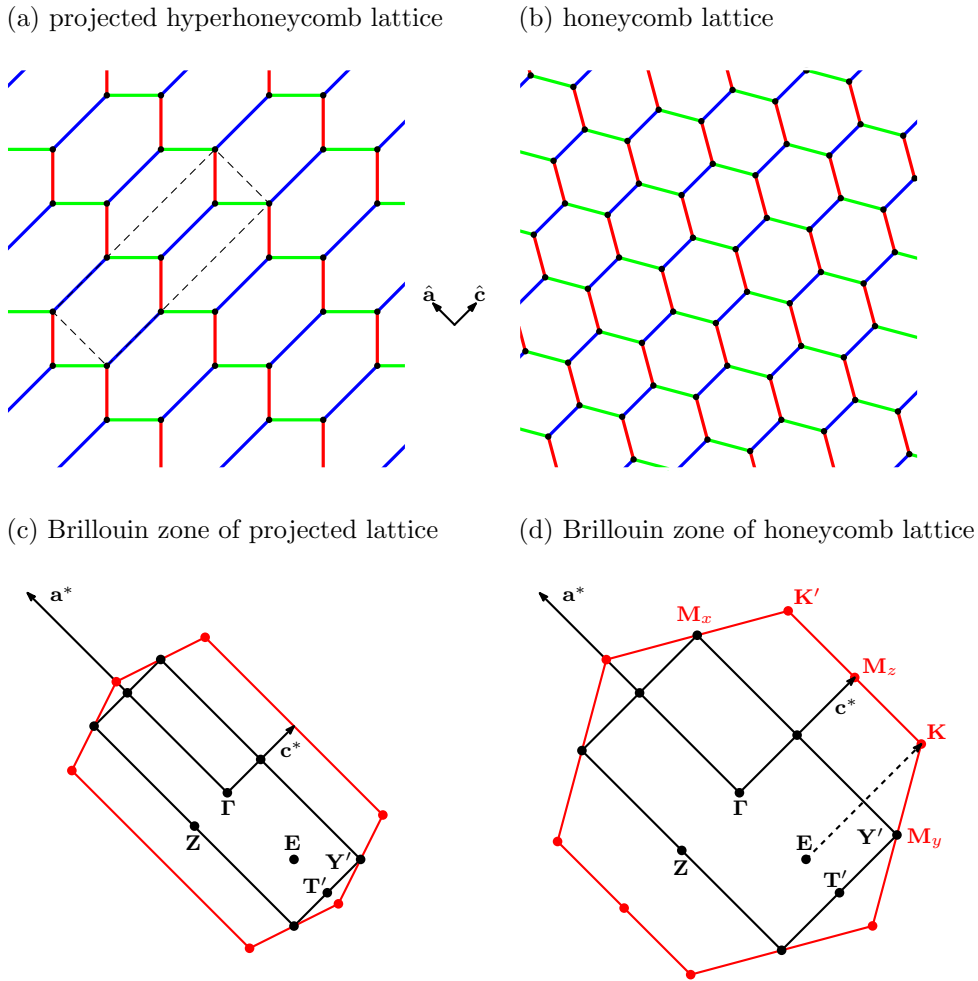


Figure 3.4: (a) The projection of the hyperhoneycomb lattice to the ac -plane. The dashed rectangle indicates the original four-site primitive unit cell. (b) The honeycomb lattice which follows by a deforming of the projected lattice in \hat{c} direction. (c) The Brillouin zone of the projected lattice. The black rectangle and red hexagon indicate the Brillouin zone for a unit cell with four and two sites, respectively. (d) The Brillouin zone of the honeycomb lattice can be connected to a part of the Brillouin zone of the hyperhoneycomb lattice. The M points labeled by M_x , M_y , and M_z correspond to wave-vectors parallel to the x , y , and z bonds, respectively.

the hyperhoneycomb model.

For a field in the $[1, 1, 1]$ direction, the magnon gap closes at $\mathbf{Q} = \mathbf{K}$ on the honeycomb lattice, as displayed in Fig. 3.5 (d). Upon backfolding, the \mathbf{K} point is equivalent to a point inside the projected Brillouin zone, which is exactly the instability wave-vector $\mathbf{Q} = \mathbf{E}$ obtained by spin-wave theory on the hyperhoneycomb lattice, see

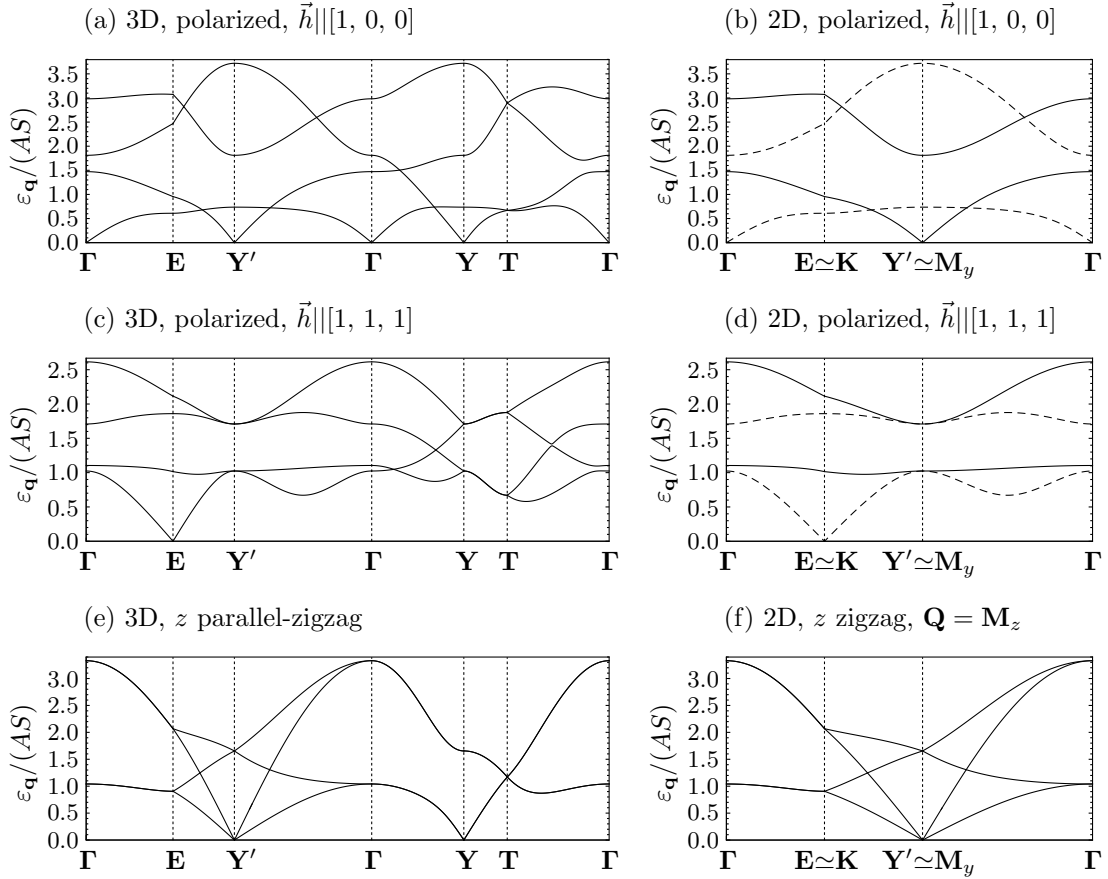


Figure 3.5: Comparison of the Heisenberg-Kitaev magnon spectrum along points in the Brillouin zone (shown in Figs. 3.3 and 3.4) on the 3D hyperhoneycomb lattice and the 2D honeycomb lattice for $\varphi = 0.62\pi$. Panel (a) shows the spectrum in the polarized phase for field in the $[1, 0, 0]$ direction at the critical field strength $h = 2.98 AS$ while (b) figures the same but for the 2D case. Dashed lines indicate bands which are folded back by \mathbf{M}_z into the first Brillouin zone what corresponds to the projected primitive unit cell. (c) and (d) show the same but for field in the $[1, 1, 1]$ direction at the critical field strength $h = 2.61 AS$. Panels (e) and (f) show the spectrum in the zigzag phase for $h = 0$. On the honeycomb lattice, the magnetic unit cell of the z zigzag phase corresponds to the projected unit cell. Note the path $\Gamma - \mathbf{E} - \mathbf{Y}' - \Gamma$ contains only quasi-2D wave-vectors and the corresponding spectrum is each equivalent to the 2D spectrum.

Fig. 3.5 (c).

Further, we can map the whole magnon spectrum of the quasi-2D wave-vectors to the honeycomb lattice. This can be seen in Fig. 3.5. Here the path $\Gamma - \mathbf{E} - \mathbf{Y}' - \Gamma$ lies in the quasi-2D plane and the spectrum is equivalent to that on the honeycomb lattice. This is true for the high-field phases for different field directions and also for the zero-field phases. Due to the elongation between the projected lattice and the honeycomb lattice, some paths on the honeycomb lattice are extended compared to paths on the projected lattice.

The mapping of the magnon spectrum works also for the zigzag phase, see Figs. 3.5 (e) and (f). The spectrum has a pseudo-Goldstone mode at $\mathbf{Q} = \mathbf{Y}'$ which is shifted from the z zigzag ordering wave-vector $\mathbf{Q} = \mathbf{\Gamma}$, in full agreement with the situation on the honeycomb lattice [31]. It has a linear dispersion, since zigzag is a dual Néel state. An anisotropic choice of the Kitaev couplings can destroy the pseudo-Goldstone mode. For $K_z > K_{x,y}$, the z -zigzag domain is chosen as the only ground state and the classical degeneracy is reduced. This opens a gap in the magnon spectrum. On the other hand, $K_z < K_{x,y}$ leads to a $U(1)$ degenerate ground state manifold and the pseudo-Goldstone mode is present. However, the C_3 symmetry protects the pseudo-Goldstone mode for the planar honeycomb model.

Further, the 3D-2D equivalence applies to other momentum-resolved observables, for instance, to the dynamic structure factor $\mathcal{S}(\mathbf{q}, \omega)$ [14] with the wave-vector \mathbf{q} lying in the ac -plane.

3.2 Extended models

3.2.1 Beyond nearest neighbors

Until now we have restricted to models with nearest-neighbor interaction. Hamiltonians for modeling real materials typically contain second- and third-nearest-neighbor interaction. The analysis of the mapping for those long-range interactions seems to be of interest because second-nearest-neighbor Dzyaloshinskii–Moriya interaction or third-nearest-neighbor Heisenberg interaction may be important to describe Kitaev materials [32]. To demonstrate the mapping, we consider an n -th nearest-neighbor Heisenberg model, where the coupling strength depends only on the Euclidian distance of pairs of spins. This approximation does not capture the fact that symmetry-inequivalent n -th neighbor paths will have in general different exchange couplings due to the underlying quantum chemistry.

Due to the crystal symmetry, each site has the same number of n -th nearest neighbors. Table 3.1 shows the number of n -th nearest neighbors on the hyperhoneycomb lattice compared to the honeycomb lattice for $n \leq 7$. The corresponding pairs of sites with $n = 7$ are exactly these ones that are connected by $\mathbf{b} = (0, 0, 4)$ and are thus equivalent under the projection. As we can see, there are three nearest neighbors on each lattice. For $n \geq 2$, the number of neighbors differs on both lattices, e.g. for $n = 2$ there are 10 neighbors on the hyperhoneycomb lattice, but only six neighbors on the honeycomb lattice.

An interesting question is whether n -th nearest neighbors stay n -th nearest neighbors under the projection. Fig. 3.6 shows that this is generally not the case. While nearest neighbors stay nearest neighbors, second-nearest (third-nearest) neighbors are mapped to a combination of second- and fourth-nearest (third- and sixth-nearest) neighbors.

3.2.2 Heisenberg-Kitaev- Γ model

The above introduced projection can be applied to more general models. There are more possible symmetry allowed interaction terms than the Heisenberg and Kitaev interactions. It has been shown that for modeling Kitaev materials also a symmetric off-diagonal Γ interaction is important [18, 32, 33]. For the hyperhoneycomb lattice [17], this leads to a Hamiltonian of the form

$$\mathcal{H}_{\text{HK}\Gamma} = \sum_{\langle ij \rangle_\gamma} \left[J \vec{S}_i \cdot \vec{S}_j + K S_i^\gamma S_j^\gamma \pm \Gamma \left(S_i^\alpha S_j^\beta + S_i^\beta S_j^\alpha \right) \right], \quad (3.3)$$

where γ labels the type of bond and (α, β, γ) is a permutation of (x, y, z) . This Heisenberg-Kitaev- Γ model on the hyperhoneycomb lattice has an alternating sign structure of the Γ term, in contrast to the corresponding model on the honeycomb lattice. The sign structure of the Γ term is shown in Fig. 3.7 (a). To simplify the model, the absolute strength of each coupling is chosen to be the same for each bond, although the z bonds are not symmetry equivalent to the x (y) bonds. However, the relative signs for the x and y bonds can be verified by the lattice rotation symmetries. There are three orthogonal C_2 rotation axes in the middle of each z bond whose axes correspond to the crystallographic $\hat{\mathbf{a}}$, $\hat{\mathbf{b}}$, and $\hat{\mathbf{c}}$ directions and thus called C_a , C_b , and C_c , respectively. Since the model is based on strong spin-orbit coupling, these C_2 rotation are instantly applied in spin space what is marked as C_2^* . For the C_a^* transformation, x and y bonds are interchanged in real space and the Γ^x (Γ^y) interaction is mapped to Γ^y (Γ^x). On the other hand, the C_b^* maps x (y) bonds to x (y) bonds and Γ^x (Γ^y) to $-\Gamma^x$ ($-\Gamma^y$). C_c^* can be written as a combination of C_a^* and C_b^* . Note that the Γ^z interaction is invariant under these transformations. This symmetry argument only fixes the relative sign of the Γ term which can be positive or negative.

Note that for this choice of couplings the local C_3^* symmetry is protected. Each lattice site is bordered by three coplanar bonds. These tripels of bonds are perpendicular to the $[-1, 1, 1]$ and $[1, -1, 1]$ axes, respectively, while the corresponding C_3^* transformations fix the relative signs of the Γ terms for the $-++$ and $+--$

Table 3.1: Number of n -th nearest neighbors on the hyperhoneycomb and honeycomb lattices for an arbitrary lattice site. The distance is given for pairs of neighbors on the hyperhoneycomb lattice.

n	distance	# hyperhoneycomb	# honeycomb
0	0	1	1
1	$\sqrt{2}$	3	3
2	$\sqrt{6}$	10	6
3	$\sqrt{8}$	6	3
4	$\sqrt{10}$	10	6
5	$\sqrt{12}$	2	6
6	$\sqrt{14}$	10	6
7	4	2	6

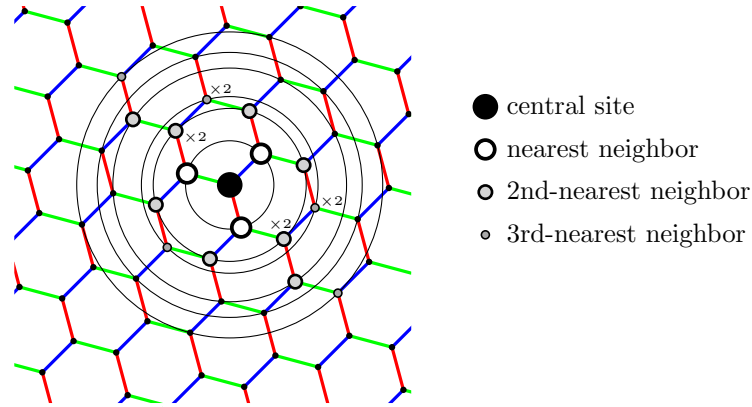


Figure 3.6: Positions of n -th nearest neighbors on the hyperhoneycomb lattice after the projection to the honeycomb lattice. "x2" denotes cases where two different n -th nearest neighbors map to the same site on the honeycomb lattice. The circles around the central site mark n -th nearest neighbors on the honeycomb lattice with $n = 1, \dots, 6$.

xyz -bond-tripels. Since C_3 is not a symmetry transformation of the entire lattice this is just an approximation. The mapping of the Heisenberg-Kitaev- Γ model leads to a 2D model as shown in Fig. 3.8 (a). Due to the enlarged four-site primitive unit cell of the projected lattice, there is a lower symmetry compared to the original honeycomb model displayed in Fig. 3.8 (c). The C_3 symmetry which relates all three types of bonds is not present for the projected model, since the z bonds on the original lattice are not symmetry equivalent to the x and y bonds.

3.2.3 Duality transformation for the projected model

As shown above, the projected Heisenberg-Kitaev- Γ model is not equivalent to the Heisenberg-Kitaev- Γ model for the honeycomb lattice due to the alternating sign structure of the Γ term. However, there are some limits where both model are equivalent. This is true for the pure Heisenberg-Kitaev model because the local interaction terms behave similar on the harmonic honeycomb lattices and nearest neighbors stay nearest neighbors under the projection.

There exists also another limit where the projected model corresponds to the honeycomb model. To illustrate a suitable duality transformation for the projected hyperhoneycomb model, we write the Hamiltonian in compact matrix form

$$\mathcal{H} = \sum_{\langle ij \rangle_\gamma} \vec{S}_i^T \mathcal{H}_{\langle ij \rangle_\gamma} \vec{S}_j = \sum_{\langle ij \rangle_\gamma} \vec{S}'_i{}^T \mathcal{H}'_{\langle ij \rangle_\gamma} \vec{S}'_j, \quad (3.4)$$

where $\mathcal{H}_{\langle ij \rangle_\gamma}$ is one of the following matrices

$$\begin{aligned}\mathcal{H}_{\langle ij \rangle_x} = \mathcal{H}_{(J,K,\pm\Gamma)}^x &= \begin{pmatrix} J+K & 0 & 0 \\ 0 & J & \pm\Gamma \\ 0 & \pm\Gamma & J \end{pmatrix}, \\ \mathcal{H}_{\langle ij \rangle_y} = \mathcal{H}_{(J,K,\pm\Gamma)}^y &= \begin{pmatrix} J & 0 & \pm\Gamma \\ 0 & J+K & 0 \\ \pm\Gamma & 0 & J \end{pmatrix}, \\ \mathcal{H}_{\langle ij \rangle_z} = \mathcal{H}_{(J,K,\Gamma)}^z &= \begin{pmatrix} J & \Gamma & 0 \\ \Gamma & J & 0 \\ 0 & 0 & J+K \end{pmatrix}.\end{aligned}\tag{3.5}$$

The sign structure of the Γ -term can be seen in Fig. 3.8 (a). The Hamiltonian can also be written in terms of dual spins $\vec{S}'_i = R_i \vec{S}_i$ where R_i is a rotation matrix, i.e., $R_i^T R_i = \mathbb{1}$. The corresponding bond interaction $\mathcal{H}'_{\langle ij \rangle_\gamma} = R_i \mathcal{H}_{\langle ij \rangle_\gamma} R_j^T$ transforms analogously. Note, this $\text{SO}(3)$ transformation works for classical spins but since $\text{SO}(3)$ is isomorphic to $\text{SU}(2)$ there exists an analogous transformation for the quantum spin operators and the duality transformation works even in the quantum case. We can define the two rotations

$$R_1 = \begin{pmatrix} 0 & -1 & 0 \\ 1 & 0 & 0 \\ 0 & 0 & 1 \end{pmatrix}, \quad R_2 = \begin{pmatrix} 0 & 1 & 0 \\ -1 & 0 & 0 \\ 0 & 0 & 1 \end{pmatrix},\tag{3.6}$$

which define a duality transformation when applying R_1 and R_2 on spins on black and orange lattice points in Fig. 3.7 (a), respectively, which belong to rotations about the z axis by angles of $\pi/2$ and $3\pi/2$.

The appearing interaction matrices transform as following

$$\begin{aligned}R_1 \mathcal{H}_{(J,K,-\Gamma)}^x R_1^T &= \mathcal{H}_{(J,K,\Gamma)}^y, & R_2 \mathcal{H}_{(J,K,\Gamma)}^x R_2^T &= \mathcal{H}_{(J,K,\Gamma)}^y, \\ R_1 \mathcal{H}_{(J,K,\Gamma)}^y R_1^T &= \mathcal{H}_{(J,K,\Gamma)}^x, & R_2 \mathcal{H}_{(J,K,-\Gamma)}^y R_2^T &= \mathcal{H}_{(J,K,\Gamma)}^x, \\ R_1 \mathcal{H}_{(J,K,\Gamma)}^z R_2^T &= \mathcal{H}_{(-J,K+2J,\Gamma)}^z.\end{aligned}\tag{3.7}$$

The duality transformation interchanges x and y bonds while it converts the $\pm\Gamma$ interaction to a $+\Gamma$ interaction. This agrees with the convention for the planar honeycomb Γ model as demonstrated in Fig. 3.7 (c). Note that one can compensate the interchange of x and y bonds by rotating the lattice around 180 degrees around the z bond.

For a finite Heisenberg coupling J , the Heisenberg and Kitaev couplings on the z bond distinguish from the couplings on the x and y bonds for the dual model. When $J = 0$, the dual model is equivalent to the corresponding honeycomb model. In that sense, the projected Kitaev- Γ model for the hyperhoneycomb lattice and the Kitaev- Γ model for the honeycomb lattice are thermodynamically equivalent.

Since a magnetic field is transformed like a spin, this transformation maps an arbitrary uniform field to a non-uniform field. However, a field in the $[0, 0, 1] \parallel \hat{\mathbf{b}}$ direction remains invariant. This implies that the honeycomb and projected models in the limit $J = 0$ are equivalent even in an applied field $\vec{h} \parallel \hat{\mathbf{b}}$. This holds for both, the classical and the quantum case.

3.3 Harmonic honeycombs

The hyperhoneycomb lattice is part of the so-called harmonic honeycomb lattice series [19, 23], see Fig. 3.7. On the hyperhoneycomb lattice, there are no closed honeycomb plaquettes thus it is denoted as $\mathcal{H}\langle 0 \rangle$. The neighbored bonds of the x (y) bonds are coplanar while the neighbored bonds of the z bonds are not coplanar.

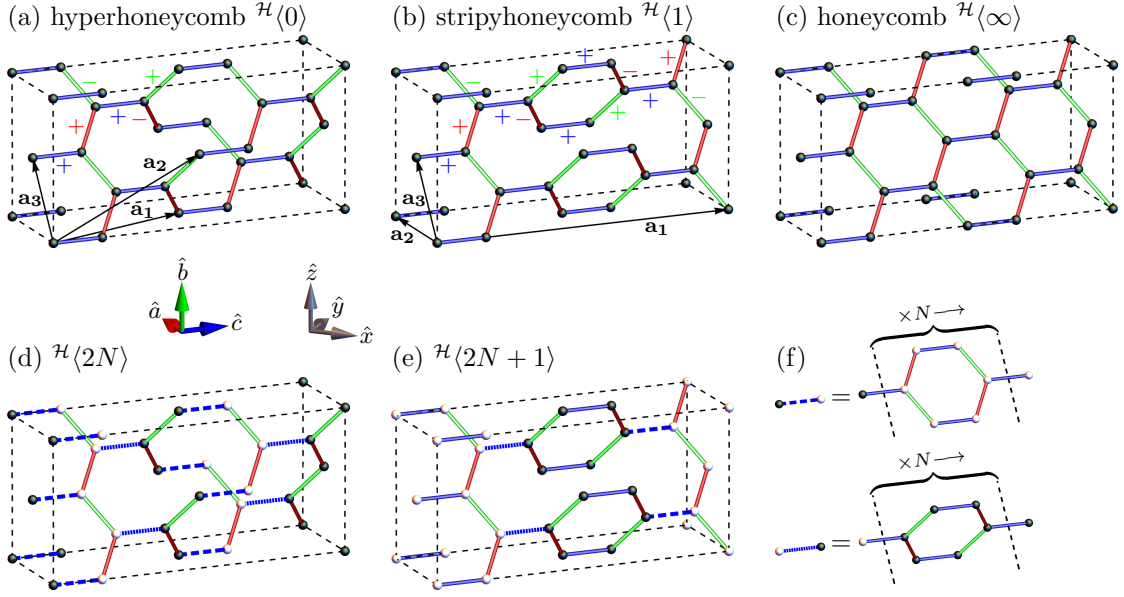


Figure 3.7: Harmonic honeycomb lattice series $\mathcal{H}\langle N \rangle$ with N be the number of rows with complete honeycomb plaquettes. (a), (b) and (c) show the hyperhoneycomb $\mathcal{H}\langle 0 \rangle$, striphoneycomb $\mathcal{H}\langle 1 \rangle$ and honeycomb $\mathcal{H}\langle \infty \rangle$ lattices, respectively. (d)-(f) show building blocks for general N . The labels " \pm " present the sign structure of the model Hamiltonian in Equation (3.3).

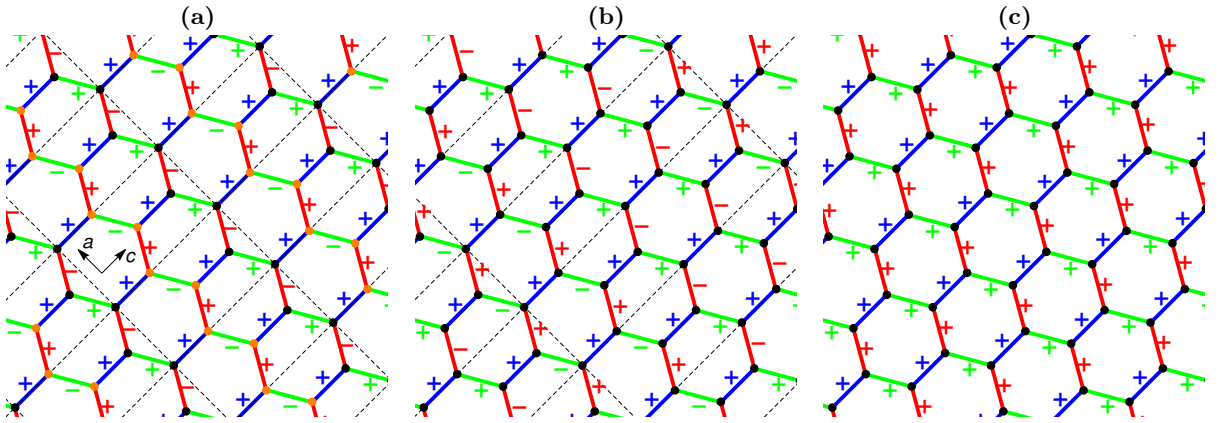


Figure 3.8: Signs of the Γ interaction in the projected hyperhoneycomb-lattice (a), striphoneycomb-lattice (b) models and the honeycomb model (c). Dashed rectangles in (a) and (b) mark the primitive unit cells.

In that sense we call the x (y) and z bonds non-twisting and twisting bonds, respectively.

The next lattice in this series is the striphoneycomb lattice as displayed in Fig. 3.7 (b). Here we can find each a row of honeycomb plaquettes which are connected by the twisting z bonds and thus call the lattice $\mathcal{H}\langle 1 \rangle$. The stripy honeycomb lattice can be built from the hyperhoneycomb lattice by rotating the neighbored bonds of the corresponding z bonds into the same plane such that these z bonds become non-twisting bonds. Analogously to the hyperhoneycomb lattice, there exist C_a^* , C_b^* , and C_c^* symmetry operations where the rotation axes pass the center of the twisting z bond. Furthermore, there exists a inversion symmetry with the center in the middle of the honeycomb plaquette.

We can also define a Heisenberg-Kitaev- Γ model like in Equation (3.3) for the striphoneycomb lattice [17]. The symmetry transformations fix the relative signs of the Γ term for the x and y bonds. Again, the z bonds are not symmetry connected to the x (y) bonds and further twisting and non-twisting z bonds are not equivalent. For simplicity we choose a Γ term on all z bonds with the same strength and a relative $+$ sign.

The next lattices in the harmonic honeycomb series can be constructed as shown in Fig. 3.7 (d)-(f). Due to

the larger number of sites per unit cell it is not more possible to fix the relative signs of the Γ interaction for x and y bonds by symmetry reasons.

For the $\mathcal{H}\langle N \rangle$ series, the lattice vectors can be written in compact form. The corresponding orthorhombic unit cell will be extended in the c direction. For $\mathcal{H}\langle 2N \rangle$ and $\mathcal{H}\langle 2N + 1 \rangle$, the orthorhombic unit cell has same length in the a and b directions, but

$$c = (2N + 1) [6, 6, 0] \text{ for } \mathcal{H}\langle 2N \rangle \text{ and } c = (N + 1) [6, 6, 0] \text{ for } \mathcal{H}\langle 2N + 1 \rangle. \quad (3.8)$$

The primitive unit vectors of the $\mathcal{H}\langle 2N \rangle$ lattice are

$$\mathbf{a}_1 = [2, 4, 0] + N [6, 6, 0], \quad \mathbf{a}_2 = [3, 3, 2] + N [6, 6, 0], \quad \mathbf{a}_3 = [-1, 1, 2], \quad (3.9)$$

and for the $\mathcal{H}\langle 2N + 1 \rangle$ lattice

$$\mathbf{a}_1 = (N + 1) [6, 6, 0], \quad \mathbf{a}_2 = [-2, 2, 0], \quad \mathbf{a}_3 = [-1, 1, 2]. \quad (3.10)$$

The difference between even and odd $\mathcal{H}\langle N \rangle$ lattices is that they have a face-centered and base-centered orthorhombic structure, respectively.

At the end of the series, there is the honeycomb lattice $\mathcal{H}\langle \infty \rangle$. For $\mathcal{H}\langle \infty \rangle$ there can be chosen an orthorhombic unit cell with the same shape as for the hyperhoneycomb and stripyhoneycomb lattices. Note that this $\mathcal{H}\langle \infty \rangle$ lattice is a real three-dimensional lattice with layers of two-dimensional honeycomb lattices. Due to the ABC stacking of the honeycomb layers in this case, the C_3 rotation symmetry is broken and thus the z bonds are not symmetry equivalent to the x (y) bonds.

The projection to the honeycomb lattice works for all harmonic honeycomb lattices. In contrast to the projection of the hyperhoneycomb model, see Fig. 3.8 (a), the unit cell of the projected $\mathcal{H}\langle N \rangle$ model has a more enlarged unit cell due to the lower symmetry of the model. This is illustrated in Fig. 3.8 (b), where the projected Heisenberg-Kitaev- Γ model for the stripyhoneycomb lattice is shown. The projection of $\mathcal{H}\langle \infty \rangle$ agrees with the original honeycomb model, as displayed in Fig. 3.8 (c).

3.4 1D Kitaev systems

Typical lattices which exhibit Kitaev physics are three-coordinated like the two dimensional honeycomb lattice and the three dimensional hyperhoneycomb lattice. This type of lattice also exists for the one-dimensional case. It is possible to define the so-called Kitaev ladder [34] which is illustrated in Fig. 3.9 (a). Here, the z bonds are the 'rungs' of the ladder while the x and y bonds are the 'legs'. This choice distinguishes the z bonds since a minimal loop contains two z bonds but each one x and y bond. Choosing a snake line along the x and z bonds, there exists an equivalent linear-chain representation of the Kitaev ladder, as shown in Fig. 3.9 (b). While the x and z interactions stay nearest-neighbor interactions, the y interaction is mapped to a third-neighbor interaction in the linear chain.

The Kitaev ladder can be built from the honeycomb lattice by a projection-like mapping [34]. Considering Fig. 3.8 (a), the projection of the honeycomb lattice to the line perpendicular to the z bonds leads to an effective one-dimensional structure. Through the projection, the length of the z bonds vanishes since each two sites of the four-site unit cell are mapped to the same position. Rescaling the length of the z bonds under retention of the nearest-neighbor geometry leads to the Kitaev-ladder structure.

Like the 3D-2D equivalence, this projection to 1D works also for certain magnetic states. If the magnetic structure on the honeycomb lattice has no modulation along the \hat{c} direction, then the 2D-1D equivalence appears. For single- \mathbf{Q} and multi- \mathbf{Q} states this means that the corresponding wave-vectors \mathbf{Q} have only components in the \hat{a} direction. This analysis clarifies the fact that the z domain of the zigzag and stripy phases can occur

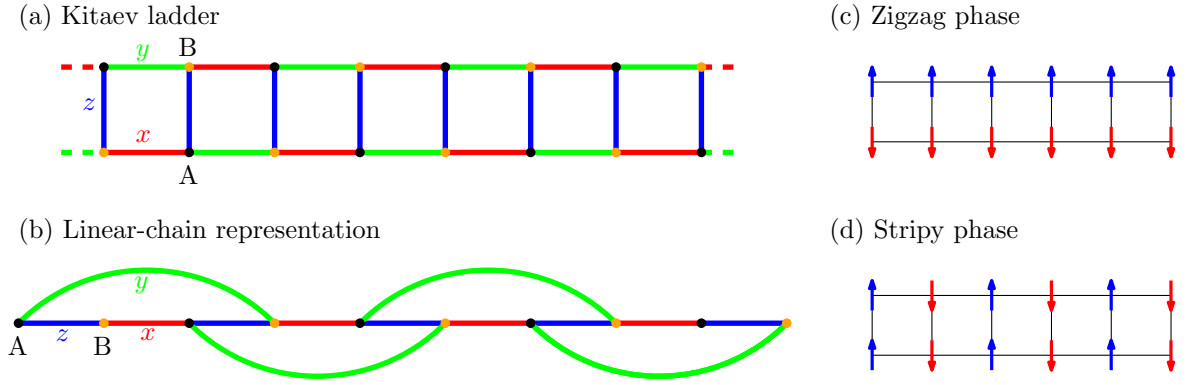


Figure 3.9: (a) The 1D Kitaev ladder with the z bonds as rungs and the x (y) bonds as the legs. It is a bipartite and three-coordinated lattice. (b) An equivalent representation of the Kitaev ladder. A snake-line path along the x and z bonds in (a) transforms the y interaction to a third-neighbor interaction in the linear chain. Like for the honeycomb lattice, there exist a zigzag (c) and a stripy phase (d) with red and blue spins pointing in $\pm\hat{z}$ direction.

on the Kitaev ladder, see Figs. 3.9 (c) and (d), but the x and y domains are not possible since they have a modulation along \hat{c} on the honeycomb lattice. Due to the fact, that the FM, Néel, zigzag, and stripy phases appear for the Kitaev ladder with exact the same energy like for the honeycomb lattice, it is sufficient to argue that the corresponding classical phase diagrams of the Heisenberg-Kitaev model are the same.

For the Heisenberg-Kitaev model in an external field, this 2D-1D mapping works for the honeycomb phases with ordering wave-vector $\mathbf{Q} = \mathbf{K}$, mentioned vortex and AF-vortex phases. However, the AF-star and FM-star phases are multi- \mathbf{Q} phases with a modulation in the \hat{c} direction. Thus, these phases can not occur for the Kitaev ladder in a magnetic field.

Since the Heisenberg-Kitaev- Γ model for the hyperhoneycomb lattice can be mapped to the 1D Kitaev ladder, even the incommensurate spiral states $\overline{\text{SP}}_{a\pm}$ can be described within this 1D ladder model.

Beyond the classical limit, this 2D-1D equivalence holds also for the magnon spectrum obtained by linear spin-wave theory. That means, the magnon spectrum for the Kitaev ladder is the same as the spectrum for the honeycomb lattice with the wave-vector \mathbf{q} in the \hat{a} direction, e.g., for the path $\Gamma - \mathbf{E}$ as shown in Fig. 3.5. Since the 3D-2D equivalence holds for this particular direction, the corresponding hyperhoneycomb spectrum is also equivalent.

To sum up, the quantitative projective equivalence of ordered states, classical energies and magnon-excitation energies for Kitaev models is present from the 3D hyperhoneycomb lattice over the 2D honeycomb lattice to the 1D Kitaev ladder.

4 Heisenberg-Kitaev- Γ model on the hyperhoneycomb and projected lattices

The advertised mapping of the last section projects the Heisenberg-Kitaev model on the hyperhoneycomb lattice to a corresponding honeycomb-lattice model. For a Heisenberg-Kitaev in an external magnetic field, this leads to a phase diagram for which most of the occurring phases can be projected within that mapping, as worked out in section 2. By including an offdiagonal Γ term, the projected and honeycomb models are no longer thermodynamically equivalent. It will be of interest to know whether the quasi-2D nature of phases is true also in this case.

The Hamiltonian of the Heisenberg-Kitaev- Γ model for the hyperhoneycomb lattice is

$$\mathcal{H}_{\text{HK}\Gamma} = \sum_{\langle ij \rangle_\gamma} \left[J \vec{S}_i \cdot \vec{S}_j + K S_i^\gamma S_j^\gamma \pm \Gamma \left(S_i^\alpha S_j^\beta + S_i^\beta S_j^\alpha \right) \right]. \quad (4.1)$$

The symmetries and approaches for this model Hamiltonian are discussed in detail in section 3.2.2. To demonstrate whether the 3D-2D mapping holds for this kind of model, we investigate the classical phase diagrams for the hyperhoneycomb-lattice and projected-lattice models.

The phase diagram for the hyperhoneycomb model has been computed earlier using a combination of Monte-Carlo and Luttinger-Tisza techniques [17]. In the following, we recompute this phase diagram and the corresponding honeycomb-lattice diagram using a slightly different method, which allows a detailed comparison between the different lattices.

4.1 Methods

Because of the expected nature of the phase diagram with large parts filled by incommensurate spiral phases, we use a combination of the Luttinger-Tisza approach and a single- \mathbf{Q} ansatz to find the ground state.

The Luttinger-Tisza approach was introduced for models with a quadratic form of the spin interaction in the Hamilton operator on Bravais lattices [35], but it can be extended to models with enlarged unit cells and inequivalent spins, i.e., spins of different length [36]. For the actual model, all spins have the same length and the spin $\vec{S}_{n\nu}$ in the unit cell n on the sublattice ν fulfills the so-called strong spin constraint

$$|\vec{S}_{n\nu}|^2 = 1. \quad (4.2)$$

This is true for all n and ν . The idea of the Luttinger-Tisza approach is to replace this strong spin constraint by the weak spin constraint

$$\sum_{n,\nu} |\vec{S}_{n\nu}|^2 = 4N, \quad (4.3)$$

where N denotes the number of unit cells and 4 is the number of sublattices of the hyperhoneycomb lattice. The weak spin constraint satisfies that the average norm square of each spin is 1. Further, the weak constraint (4.3) is invariant under a unitary transformation, in particular, the Fourier transformation. The energy minimization becomes simple for the Fourier transformed spins. The resulting spin state has then to be checked for the strong spin constraint (4.2). If it is satisfied, then the true ground state has been found. However, if the state does not fulfill the strong constraint, the Luttinger-Tisza approach has failed. Nevertheless, the resulting energy represents a strict lower bound for the true ground state energy. The procedure is described in detail in Appendix C.

The second method used is a single- \mathbf{Q} ansatz. Here, we make an explicit ansatz for the spin \vec{S}_a at the lattice

position \mathbf{r} and express the spin as

$$\vec{S}_a(\mathbf{r}) = \sin \eta_a [\hat{\mathbf{e}}_a^x \cos(\mathbf{Q} \cdot \mathbf{r}) + \hat{\mathbf{e}}_a^y \sin(\mathbf{Q} \cdot \mathbf{r})] + \cos \eta_a \hat{\mathbf{e}}_a^z, \quad (4.4)$$

where a denotes the sublattice of the spin, $\{\hat{\mathbf{e}}_a^x, \hat{\mathbf{e}}_a^y, \hat{\mathbf{e}}_a^z\}$ is an arbitrary coordinate system, η_a is a canting angle and \mathbf{Q} is a wave-vector inside the first Brillouin zone. The coordinate system $\{\hat{\mathbf{e}}_a^x, \hat{\mathbf{e}}_a^y, \hat{\mathbf{e}}_a^z\}$ can be parametrized by three Euler angles. Note that all these parameters, except \mathbf{Q} , depend on the sublattice position $a = 1, 2, 3, 4$ on the hyperhoneycomb lattice. To find the ground-state, we have to minimize the energy of the corresponding spin state for all free parameters. For the minimizing wave-vector \mathbf{Q} , the state has Bragg peaks at $\pm \mathbf{Q}$ and also at Γ if $\cos \eta_a \neq 0$ for some a . The method of the single- \mathbf{Q} ansatz is illustrated in detail in Appendix D. The described methods are not able to find multi- \mathbf{Q} state which may be important for a small part of the phase diagram [17].

4.2 Phases and phase diagrams

The couplings of the Heisenberg-Kitaev- Γ model can be parametrized as

$$(J, K, \Gamma) = A(\sin \vartheta \cos \varphi, \sin \vartheta \sin \varphi, \cos \vartheta), \quad (4.5)$$

with the overall energy scale $A > 0$, $\vartheta \in [0, \pi]$ and $\varphi \in [0, 2\pi)$. We will focus on the case $\Gamma \leq 0$, i.e., $\vartheta \in [\frac{\pi}{2}, \pi]$, because this seems to be the experimentally relevant case [17].

Due to the accidental SU(2) degeneracy of ordered phases of the classical Heisenberg-Kitaev model, the Néel, zigzag, FM, and stripy phase are highly degenerate in the limit $\Gamma = 0$, which corresponds to the outer border of the circular phase diagram Fig. 4.1. In the presence of a finite Γ term, this degeneracy is reduced and the spins are locked to special spatial directions.

The eight-sublattice duality transformation introduced in Section 2.2 which connects the left and the right boundary of the phase diagram, is no longer useful for a finite Γ since the duality transformation maps the Γ interaction to a model which is not captured by the model Hamiltonian (4.1), i.e., the left and right interiors of the phase diagram are not related.

For the hyperhoneycomb model, we find in total 11 different phases for a finite Γ . There are six phases that can not directly be connected to one of the ordered states of the pure Heisenberg-Kitaev model, namely the incommensurate spiral phases $\overline{\text{SP}}_{a+}$, $\overline{\text{SP}}_{a-}$, $\overline{\text{SP}}_{b+}$ and $\overline{\text{SP}}_{b-}$ and also the commensurate AF $_{abc}$ and FM-SZ $_{\text{FM}}$ phases, which border the highly degenerate Kitaev ($\vartheta = \frac{\pi}{2}$, $\varphi = \frac{\pi}{2}, \frac{3\pi}{2}$) and Γ ($\vartheta = \pi$) points, respectively. The remaining five phases are connected continuously to the ordered states of the Heisenberg-Kitaev model. The SZ $_{x,y}$ and SZ $_b$ phases are connected to the zigzag phase, the FM $_c$ phase is connected to the FM phase, the SS $_{x,y}$ phase is connected to the stripy phase, and the AF $_c$ phase is connected to both, the stripy phase and the Néel phase. The corresponding phase diagram is shown in Fig. 4.1 (a).

The phase diagram of the projected model, displayed in Fig. 4.1 (b), contains in total 8 phases which have all their equivalent counterparts on the hyperhoneycomb lattice in terms of the projection. For those parts of the 3D phase diagram where the projection works, the corresponding 3D and 2D phases have quantitatively the same spin orientations, energies and phase boundaries.

Notably, there is a highly degenerate point $(\vartheta, \varphi) = (\pi - \arccos \frac{1}{\sqrt{3}}, \frac{3\pi}{4})$ in the phase diagram which is bordered by the SZ $_b$, FM $_c$, FM-SZ $_{\text{FM}}$, $\overline{\text{SP}}_{a+}$, and $\overline{\text{SP}}_{b+}$ phases in the 3D case and additionally by the Z $_{x/y}$ phase for the 2D model. Here, the absolute value of the couplings $(J, K, \Gamma) \sim (-1, 1, -1)$ is the same and the bond interaction $\mathcal{H}_{\langle ij \rangle_\gamma} \sim (S_i^\alpha \pm S_i^\beta)(S_j^\alpha \pm S_j^\beta) \sim (\delta_{ij} \cdot \vec{S}_i)(\delta_{ij} \cdot \vec{S}_j)$ gets a dipolar form where δ_{ij} is the normalized nearest-neighbor vector.

In the following, we want to discuss the occurring phases of the Heisenberg-Kitaev- Γ model on the hyperhoneycomb and projected lattices. Note that this discussion has previously been done by Lee and Kim for the

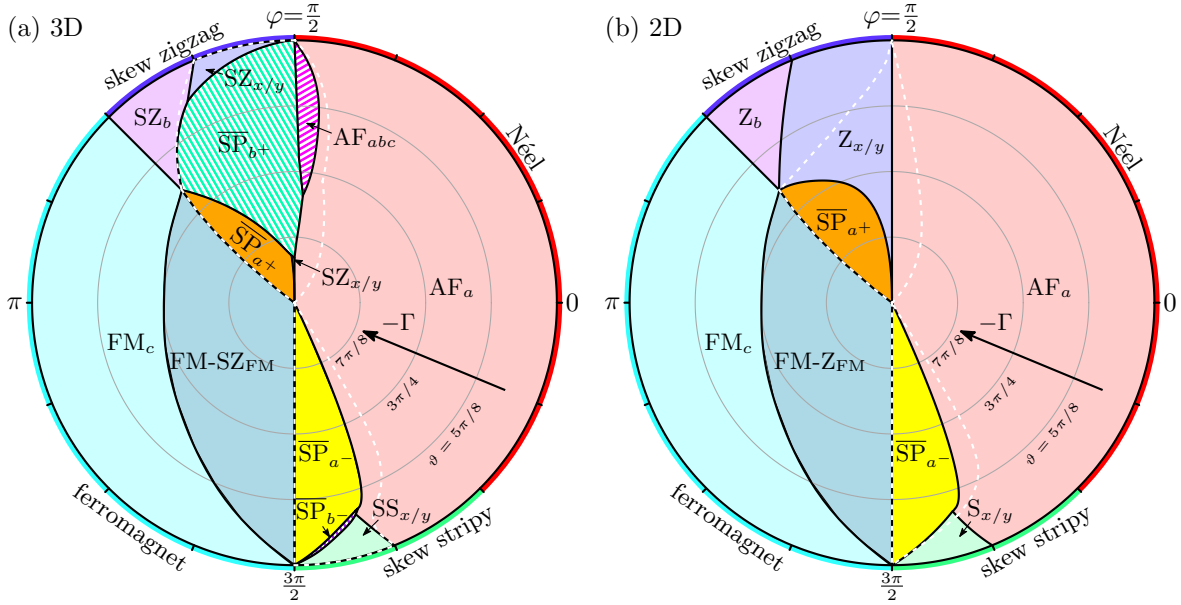


Figure 4.1: Phase diagram of the Heisenberg-Kitaev- Γ model (a) for the hyperhoneycomb lattice and (b) for the projected lattice for $\Gamma \leq 0$ with the parametrization (4.5) where φ is the azimuth angle and ϑ corresponds to the radial component. Thus, the Γ -only point is the center of the circle and the pure Heisenberg-Kitaev model is on the border of the circle.

hyperhoneycomb model, but not under the aspect of the 3D-2D equivalence of states and not for the planar honeycomb model with an alternating sign structure in the Γ term. Thus, the following discussion is partly equivalent to that one from reference [17].

FM_c : This ferromagnetic phase is bordered by the FM phase in the limit $\Gamma = 0$ and the spins are locked in the \hat{c} direction. Since the Heisenberg-Kitaev model possess an emergent $SU(2)$ symmetry and the energy contributions for the Γ interaction of the x and y bonds cancel due to the alternating sign of the Γ term, the only symmetry breaking contribution to the energy of a ferromagnetic state is the z -bond Γ -interaction $\sim \Gamma S^x S^y$, which is minimized for $\mathbf{S}_i \parallel \hat{c}$ if $\Gamma < 0$. The FM_c phase can be verified via the Luttinger-Tisza approach as the exact ground state.

AF_a : The AF_a phase captures a large part of the phase diagram. The \hat{a} component of the spins orders antiferromagnetic, while the \hat{b} component orders in a stripy order along the z bonds and the \hat{c} component vanishes. Due to the mixture of Néel and stripy order, the AF_a phase can be continuously connected to the Néel and stripy phases of the Heisenberg-Kitaev model. The Luttinger-Tisza approach captures this phase but fails near the phase boundaries for finite Γ .

SZ_b : The SZ_b phase can also be justified by the Luttinger-Tisza method and it borders the Heisenberg-Kitaev zigzag phase. Here, the \hat{b} component orders in the zigzag order along the xy zigzag chains. By that reason, the phases for the 3D and 2D models are called SZ_b for skew-zigzag and Z_b for zigzag phase, respectively.

$SZ_{x,y}$: There is a second phase connected to the Heisenberg-Kitaev zigzag phase, mentioned the $SZ_{x,y}$ phase. The \hat{x} (\hat{y}) component of the spins is the largest component and orders in the zigzag order along the yz (xz) zigzag chains. The x and y domains are degenerate. The Luttinger-Tisza approach fails here for the 3D $SZ_{x,y}$ phase, but works at least for a part of the parameter region where the 2D $Z_{x,y}$ phase is assumed to be the ground state. In the 3D phase diagram, there is still a small part of the $SZ_{x,y}$ phase bordered by the \overline{SP}_{a+} , \overline{SP}_{b+} , AF_a phases and the pure Γ point, which is not directly connected to the rest of the $SZ_{x,y}$ region. This can be understood with the help of the phase diagram for the projected model. Here, the region of the $Z_{x,y}$ phase connects directly the Heisenberg-Kitaev zigzag phase and the pure Γ point. However, in the 3D case there exists the \overline{SP}_{b+} phase which overlaps the region of the 2D $Z_{x,y}$ phase partly and thus leads to two disconnected regions of the $SZ_{x,y}$ phase.

$SS_{x,y}$: On the other side of the phase diagram, there exists a stripy counterpart of the $SZ_{x,y}$ phase. In the $SS_{x,y}$ phase, the $\hat{\mathbf{x}}$ ($\hat{\mathbf{y}}$) component of the spins orders in the stripy order along the x (y) stripes, while the other spin components are small. These two configurations are degenerate. Again, the Luttinger-Tisza method fails for the 3D case but captures the $S_{x,y}$ phase as the true ground state for the 2D model.

$FM-SZ_{FM}$: In the ferromagnetic regime, there exists a second phase next to the FM_c phase for small J found by the Luttinger-Tisza approach, dubbed $FM-SZ_{FM}$. Here, the $\hat{\mathbf{a}}$ component of the spins orders in the zigzag order along the xy chains and the $\hat{\mathbf{b}}$ component orders ferromagnetic. This phase is bordered by the $J = 0$ line between the Γ and the FM Kitaev points and the duality transformation for the Kitaev- Γ model (introduced in section 3.2.3) maps the $FM-SZ_{FM}$ phase to a ferromagnet.

AF_{abc} : Near the AF Kitaev point, there is stabilized the AF_{abc} phase only for the 3D model. Here, the spin in the type I xy zigzag chain order antiferromagnetically while the spins in type II xy zigzag chains order in stripes, i.e., every spin has a ferromagnetic and an antiferromagnetic neighbor in the zigzag chain. Since the ordering wave-vector is $\mathbf{Q} = \mathbf{L}$, there exist symmetry equivalent domains. The AF_{abc} phase is only found by the single- \mathbf{Q} ansatz. However, large-scale Monte-Carlo simulations show that the true ground state in this parameter region may be a multi- \mathbf{Q} phase [17].

The remaining states of the phase diagram are the spiral phases \overline{SP}_{a+} , \overline{SP}_{a-} , \overline{SP}_{b+} , and \overline{SP}_{b-} , which can be found by the single- \mathbf{Q} ansatz (4.4). The corresponding wave-vectors \mathbf{Q} lie in the crystallographic $\hat{\mathbf{a}}$ and $\hat{\mathbf{b}}$ directions what is marked by the subindices a and b , respectively. Since the $\cos \eta_a \hat{\mathbf{e}}_a^z$ term in the ansatz vanishes by energy minimization, the spiral phases have no total magnetization and the spins on each sublattice are coplanar. The corresponding plane is called spiral plane of the sublattice. The sites of each sublattice border three nearest-neighbor bonds which belong to the corresponding honeycomb plane. For the $+$ phases, the spiral plane of each sublattice corresponds approximatively to the honeycomb plane of the same sublattice, while for the $-$ phases, the spiral plane of the sublattice is approximatively the other honeycomb plane of the lattice.

Another feature that is shared by all of these spiral phases is the so-called counter rotation. Each xy zigzag chain contains two crystallographic sublattices. On these sublattices, the spins along the zigzag chain rotate clockwise and counter-clockwise, respectively.

The \overline{SP}_{b+} and \overline{SP}_{b-} phases are stabilized near the AF and FM Kitaev points only for the 3D model, respectively. Since the ordering wave-vectors \mathbf{Q} have only a \mathbf{b}^* component, the 3D-2D mapping does not work for both phases and thus the 2D phase diagram differs from the 3D phase diagram in these regions. While the \overline{SP}_{b-} phase occupies only a small part of the phase diagram, the \overline{SP}_{b+} phase is stabilized for a larger parameter region which contains also a part of the Kitaev- Γ line.

On the other hand, the \overline{SP}_{a+} and \overline{SP}_{a-} phases are the ground states near the Γ point with the \overline{SP}_{a-} phase is also stabilized in the FM Kitaev limit. The ordering wave-vector \mathbf{Q} for these phases lies in the \mathbf{a}^* direction, thus the 3D-2D mapping works even for these incommensurate phases. The shape of the \overline{SP}_{a+} and \overline{SP}_{a-} phases is a bit larger in the 2D phase diagram since the bordering \overline{SP}_{b+} and \overline{SP}_{b-} phases in the 3D phase diagram do not exist for the 2D model.

Fig. 4.2 shows the spin configurations of the different spiral phases for the 3D and 2D models. The main features of all phases are summarized in Table 4.1.

4.3 Relation to the honeycomb model

Since a large part of the Heisenberg-Kitaev- Γ model for the hyperhoneycomb lattice contains quasi-2D phases, one can ask, whether and in which manner these quasi-2D phases are related to the phases of the Heisenberg-Kitaev- Γ model for the honeycomb lattice. For the honeycomb lattice, the sign of the Γ term is equal on each bond due to the presence of the C_3 rotation symmetry. Further, the strength of the couplings are the same for each bond, i.e., we do not need to approximate this in contrast to the hyperhoneycomb model. However,

Table 4.1: Phases of the Heisenberg-Kitaev- Γ model on the hyperhoneycomb lattice for $\Gamma < 0$ with the corresponding ordering wave-vector \mathbf{Q} . The phases are dubbed quasi 2D (genuine 3D) when they have (no) modulation along the crystallographic $\hat{\mathbf{b}}$ direction and thus can (not) be projected to the honeycomb model.

phase	3D-2D correspondence	\mathbf{Q}	Comments
$\overline{\text{FM}}_c$	quasi 2D	Γ	$\mathbf{S}_i \parallel \hat{\mathbf{c}}$
$\overline{\text{FM-SZ}}_{\text{FM}}$	quasi 2D	Γ	$\mathbf{S}_i \cdot \hat{\mathbf{a}}$: zigzag, $\mathbf{S}_i \cdot \hat{\mathbf{b}}$: FM
$\overline{\text{AF}}_a$	quasi 2D	Γ	$\mathbf{S}_i \cdot \hat{\mathbf{a}}$: Néel, $\mathbf{S}_i \cdot \hat{\mathbf{b}}$: stripy
$\overline{\text{SZ}}_b$	quasi 2D	Γ	$\mathbf{S}_i \cdot \hat{\mathbf{b}}$: zigzag
$\overline{\text{SZ}}_{x,y}$	quasi 2D	\mathbf{Y}	$\mathbf{S}_i \cdot \hat{\mathbf{x}}$ or $\mathbf{S}_i \cdot \hat{\mathbf{y}}$: zigzag (degenerate)
$\overline{\text{SS}}_{x,y}$	quasi 2D	\mathbf{Y}	$\mathbf{S}_i \cdot \hat{\mathbf{x}}$ or $\mathbf{S}_i \cdot \hat{\mathbf{y}}$: stripy (degenerate)
$\overline{\text{AF}}_{abc}$	genuine 3D	\mathbf{L}	xy chain type I: AF, xy chain type II: stripy
$\overline{\text{SP}}_{a+}$	quasi 2D	$(a, 0, 0)$	incommensurate spiral
$\overline{\text{SP}}_{a-}$	quasi 2D	$(a, 0, 0)$	incommensurate spiral
$\overline{\text{SP}}_{b+}$	genuine 3D	$(0, b, 0)$	incommensurate spiral
$\overline{\text{SP}}_{b-}$	genuine 3D	$(0, b, 0)$	incommensurate spiral

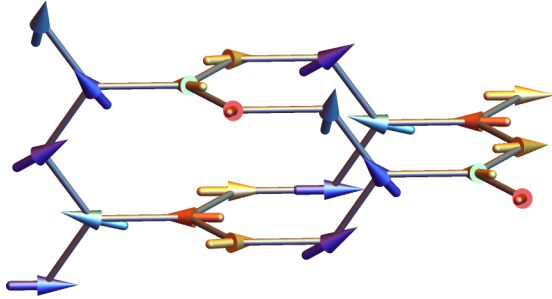
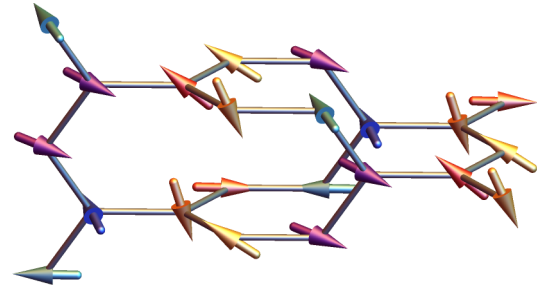
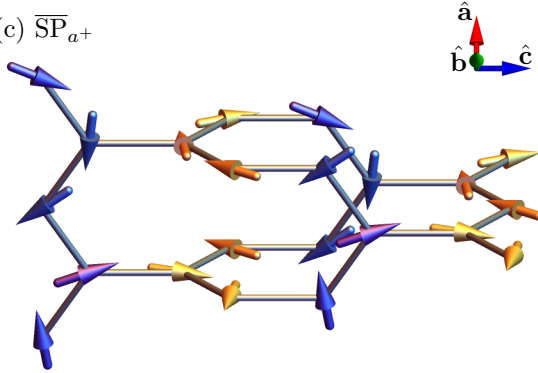
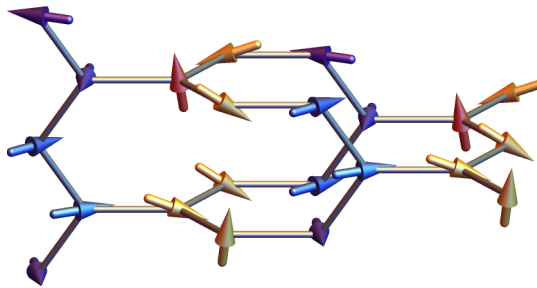
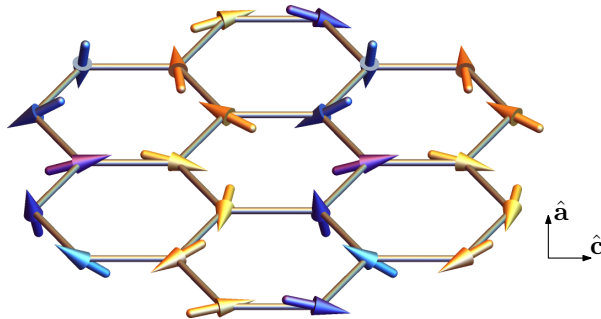
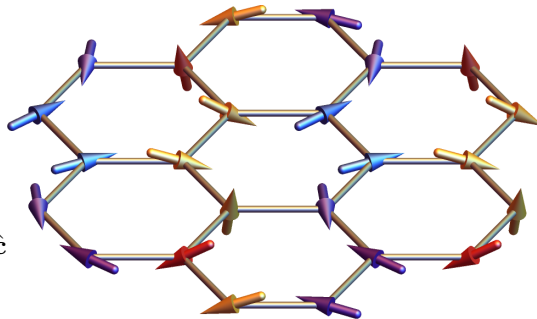
(a) $\overline{\text{SP}}_{b+}$ (b) $\overline{\text{SP}}_{b-}$ (c) $\overline{\text{SP}}_{a+}$ (d) $\overline{\text{SP}}_{a-}$ (e) $\overline{\text{SP}}_{a+}$, 2D(f) $\overline{\text{SP}}_{a-}$, 2D

Figure 4.2: Spin configurations for the incommensurate spiral phases on the hyperhoneycomb lattice, (a) the $\overline{\text{SP}}_{b+}$ phase for $(\vartheta, \varphi) = (0.8\pi, 0.55\pi)$, (b) the $\overline{\text{SP}}_{b-}$ phase for $(\vartheta, \varphi) = (0.545\pi, 1.55\pi)$, (c) the $\overline{\text{SP}}_{a+}$ phase for $(\vartheta, \varphi) = (0.85\pi, 0.65\pi)$ and (d) the $\overline{\text{SP}}_{a-}$ phase for $(\vartheta, \varphi) = (0.7\pi, 1.55\pi)$. Panels (e) and (f) show the same phases as (c) and (d) but for the projected lattice.

in real three-dimensional materials, the honeycomb planes may be stacked not in an A-A manner what breaks the C_3 symmetry. We will discuss only the planar honeycomb model in the following.

The phase diagram of the Heisenberg-Kitaev- Γ model for the honeycomb lattice is shown in Fig. 4.3 for $\Gamma \leq 0$. This honeycomb-model phase diagram is reproduced from reference [37] where it is shown for the case $\Gamma \geq 0$. We can map this $\Gamma \geq 0$ phase diagram to the $\Gamma \leq 0$ phase diagram by the following transformation. The spins on the odd sublattices are inverted what leads to the transformation of the couplings $(J, K, \Gamma) \rightarrow (-J, -K, -\Gamma)$. The phase diagram is also inverted under this transformation, while FM and AF bonds and also stripy and zigzag are interchanged. Although this transformation works in the classical case, the transformed spins do not satisfy the canonical commutation relation and thus the $\Gamma \geq 0$ and $\Gamma \leq 0$ phase diagrams are not related in the quantum case.

The FM, Néel, stripy, and zigzag phases have a $SU(2)$ degeneracy for $\Gamma = 0$ but they are locked or have a lower degeneracy for finite Γ . Since the signs of the Γ term differs for the honeycomb and projected hyperhoneycomb models, the locking direction for both lattices is generally not the same.

In the honeycomb model, there also occurs the coplanar 120° phase for a finite Γ with spins on the same sublattice have a relative angle of 120° . In the parameter region where the Luttinger-Tisza approach fails, an incommensurate spiral phase (IS) may be the ground state but a recent study shows that incommensurate multi- \mathbf{Q} states are stabilized [38]. Which of these phases is the true ground state is not important since the parameter region of these multi- \mathbf{Q} states is not of interest for our discussion.

4.3.1 The $J \rightarrow 0$ limit

More impressive and maybe of experimental interest are the phases in the vicinity of the Kitaev- Γ model, i.e., the vertical $J = 0$ line. As shown in section 3.2.3, the projected model and the honeycomb model are equivalent in this limit. Since the Luttinger-Tisza approach fails for $\Gamma < 0$ and $K > 0$ for all considered models and the ground state for the hyperhoneycomb lattice realized by the \overline{SP}_{b+} phase seems to be genuine 3D in this region, we restrict to the $\Gamma < 0$ and $K < 0$ line, i.e., the lower half of the $J = 0$ line in the phase diagram. For the hyperhoneycomb model, this line is bordered by the FM-SZ_{FM} and \overline{SP}_{a-} phases which survive the 3D-2D mapping and still border the $\Gamma < 0$ and $K < 0$ line for the projected model. On the other hand, the corresponding Kitaev- Γ line in the honeycomb phase diagram is bordered by the FM and the 120° phases. Since for the pure Kitaev- Γ model there may be a higher degeneracy due to the fact that both, the Kitaev model and the Γ model, contain classically disordered states, the limits of the corresponding phases for the honeycomb and projected models do not necessarily have to agree.

The Luttinger-Tisza method works on the $\Gamma < 0$, $K < 0$ line for the honeycomb and projected models. For the honeycomb model, we find $\mathbf{Q} = \mathbf{\Gamma}$ and $\mathbf{Q} = \mathbf{K}$ as possible ordering wave-vectors which belong to degenerate states. Note, the wave-vector \mathbf{K} on the honeycomb lattice corresponds to $\mathbf{E} = (\frac{1}{3}, 0, 0)$ on the hyperhoneycomb lattice, see Fig. 3.4 (d). For $\mathbf{Q} = \mathbf{\Gamma}$, the ground state is a FM locked in the $[1, 1, 1]$ direction. On the other hand for $\mathbf{Q} = \mathbf{K}$, the ground state is a 120° phase with spins lying in the honeycomb plane. This 120° phase has a $U(1)$ degeneracy. The ground state for the projected model is just the duality transformed ground state of the honeycomb model.

A finite $J < 0$ will choose the locked FM in $[1, 1, 1]$ direction as the ground state for the honeycomb model. For the projected model, a finite $J < 0$ stabilizes the FM-Z_{FM} phase. Here, the $\hat{\mathbf{b}} \parallel \hat{\mathbf{z}}$ component of the spins are ferromagnetic while the $\hat{\mathbf{a}} \parallel (\hat{\mathbf{x}} - \hat{\mathbf{y}})$ component is in a zigzag order along the xy chains. The FM-Z_{FM} phase is mapped under the duality transformation to a FM. In the limit $J \rightarrow 0$, the dual spins are aligned in the $[1, 1, 1]$ direction. Thus, the FM-Z_{FM} phase is adiabatically connected to the FM phase on the honeycomb lattice.

A finite $J > 0$ stabilizes the 120° and \overline{SP}_{a-} for the honeycomb and projected models, respectively. For the 120° phase, the spins are aligned in the honeycomb plane perpendicular to the $[1, 1, 1]$ direction and this phase

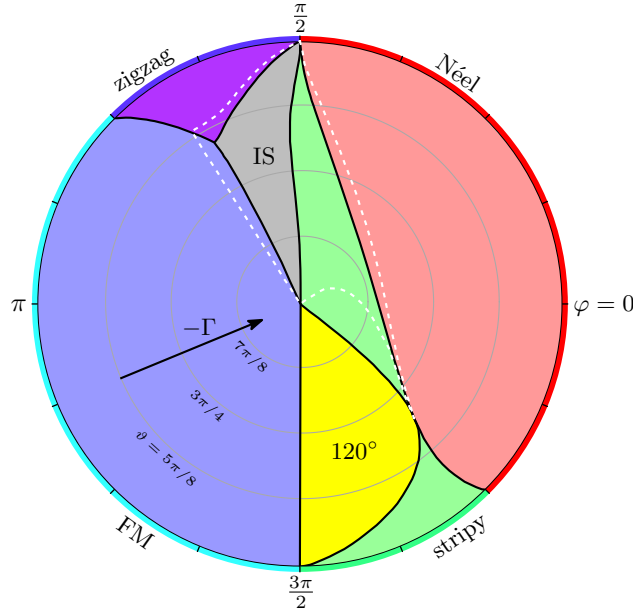


Figure 4.3: Phase diagram of the classical Heisenberg-Kitaev- Γ model for the honeycomb lattice for $\Gamma \leq 0$ with the parametrization (4.5). Here, φ is the azimuth angle and ϑ corresponds to the radial component. Thus, the Γ -only point is the center of the circle and the pure Heisenberg-Kitaev model is on the border of the circle. In the parameter region enclosed by the white dashed line the Luttinger-Tisza approach failed. This phase diagram is reproduced from reference [37] where it is shown for $\Gamma \geq 0$.

posses a $U(1)$ degeneracy. On the other hand, the \overline{SP}_{a-} phase for the projected model is of incommensurate order with the ordering wave-vector \mathbf{Q} be in $\hat{\mathbf{a}}$ direction. In the limit $J \rightarrow 0$, the ordering wave-vector becomes $\mathbf{Q} \rightarrow (\frac{1}{3}, 0, 0) = \mathbf{E}$ what corresponds to the wave-vector $\mathbf{Q} = \mathbf{K}$ of the 120° phase of the honeycomb model. Since the \overline{SP}_{a-} is incommensurate in the crystallographic $\hat{\mathbf{a}}$ direction, we can shift the spin configuration by one crystallographic unit cell in the $\hat{\mathbf{a}}$ direction and get a new domain of the \overline{SP}_{a-} phase. Thus, the \overline{SP}_{a-} phase posses also a $U(1)$ degeneracy. These simple arguments, the same degeneracy and equivalent ordering wave-vectors, leads to the conclusion that the 120° and \overline{SP}_{a-} phases are equivalent in the limit $J \rightarrow 0$, where equivalent means in the presence of the duality transformation.

This equivalence can be varified explicitly with the duality transformation. Fig. 4.4 (a) displays the commensurate spin structure of the \overline{SP}_{a-} phase on the projected lattice in the limit $J \rightarrow 0$. The magnetic unit cell contains 12 spins which all seem to be inequivalent. The duality transformation for the Kitaev- Γ model rotates the spins on the two types of zigzag chains, indicated by spins in red and blue hues, by different angles around the $\hat{\mathbf{z}}$ axis. The transformed spin state is shown in Fig. 4.4 (b) and is equivalent to the 120° phase of the honeycomb model. The duality transformation maps each pairs of spins in different zigzag chains to equivalent dual spins, so the magnetic unit cell of the dual spin structure reduces to a unit cell with 6 inequivalent spins. Within that analysis, the physics of the \overline{SP}_{a-} phase for $J = 0$ can be understood completely by the physics of the 120° phase of the honeycomb lattice, with small modulations for $J > 0$. Physical quantities like heat transport or quantum corections which depend on the dimensionality of the system may be different for the 3D and 2D phases.

The 120° phase has a feature called counter rotating spirals. The spins on different sublattices rotate clockwise and counterclockwise when going along a zigzag chain, respectively. Due to the C_3 symmetry of the honeycomb lattice this is true for all zigzag chains. The Kitaev- Γ duality transformation breaks this C_3 symmetry so that the counter rotation for the projected model is given only along the xy zigzag chains. By using the 3D-2D equivalence, these counter rotating spirals occur also in the 3D \overline{SP}_{a-} phase.

A second interesting feature of the \overline{SP}_{a-} phase can also be explained by the 120° phase. In the 120° phase,

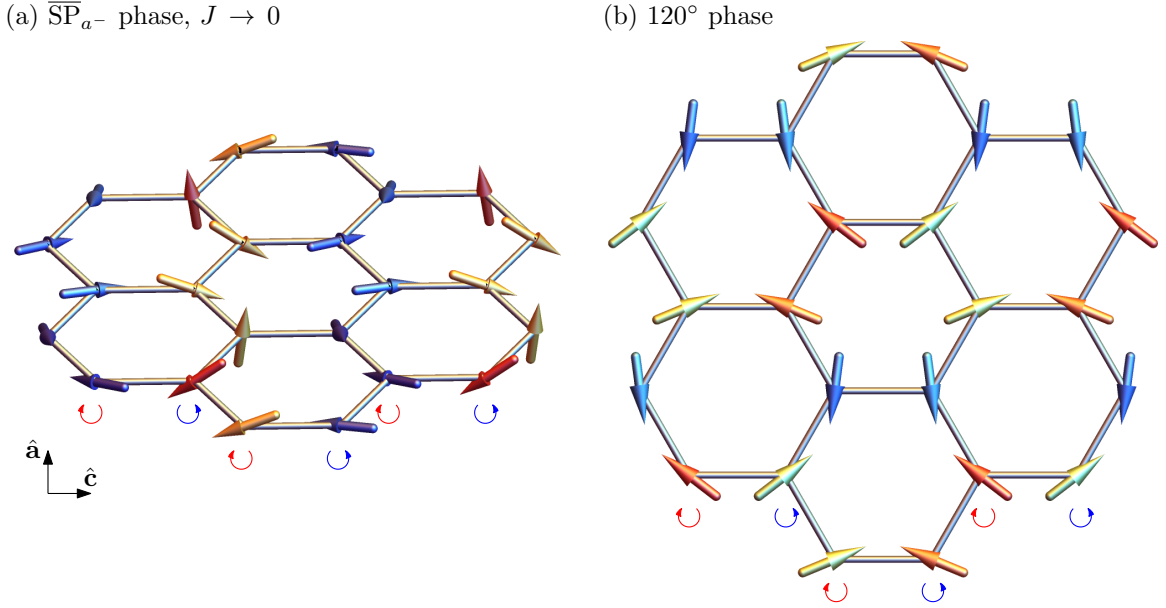


Figure 4.4: (a) The spin configuration of the $\overline{\text{SP}}_{a^-}$ phase for $(\vartheta, \varphi) = (0.7\pi, \frac{3\pi}{2})$ on the projected lattice. The ordering wave-vector $\mathbf{Q} = (\frac{1}{3}, 0, 0)$ gets commensurate for $\varphi = \frac{3\pi}{2}$. (b) The corresponding dual spin configuration with the duality transformation for the Kitaev- Γ model. The honeycomb plane is here perpendicular to the $[1, 1, 1]$ direction and the spins are in plane. This dual spin state is exact that one of the 120° phase of the honeycomb model. Red and blue curly arrows mark the counter rotation of moments.

the spins are coplanar and lie in the honeycomb plane. The Kitaev- Γ duality transforms the spins in the two types of xy chains in another way so that in the corresponding projected model the spins in each xy zigzag chain are coplanar. This feature survives for the 3D model and it turns out that the spins in a zigzag chain are aligned parallel to the honeycomb plane of the other type of zigzag chain. This detail is denoted by the $-$ in $\overline{\text{SP}}_{a^-}$.

4.3.2 The Heisenberg point $K = \Gamma$, $J = 0$

On the $J = 0$ line, there is the special point $K = \Gamma$. The corresponding Kitaev- Γ model can be mapped by a Klein duality transformation to a Heisenberg model. This mapping works for the honeycomb model [31] and also for the hyperhoneycomb model with the restrictions discussed in section 3.2.2 [21]. First we want to discuss the honeycomb case because this will give a clearer insight to the physics of the phases which border this hidden Heisenberg point.

For the choice of parameter $\Gamma \leq 0$, the special point $K = \Gamma$, $J = 0$ can be mapped to a AF Heisenberg model. For the honeycomb model, the corresponding duality transformation has the ordering wave-vector $\mathbf{Q} = \mathbf{K}$ what is illustrated in Fig. 4.5.

By the Klein duality transformation, spins parallel to the honeycomb plane will be mapped to dual spins which are also parallel to the honeycomb plane. On the other hand, spins perpendicular to the honeycomb plane are mapped to dual spins perpendicular to the plane. Let the normal vector of the honeycomb plane be in the $[1, 1, 1]$ direction, then we can write each spin as $\vec{S}_i = \vec{S}_i^{\parallel} + \vec{S}_i^{\perp}$ with $\vec{S}_i^{\parallel} \perp [1, 1, 1]$ and $\vec{S}_i^{\perp} \parallel [1, 1, 1]$ denote the in-plane and out-of-plane components, respectively.

To construct the ground state for $K = \Gamma$, $J = 0$, we start from the AF Heisenberg model using the inverse duality transformation. Here the ground state of the dual spins \vec{S}'_i is the Néel phase. Under the Klein transformation, the spin component \vec{S}'_i^{\perp} is left invariant on one sublattice and flipped on the other sublattice such that the resulting spins have a FM \vec{S}_i^{\perp} component. Thus an AF in the $[1, 1, 1]$ direction is mapped to a FM in the $[1, 1, 1]$ direction.

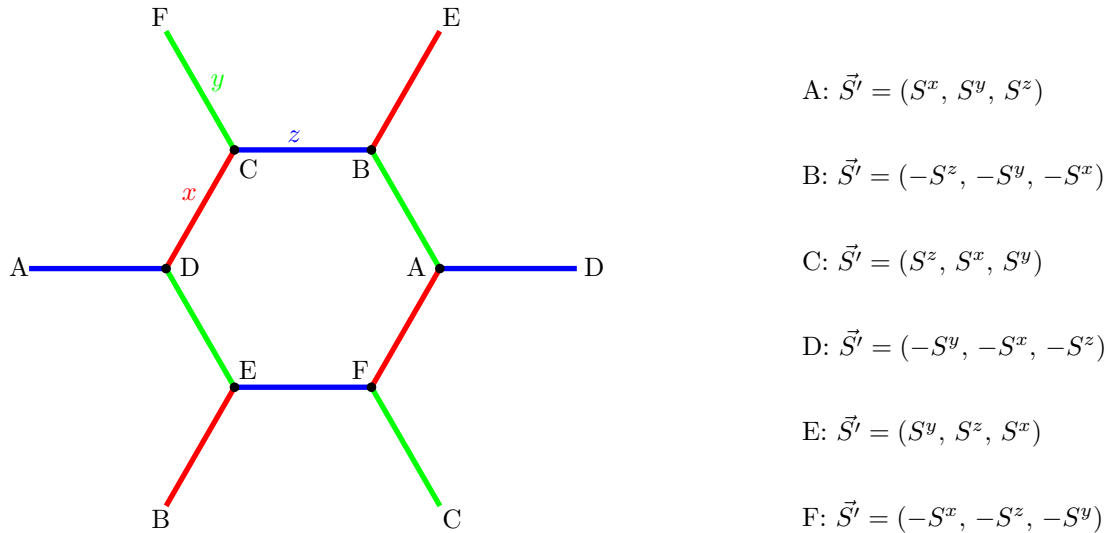


Figure 4.5: The six-sublattice Klein-duality transformation for the honeycomb model which maps the Klein point $K = \Gamma < 0, J = 0$ to the AF Heisenberg point. The transformation has the ordering wave-vector $\mathbf{Q} = \mathbf{K}$. The spins on sublattices A, C and E are rotated around the $[1, 1, 1]$ axis by angles $0, 2\pi/3$ and $4\pi/3$, respectively, while spins on sublattices B, D and F are rotated by an angle of π around the $[-1, 0, 1], [1, -1, 0]$ and $[0, 1, -1]$ axes, respectively. This Klein transformation agrees with the \mathcal{T}_6 transformation found by Chaloupka and Khaliullin [31].

For the in-plane component \vec{S}_i^{\parallel} there is a qualitatively other behavior. On odd sublattices, \vec{S}_i^{\parallel} is either left invariant or rotated by $2\pi/3$ or $4\pi/3$ around the $[1, 1, 1]$ axis by the Klein transformation such that the in-plane spin components \vec{S}_i^{\parallel} have a relative angle of multiples of $2\pi/3$. For the spins on even sublattices, there are three different rotation axes but it is easy to see that the in-plane components \vec{S}_i^{\parallel} also have a relative angle of $2\pi/3$. This is exactly the spin configuration of the 120° phase found for the Heisenberg-Kitaev- Γ model on the honeycomb lattice [37].

Since the in-plane \vec{S}_i^{\parallel} can have an arbitrary direction in the Néel AF, this U(1) degeneracy is transferred to the 120° phase. Since the FM and 120° phase are degenerate, the ground state is a superposition of both and thus has the full hidden SU(2) symmetry. Like for classical Heisenberg-Kitaev model, this SU(2) degeneracy is still present for $K \neq \Gamma$ in the classical limit. However, this SU(2) symmetry can only be present at the Klein point in the quantum case.

Further, this Klein transformation gives more insight into the counter-rotational nature of the 120° phase. Starting from the AF Heisenberg model with the spins in the Néel phase be in-plane, we can show that this counter rotation is a feature of the Klein duality transformation. Using the inverse Klein transformation what is just an interchange of sublattices C and E shown in Fig. 4.5, we consider the xy zigzag chain B-C-D-E-F-A. On the odd sublattices C-E-A there is a clockwise rotation of spins while on the even sublattices B-D-F the spins rotate counterclockwise.

Since the projected model and the honeycomb model are equivalent for $J = 0$, there exists also the Klein point $K = \Gamma$ for the projected model. The duality transformation is here a combination of the Klein duality transformation for the honeycomb model and the Kitaev- Γ duality transformation. This corresponds to a 12-sublattice rotation. Due to the 3D-2D equivalence there exists the same Klein duality transformation for the hyperhoneycomb lattice. Thus, the Klein duality on the 3D lattice is a 12-sublattice transformation in full agreement with previous considerations [21, 39].

For the hyperhoneycomb model, the Néel AF is mapped by the Klein transformation to a superposition of the FM-SZ_{FM} and $\overline{\text{SP}}_{a^-}$ phases. The $\overline{\text{SP}}_{a^-}$ phase has an ideal 120° structure at this Klein point. Since the Néel state is quasi 2D, the Klein transformation ensures the ground state is also quasi 2D in the vicinity of the Klein

point. This argument holds even in the quantum case, if the AF Heisenberg model shows quasi-2D order.

4.3.3 Experimental results

The observed magnetic structures of the iridates α -Li₂IrO₃ [11], β -Li₂IrO₃ [12], and γ -Li₂IrO₃ [13] show a similar behavior. For these Li₂IrO₃ polytypes, which belong to the honeycomb, hyperhoneycomb, and stripyhoneycomb lattices, respectively, the magnetic moments order in an incommensurate spiral structure with counterrotating magnetic moments. For γ -Li₂IrO₃, the experimenters used magnetic resonant x-ray diffraction. On the other hand, for α -Li₂IrO₃ and β -Li₂IrO₃, a combination of single crystal magnetic resonant x-ray diffraction and powder magnetic neutron diffraction was applied to obtain the magnetic structure.

The experimental result for α -Li₂IrO₃ is displayed in Fig. 4.6 (a). A four-site unit cell is chosen and the magnetic propagation vector is found to $\mathbf{q}_\alpha = (0.32(1), 0, 0)$ in the crystallographic (a^* , b , c) basis. This is close to the ordering wave-vector $(1/3, 0, 0)$ of the 120° phase. As the lower panel of Fig. 4.6 (a) shows, the structure in the c direction is homogeneous. This is a hint on a ferromagnetic interlayer exchange interaction. The magnetic moments are approximately perpendicular to the honeycomb layer and counterrotate on the different sublattices along a zigzag chain. The ABC stacking of the honeycomb layers breaks the C_3 symmetry of the lattice. Modeling α -Li₂IrO₃ by a coupled zigzag-chain model leads to the correct observed magnetic order [20]. On the other hand, an isotropic model with second- and third-nearest-neighbor interaction produces also incommensurate spiral order [32]. All of these theoretical studies propose a large ferromagnetic Kitaev coupling and a small antiferromagnetic Heisenberg coupling.

Fig. 4.6 (b) shows the magnetic structure of β -Li₂IrO₃. The orthorhombic unit cell contains 16 sites. The magnetic propagation vector is $\mathbf{q}_\beta = (0.57(1), 0, 0)$ in the crystallographic (a , b , c) basis. This is much more away from an ideal 120° configuration with ordering wave-vector $(2/3, 0, 0)$ than in the α -Li₂IrO₃ case what can be explained by the presence of a weak antiferromagnetic Heisenberg coupling as discussed in the previous sections. The plane of rotation of the magnetic moments is the same for all sublattices in a zigzag chain but is alternating between neighboring zigzag chains as illustrated by the shaded ellipses in Fig. 4.6 (b). β -Li₂IrO₃ shows also a counterrotation of moments.

Since for the α -Li₂IrO₃ lattice the same orthorhombic unit cell as for β -Li₂IrO₃ can be chosen, we can express the propagation vector $\mathbf{q}'_\alpha = (0.64, 0, 0)$ in this new basis. The similar features of the α - and β -Li₂IrO₃ structures can be explained by the Kitaev- Γ duality transformation discussed in section 4.3.1 because β -Li₂IrO₃ has a quasi-2D order. The magnetic moments for α -Li₂IrO₃ are coplanar. The duality transformation rotates the moments differently for neighboring zigzag chains what fully agrees with the different planes of moment rotation observed in β -Li₂IrO₃. On the other hand, the duality transformation captures the counterrotation of moments. The deviation from the ideal 120° structure in β -Li₂IrO₃ corresponds to the strength of the antiferromagnetic Heisenberg coupling what corresponds to the ratio of the ordering wave-vectors $q_\beta/q_\alpha = 0.89$. It seems to be a curiosity that the experimentally found ordering wave-vector for γ -Li₂IrO₃ is exactly the same as for β -Li₂IrO₃. As theoretical studies for the Heisenberg-Kitaev- Γ model on these two lattices have shown, nearly all phases for the hyperhoneycomb lattice β -Li₂IrO₃ exist also for the stripyhoneycomb lattice γ -Li₂IrO₃ [17]. These two facts are a strong hint on that the underlying microscopic couplings are similar for β -Li₂IrO₃ and γ -Li₂IrO₃.

All in all, the experimental results for the different Li₂IrO₃ polytypes show similar physics for 3D and effective 2D Kitaev materials. This can be explained by the presence of just a small Heisenberg coupling.

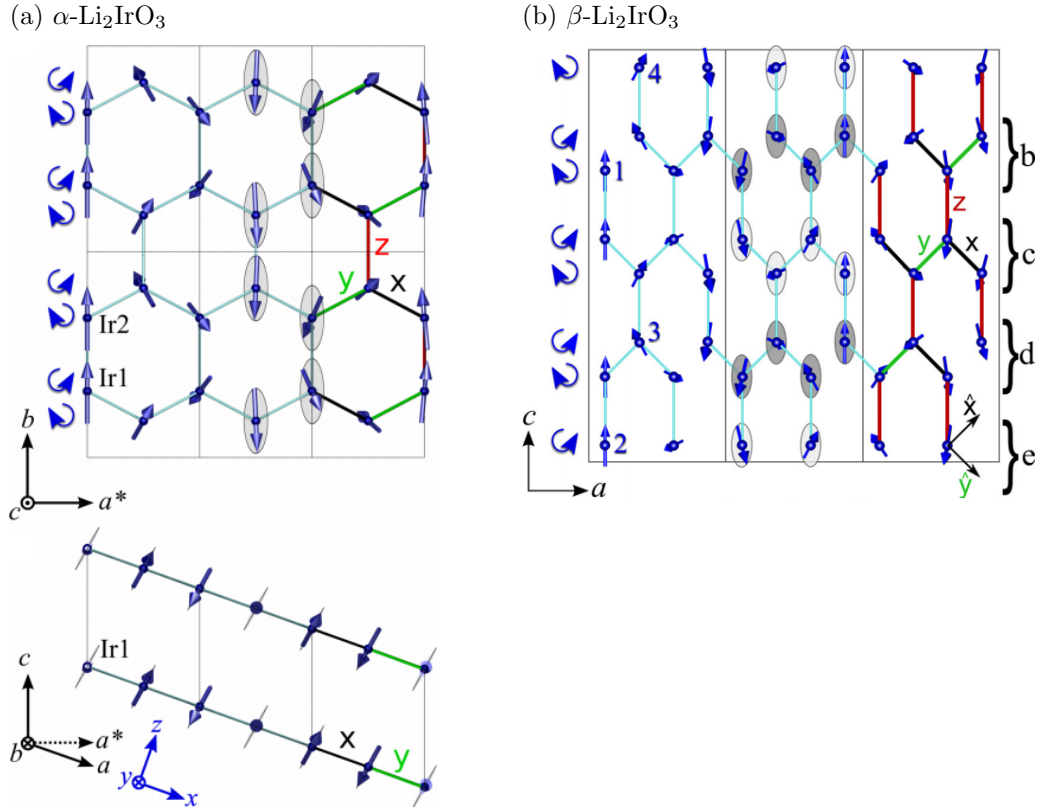


Figure 4.6: (a) Magnetic structure of α - Li_2IrO_3 . The crystallographic directions a^* , b , c belong to the a , c , b directions of the \mathcal{H}_∞ displayed in Fig. 3.7 (c). The upper plot shows the projection of the magnetic structure into the a^*b plane while the lower plot displays the structure for two different honeycomb planes showing ferromagnetic order in the crystallographic c direction. The magnetic propagation vector is along the a^* direction. (b) Magnetic structure of β - Li_2IrO_3 projected into the ac -plane with a magnetic propagation vector in the a direction. The curly arrows indicate the counter rotation of the magnetic moments in the (a) a^* and (b) a directions, respectively. Shaded elliptical envelopes mark the plane of the moment rotation tilted away from the projection plane with an alternating plane structure for β - Li_2IrO_3 . The panels are adapted from References [11] and [12], respectively.

5 Quantum corrections in 3D and 2D

The advertised mapping between the hyperhoneycomb and honeycomb lattices discussed in Section 3 works in the classical limit and makes a correspondence between spin states on the honeycomb lattice and quasi-2D states on the hyperhoneycomb lattice. This correspondence is quantitative, i.e., the spin directions, the energy, and the magnetization of the ground states are the same for both lattices if there is no modulation in the crystallographic $\hat{\mathbf{b}}$ direction of the hyperhoneycomb lattice. However, this quantitative equivalence will not survive in the presence of quantum fluctuations. Since every spin is presented by a spin operator on each lattice site, the projection will map different spin operators to the same position on the honeycomb lattice. Since quantum corrections are generally smaller in three dimensions compared to two dimensions, the ordered states will occupy a larger part of the phase diagram in 3D than in 2D. In this sense, the 3D case is more classical.

In this section, we want to study quantum effects for the Heisenberg-Kitaev model

$$\mathcal{H}_{\text{HK}} = J \sum_{ij} \vec{S}_i \cdot \vec{S}_j + 2K \sum_{\langle ij \rangle_\gamma} S_i^\gamma S_j^\gamma, \quad (5.1)$$

where the couplings can be parametrized as

$$J = A \cos \varphi, \quad K = A \sin \varphi, \quad (5.2)$$

with an energy scale $A > 0$.

5.1 Energy corrections

We want to study the effects of quantum fluctuations to the ground state energy. In the classical limit, the ordered phases of the Heisenberg-Kitaev model for the hyperhoneycomb lattice have a $SU(2)$ degeneracy what is dangerously since the model Hamiltonian has a lower symmetry except for the Heisenberg points. Quantum fluctuations will shift this degeneracy and choose one state out of the $SU(2)$ manifold as the ground state where there may be symmetry equivalent states.

For the honeycomb lattice, the C_3 rotation symmetry is present, which preserves the equivalence of the x , y and z domains of the corresponding phases. However, for the hyperhoneycomb lattice there exist just the C_2 symmetries which connect the x and y domains but not the z domain.

We can write the energy as $E = E_{\text{cl}} + \Delta E$, where $E_{\text{cl}} \sim S^2$ is the classical energy and $\Delta E \sim S$ is the energy correction in linear spin-wave theory, which is an expansion in $1/S$. For clearness, we use the symbols for the FM phase on the hyperhoneycomb lattice from the Appendix A which has $p = 4$ site per unit cell. We make a Holstein-Primakoff transformation and write the Hamiltonian in matrix form as

$$\mathcal{H}_{\text{SW}} = \frac{S}{2} \sum_{\mathbf{q}} \begin{pmatrix} (\vec{\alpha}_{\mathbf{q}}^\dagger)^T & (\vec{\alpha}_{-\mathbf{q}})^T \end{pmatrix} \underbrace{\begin{pmatrix} A(\mathbf{q}) & B(\mathbf{q}) \\ B^\dagger(\mathbf{q}) & A^T(-\mathbf{q}) \end{pmatrix}}_{H_{\text{SW}}(\mathbf{q})} \begin{pmatrix} \vec{\alpha}_{\mathbf{q}} \\ \vec{\alpha}_{-\mathbf{q}}^\dagger \end{pmatrix} - \frac{pNS\varepsilon_0}{2}, \quad (5.3)$$

where $\vec{\alpha}_{\mathbf{q}}$ contains the bosonic creation and annihilation operators and N is the number of unit cells, i.e., the lattice contains pN sites in total. This calculation is described in detail in Appendix A. Since not all bosonic operators are in normal order $a^\dagger a$ due to the matrix form, we get a constant from the commutation relation $[a, a^\dagger] = 1$ which involves the diagonal ε_0 term which is important for the energy calculation. The classical part of the energy is proportional to S^2 and is neglected during the calculation.

We can diagonalize the spin-wave Hamiltonian by a bosonic Bogoliubov transformation [14,29] which transforms

the Hamiltonian (5.3) to

$$\mathcal{H}_{\text{SW}} = \frac{S}{2} \sum_{\mathbf{q}} \left((\vec{\beta}_{\mathbf{q}}^\dagger)^T \quad (\vec{\beta}_{-\mathbf{q}})^T \right) \Sigma \begin{pmatrix} \Omega_{\mathbf{q}}^+ & 0 \\ 0 & \Omega_{\mathbf{q}}^- \end{pmatrix} \begin{pmatrix} \vec{\beta}_{\mathbf{q}} \\ \vec{\beta}_{-\mathbf{q}}^\dagger \end{pmatrix} - \frac{pNS\varepsilon_0}{2}, \quad (5.4)$$

where $\vec{\beta}_{\mathbf{q}}$ contains the bosonic operators in the diagonal basis and $\Omega_{\mathbf{q}}^+$ and $\Omega_{\mathbf{q}}^-$ are diagonal matrices which contain the positive and negative eigenvalues $\{\pm\omega_{\mathbf{q}}^i\}$ of $\Sigma H_{\text{SW}}(\mathbf{q})$ with

$$\Sigma = \begin{pmatrix} \mathbb{1} & 0 \\ 0 & -\mathbb{1} \end{pmatrix}. \quad (5.5)$$

Since we have neglected magnon-magnon interaction in the spin-wave Hamiltonian this is just an approximation. The ground state is the noninteracting-magnon state $|0\rangle$,

$$\beta_{\mathbf{q}}^i |0\rangle = 0, \quad \text{for } i \in \{1, \dots, p\}, \quad (5.6)$$

which is destroyed by the annihilation operators in the diagonal basis. The energy of this state is the expectation value $E = \langle 0 | \mathcal{H}_{\text{SW}} | 0 \rangle$ of the Hamilton operator. Thus only terms of the form $\beta\beta^\dagger$ contribute and the energy correction per lattice site ΔE following from the Hamiltonian (5.4) is

$$\Delta E \cdot pN = -\frac{S}{2} \sum_{\mathbf{q}} \langle 0 | (\vec{\alpha}_{-\mathbf{q}})^T \Omega_{-\mathbf{q}} \vec{\alpha}_{-\mathbf{q}}^\dagger | 0 \rangle - \frac{pNS\varepsilon_0}{2}, = S \sum_{\mathbf{q}} \sum_{i=1}^p \frac{1}{2} \omega_{\mathbf{q}}^i - \frac{pNS\varepsilon_0}{2}, \quad (5.7)$$

with the positive mode frequencies $\omega_{\mathbf{q}}^i$. The first term is equivalent to the zero-point energy of the harmonic oscillator. In the thermodynamic limit, the sum over \mathbf{q} becomes an integral over the first Brillouin zone, $\sum_{\mathbf{q}} \rightarrow N/V_{\text{BZ}} \int d^d q$, where the volume of the first Brillouin zone V_{BZ} is the normalization factor of the integral. Since we find $V_{\text{real}} V_{\text{BZ}} = (2\pi)^d$ with V_{real} be the volume of the real-space unit cell, it is convenient to put the factor $1/(2\pi)^d$ explicitly into the integral. In three dimensions, the volume of the unit cell is found to be $V_{\text{real}} = |\vec{a}_1 \cdot (\vec{a}_2 \times \vec{a}_3)|$ with \vec{a}_1 , \vec{a}_2 and \vec{a}_3 be the lattice vectors. On the other hand, the area of a two-dimensional unit cell is $V_{\text{real}} = \sin \alpha |\vec{a}_1| |\vec{a}_2|$ where α is the angle between the lattice vectors \vec{a}_1 and \vec{a}_2 . The spin-wave energy correction (5.7) is in the thermodynamic limit

$$\Delta E = S \left(\frac{V_{\text{real}}}{p} \int \frac{d^d q}{(2\pi)^d} \sum_{i=1}^p \frac{1}{2} \omega_{\mathbf{q}}^i - \frac{\varepsilon_0}{2} \right). \quad (5.8)$$

The calculation is the same for all ordered commensurate phases, the mode frequencies $\omega_{\mathbf{q}}^i$ and diagonal elements ε_0 in Equation (5.8) have to be replaced by those ones of the corresponding spin-wave matrix.

With help of Equation (5.8), we can calculate the energy correction of the order $1/S$ for all ordered phases of the Heisenberg-Kitaev model. Since all classical phase transitions are first order, the corresponding state may be a local minimum in the global energy landscape even beyond the classical transition point. In this case, we are able to calculate the energy correction for this classically metastable phase and the transition points will be shifted in the presence of quantum fluctuations. However, linear spin-wave theory gets unstable at the classical transition points. Fig. 5.1 (a) shows the magnon spectrum in the Néel phase at the classical transition point to the stripy phase. As one can see, there are flat bands between Γ and \mathbf{Y} and also between Γ and \mathbf{L} . Beyond this parameter point, the eigenvalues get imaginary, i.e., the semiclassical expansion is about an unstable state. On the other hand, the magnon spectrum at the Kitaev point, displayed in Fig. 5.1 (b), has flat band everywhere in the Brillouin zone. This is not surprising since the Kitaev model has a disordered ground state. This breaking down of spin-wave magnons at the classical transition points is also found for all other phases of the considered model.

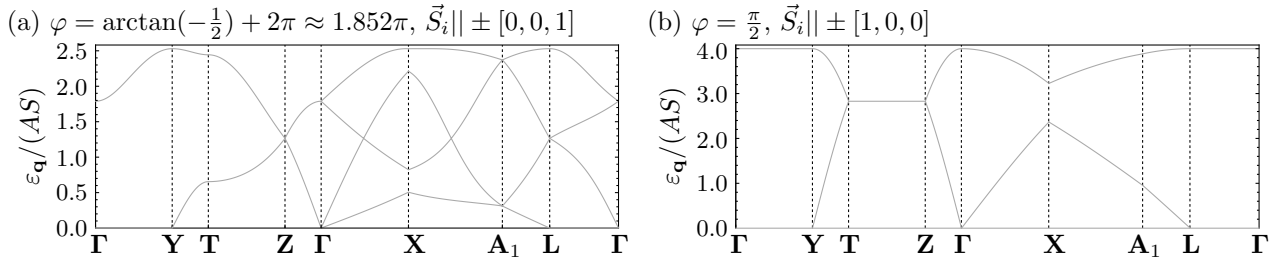


Figure 5.1: Magnon spectra for the Néel phase on the hyperhoneycomb lattice at the classical transition points to the stripy phase (a) and zigzag phase (b). In the case (a), there are flat bands with $\varepsilon_{\mathbf{q}} = 0$ on the paths $\Gamma - \mathbf{Y}$ and $\mathbf{L} - \Gamma$ while for (b) there are flat bands every in the spectrum. Beyond the classical transition points, the eigenenergies get imaginary and thus linear spin-wave theory is not more stable.

Table 5.1: Comparison of quantum corrections to the ground state energy E and the magnetization m in linear spin-wave theory for an AF Heisenberg model on different lattices. Here, d denotes the dimension of the lattice, $J > 0$ is the Heisenberg coupling and S is the length of the spin.

lattice	d	E	m	references
linear chain	1	$-dJS^2(1 + 0.363/S)$	-	[40]
square lattice	2	$-dJS^2(1 + 0.158/S)$	$S - 0.197$	[40]
simple cubic lattice	3	$-dJS^2(1 + 0.097/S)$	$S - 0.078$	[40]
Kitaev ladder	1	$-\frac{3}{2}JS^2(1 + 0.236967/S)$	-	[41]
honeycomb	2	$-\frac{3}{2}JS^2(1 + 0.209842/S)$	$S - 0.258$	[42]
hyperhoneycomb	3	$-\frac{3}{2}JS^2(1 + 0.205283/S)$	$S - 0.187$	-

For the AF Heisenberg model on the 2D honeycomb lattice, we find $E = -\frac{3}{2}JS^2(1 + 0.209842/S)$ with the coupling $J > 0$ what agrees with previous results [42]. For the 3D hyperhoneycomb lattice, the energy is $E = -\frac{3}{2}JS^2(1 + 0.205283/S)$ what is marginal lower compared to the 2D case.

In Table 5.1, we compare the quantum corrections of the AF Heisenberg model for the Kitaev lattices in different dimensions and also for types of square lattices. To study dimensional effects of quantum fluctuations, we consider also the one-dimensional Kitaev ladder which is introduced in section 3.4. In relation to the classical ground state energy, the energy correction of the order S decreases for the square lattice types with increasing dimension d . Since the classical energy of the Néel state depends on the coordination number, which is $z = 2d$, it increases linearly with the dimension. When we rescale the energy correction of order S with the dimension d then the dimensional decrease is much smaller.

On the other hand, the coordination number $z = 3$ is the same for all types of Kitaev lattices. Thus, the classical energy is the same and the energy quantum correction does not strongly depend on the dimension of the system. In particular, the $1/S$ correction in the hyperhoneycomb case is only 2% smaller than the one in the planar honeycomb case.

As mentioned above, for the honeycomb lattice the C_3 symmetry is preserved and the quantum order-by-disorder mechanism chooses the x , y and z domains of the corresponding Heisenberg-Kitaev phases as the ground state [26]. This agrees with our linear spin-wave result using Equation 5.8. On the other hand, for the hyperhoneycomb lattice there is just a C_2 symmetry which connects the x and y domains but not the z domain.

The AF-Heisenberg model posses a $SU(2)$ symmetry, i.e., all possible Néel configuration are degenerate at this point. For $K > 0$, this degeneracy is removed by quantum order-by-disorder. As displayed in Table 5.2, which

shows the energy corrections in units of the classical energy E_{cl} , the x (y) domain of the Néel phase on the hyperhoneycomb lattice is chosen as the ground state in this parameter regime. This choice of domains by the quantum order-by-disorder mechanism agrees with previous results [16]. For comparison, the energy of the $[1, 1, 1]$ domain is also displayed which has typically the highest energy for all considered phases [15]. On the other hand, for $K < 0$, order-by-disorder chooses the z domain as the ground state. Due to the presence of the C_3 symmetry on the honeycomb lattice, order-by-disorder chooses the x , y and z domains here for both, the $K > 0$ and $K < 0$ cases. Although the projective equivalence is not given quantitatively, we can say it is qualitative. The energy difference of domains in 3D and 2D that are classically equivalent concerning the projection, i.e., $\Delta E_{[x,y,z]}^{3\text{D}} - \Delta E_{[x,y,z]}^{2\text{D}}$, is of the order 10^{-3} . On the other hand, the splitting of classically degenerate domains on the same lattice, e.g., $\Delta E_{[0,0,1]}^{3\text{D}} - \Delta E_{[1,1,1]}^{3\text{D}}$, is of the order 10^{-2} . Thus, the effect of different dimensions to the energy in the quantum case is smaller than the effect of quantum order-by-disorder for classically degenerate states in the same dimension. Additionally, the energy difference of the z and x (y) domains on the hyperhoneycomb lattice are of the order $10^{-4} \dots 10^{-5}$ which is at least two orders of magnitudes smaller than the former scale. Compared to the honeycomb model, the degeneracy between the z and x (y) domains is removed but on a small energy scale.

Near the Heisenberg point in the FM regime, quantum corrections are smaller compared to those in the Néel phase. That is because the FM is the exact ground state of the FM Heisenberg model and thus quantum corrections vanish for $\varphi = \pi$. Quantum order-by-disorder chooses the z domain of the FM phase as the ground state for all parameters in this regime, as figured in Table 5.2. Like for the Néel phase, the energy difference obtained by quantum order-by-disorder is larger than the energy difference for equivalent states in 3D and 2D. The energies for the $[1, 1, 1]$ FM differ in 3D and 2D on a scale that is smaller than the shown numerical precision.

The energy correction obtained by linear spin-wave theory for all phases of the Heisenberg-Kitaev model on the hyperhoneycomb lattice is displayed in Fig. 5.2 (a). Because the Néel (FM) and zigzag (stripy) phases are connected by a four-sublattice transformation, the energy corrections will be the same for a corresponding couple of parameters. Thus, we calculate the quantum corrections only for the Néel and FM phases and use the transformation to get the corrections for the zigzag and stripy phases. We have checked this duality explicitly for the z domain of the Néel and zigzag phases. Since the FM is the exact ground state for the FM Heisenberg model, the energy correction vanishes for $\varphi = \pi$ and also at the corresponding Klein point $\varphi = 7\pi/4$. Adding a Kitaev term increases the energy correction. At the classical transition point between the zigzag and FM phases, the energy correction for the zigzag phase is smaller than the correction for the FM phase. This leads to a shift of the transition point in the quantum case in the direction of the FM Heisenberg point. On the other hand, at the transition between stripy and Néel, the Néel phase has a lower energy and thus the transition point is shifted to the FM Kitaev point. This shift of transition points is qualitatively the same as for the honeycomb model [26]. Note, the energy corrections for the AF ($\varphi = \pi/2$) and FM ($\varphi = 3\pi/2$) Kitaev models are the same. Since the real ground state here is a spin liquid, the spin-wave result is not a good approximation.

Although the energies of ordered phases on the 3D hyperhoneycomb and 2D honeycomb lattices quantitatively agree in the classical limit, the exact correspondence is not expectable in the quantum case. Fig. 5.2 (b) shows the energy difference for phases on the hyperhoneycomb and honeycomb lattices obtained by linear spin-wave theory. This dimensional energy difference is about two orders of magnitudes smaller compared to the absolute value of the energy correction. It seems to be at largest in the AF Heisenberg limit and vanishes at the Kitaev points. Surprisingly, this energy difference vanishes also in the Néel phase at the classical transition point to the stripy phase while the stripy energies at this point have a large difference. Similar behavior is shown at the transition between the zigzag and FM phases. This may be an artefact of linear spin-wave theory since the magnon spectra become unstable at the classical transition points.

In the Néel phase, the quantum order-by-disorder mechanism chooses the x (y) domain for $K > 0$ and the z

Table 5.2: Comparison of quantum corrections to the ground state energy in linear spin-wave theory for the Néel and FM phases on the $d = 3$ and $d = 2$ dimensional hyperhoneycomb and honeycomb lattices, respectively. The couplings can be parametrized by an angle φ like in Equation (5.2). For a given range of φ , numeric results are given for a representative value φ_0 . $\Delta E_{[x,y,z]}/E_{\text{cl}}$ gives the $1/S$ energy correction for the Néel and FM phases with spins $\vec{S}_i \parallel \pm[x, y, z]$ and $\vec{S}_i \parallel [x, y, z]$, respectively. Quantum order-by-disorder shifts the classical SU(2) degeneracy. Since $E_{\text{cl}} < 0$, the state with the largest $\Delta E/E_{\text{cl}}$ is the ground state.

Phase	φ	d	$\Delta E_{[0,0,1]}/E_{\text{cl}}$	$\Delta E_{[1,0,0]}/E_{\text{cl}}$	$\Delta E_{[1,1,1]}/E_{\text{cl}}$	ground state
Néel	$(0, \pi/2)$	3	$0.219\,097/S$	$0.219\,166/S$	$0.207\,629/S$	x, y
	$\varphi_0 = 0.2\pi$	2	$0.222\,932/S$	$0.222\,932/S$	$0.211\,625/S$	x, y, z
	$(1.852\pi, 2\pi)$	3	$0.217\,975/S$	$0.217\,847/S$	$0.206\,949/S$	z
	$\varphi_0 = 1.9\pi$	2	$0.221\,463/S$	$0.221\,463/S$	$0.211\,105/S$	x, y, z
FM	$(\pi, 3\pi/2)$	3	$0.028\,155/S$	$0.028\,152/S$	$0.019\,515/S$	z
	$\varphi_0 = 1.2\pi$	2	$0.028\,235/S$	$0.028\,235/S$	$0.019\,515/S$	x, y, z
	$(0.852\pi, \pi)$	3	$0.022\,147/S$	$0.022\,135/S$	$0.013\,928/S$	z
	$\varphi_0 = 0.9\pi$	2	$0.222\,275/S$	$0.022\,275/S$	$0.013\,928/S$	x, y, z

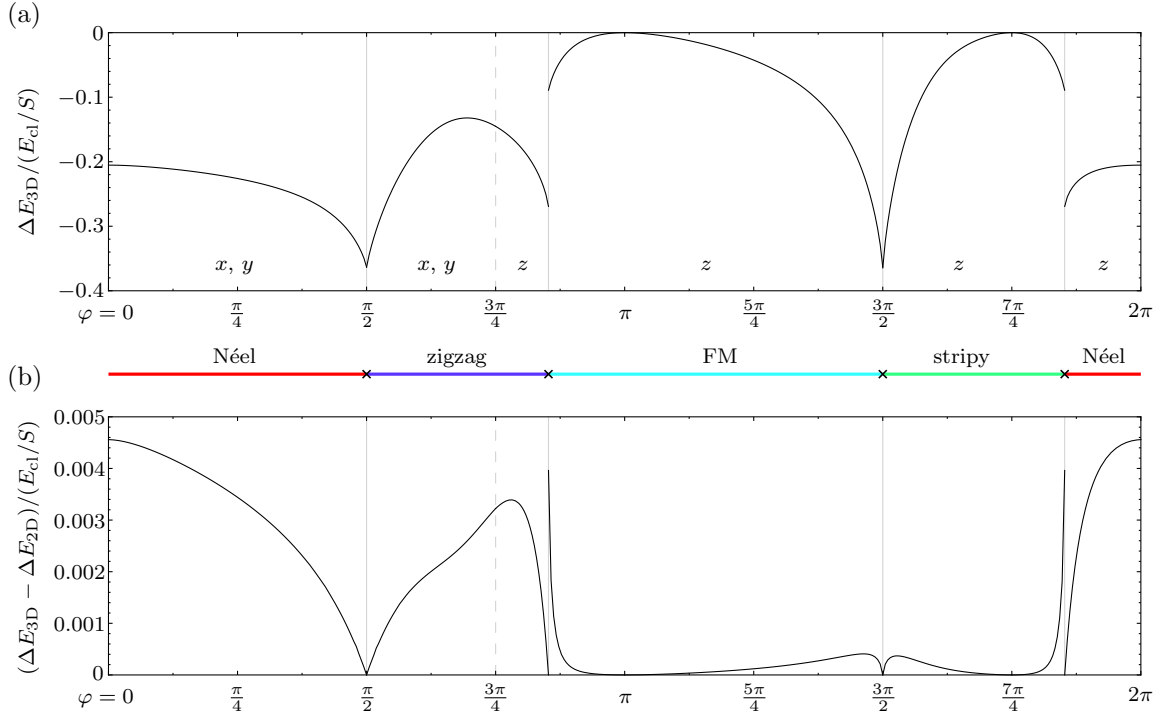


Figure 5.2: (a) Energy corrections obtained by linear spin-wave theory in units of (E_{cl}/S) for ordered phases of the Heisenberg-Kitaev model on the hyperhoneycomb lattice. For each parameter region, the corresponding ground state domain is denoted which is chosen by quantum order-by-disorder. (b) Difference of the energy corrections for the ground states on the 3D hyperhoneycomb and 2D honeycomb lattices.

domain for $K < 0$ as the ground state. Thus, there is a phase transition at $\varphi = 0$ (AF Heisenberg model). This transition is continuous because the magnetization is continuous due to the SU(2) symmetry at the transition point. This quantum critical point is induced by quantum fluctuations. Corrections of higher orders in $1/S$ can not transfer it to a first-order transition since the SU(2) symmetry of the Heisenberg model protects the gapless Goldstone mode. However, higher orders can choose the same ground state domain for $K > 0$ and $K < 0$, respectively. In this case, the former discussion does not apply. A continuous phase transition also occurs at the Klein point $\varphi = 3\pi/4$.

Further, it is possible to calculate the gap of the pseudo-Goldstone mode within linear spin-wave theory [43]. Therefore, one has to calculate the energy landscape as a function of appropriate parameters. The pseudo-Goldstone gap is then a function of the curvature at the minimum energy point.

5.2 Magnetization

Applying quantum fluctuations to our system does not only give an energy correction, it also has influence to the order parameter like the (staggered) magnetization. In linear spin-wave theory, the magnetization is usually decreased. In the following, we want to calculate the correction to the magnetization in the leading order of $1/S$.

Like for the case of calculating the energy correction, see Equations (5.3) to (5.8), we make the calculation explicitly for the FM phase on the $d = 3$ dimensional hyperhoneycomb lattice with $p = 4$ sites per unit cell, but it is in principle the same calculation for any ordered phase. In the FM phase., all spins point in the same direction and the ground state is

$$|0\rangle = \prod_{i \in A} |S\rangle_i \prod_{j \in B} |S\rangle_j \prod_{k \in C} |S\rangle_k \prod_{l \in D} |S\rangle_l, \quad (5.9)$$

where $|S\rangle_i$ denotes the spin on sublattice A, B, C, and D, with maximum component $+S$ in the certain direction. Again, with help of a Holstein-Primakoff transformation, we can express each spin operator \vec{S}_i by bosonic creation and annihilation operators $a_i^{(\dagger)}$, $b_j^{(\dagger)}$, $c_k^{(\dagger)}$, $d_l^{(\dagger)}$ defined on the different sublattices. A detailed description is given in the Appendix A. The magnetization m is the expectation value of the S^3 operator

$$\begin{aligned} m &= \frac{1}{4} (\langle S_i^3 \rangle + \langle S_j^3 \rangle + \langle S_k^3 \rangle + \langle S_l^3 \rangle) \\ &= \frac{1}{4} \left[\langle 0 | (S - a_i^\dagger a_i) | 0 \rangle + \langle 0 | (S - b_j^\dagger b_j) | 0 \rangle + \langle 0 | (S - c_k^\dagger c_k) | 0 \rangle + \langle 0 | (S - d_l^\dagger d_l) | 0 \rangle \right] \\ &= S - \frac{1}{4N} \sum_{\mathbf{q}} \langle 0 | (a_{\mathbf{q}}^\dagger a_{\mathbf{q}} + b_{\mathbf{q}}^\dagger b_{\mathbf{q}} + c_{\mathbf{q}}^\dagger c_{\mathbf{q}} + d_{\mathbf{q}}^\dagger d_{\mathbf{q}}) | 0 \rangle, \end{aligned} \quad (5.10)$$

with the Fourier transformed operators $a_{\mathbf{q}}$, $b_{\mathbf{q}}$, $c_{\mathbf{q}}$ and $d_{\mathbf{q}}$. There is a decrease of the magnetization, if the expectation value of the occupation number $\langle 0 | a_{\mathbf{q}}^\dagger a_{\mathbf{q}} | 0 \rangle$ is non-zero. However, these operators are not creation and annihilation operators of the ground state since the ground state is the noninteracting-magnon state. So we have to express them by new bosonic operators in the diagonal basis. These operators are defined by the bosonic Bogoliubov transformation

$$\begin{pmatrix} \vec{a}_{\mathbf{q}} \\ \vec{a}_{-\mathbf{q}}^\dagger \end{pmatrix} = \begin{pmatrix} U & V \\ V^* & U^* \end{pmatrix} \begin{pmatrix} \vec{\alpha}_{\mathbf{q}} \\ \vec{\alpha}_{-\mathbf{q}}^\dagger \end{pmatrix}, \quad (5.11)$$

where $\vec{a}_{\mathbf{q}} = (a_{\mathbf{q}}, b_{\mathbf{q}}, c_{\mathbf{q}}, d_{\mathbf{q}})^T$ and $\vec{\alpha}_{\mathbf{q}} = (\alpha_{\mathbf{q}}, \beta_{\mathbf{q}}, \gamma_{\mathbf{q}}, \delta_{\mathbf{q}})^T := (\alpha_{1\mathbf{q}}, \alpha_{2\mathbf{q}}, \alpha_{3\mathbf{q}}, \alpha_{4\mathbf{q}})^T$ contains the new bosonic operators. U and V are 4×4 matrices which contain the \mathbf{q} -dependent transformation coefficients. So we can write the expectation value of the occupation number as

$$\langle 0 | a_{\mathbf{q}}^\dagger a_{\mathbf{q}} | 0 \rangle = \langle 0 | \left(\sum_{i=1}^4 v_{1i}^* \alpha_{i,-\mathbf{q}} + \sum_{i=1}^4 u_{1i}^* \alpha_{i\mathbf{q}}^\dagger \right) \left(\sum_{i=1}^4 u_{1i} \alpha_{i\mathbf{q}} + \sum_{i=1}^4 v_{1i} \alpha_{i,-\mathbf{q}}^\dagger \right) | 0 \rangle. \quad (5.12)$$

Here all terms terms vanish which have an annihilation operator on the right, $\alpha_{i\mathbf{q}} | 0 \rangle = 0$, or an creation operator on the left, $\langle 0 | \alpha_{i\mathbf{q}}^\dagger = 0$. Also mixing terms vanish, $\langle 0 | a_{i\mathbf{q}} a_{j\mathbf{q}'}^\dagger | 0 \rangle = 0$ for $i \neq j$ or $\mathbf{q} \neq \mathbf{q}'$. Thus, the expectation value of the occupation number (5.12) reduces to

$$\langle 0 | a_{\mathbf{q}}^\dagger a_{\mathbf{q}} | 0 \rangle = |v_{11}|^2 + |v_{12}|^2 + |v_{13}|^2 + |v_{14}|^2, \quad (5.13)$$

which is the sum of the norm squares of the components in the first line of the matrix V . For the expectation values of $b_{\mathbf{q}}^\dagger b_{\mathbf{q}}$, $c_{\mathbf{q}}^\dagger c_{\mathbf{q}}$, and $d_{\mathbf{q}}^\dagger d_{\mathbf{q}}$, we get the sum over components of the 2nd, 3rd, and 4th line of V , respectively. So the magnetization (5.10) can be written as

$$m = S - \frac{1}{4N} \sum_{\mathbf{q}} \sum_{i,j=1}^4 |v_{ij}|^2. \quad (5.14)$$

In the thermodynamic limit, the sum over \mathbf{q} becomes an integral. Similarly to the transformation between equations (5.7) and (5.8), we get the volume of the real-space unit cell V_{real} as a pre-factor,

$$m = S - \frac{V_{\text{real}}}{4} \int \frac{d\mathbf{q}}{(2\pi)^3} \sum_{i,j=1}^4 |v_{ij}|^2. \quad (5.15)$$

This integral can be solved numerically for given values of the model parameters.

As mentioned above, this calculation of the magnetization can be generalized to other commensurate phases. E.g., the Néel phase has the ground state

$$|0\rangle_{\text{Néel}} = \prod_{i \in A} |S\rangle_i \prod_{j \in B} |-S\rangle_j \prod_{k \in C} |S\rangle_k \prod_{l \in D} |-S\rangle_l, \quad (5.16)$$

i.e., the spin of every second sublattice points in the opposite direction. The staggered magnetization is defined as

$$m_{\text{stagg}} = \frac{1}{4} (\langle S_i^3 \rangle - \langle S_j^3 \rangle + \langle S_k^3 \rangle - \langle S_l^3 \rangle). \quad (5.17)$$

Using a rotated spin basis for every second sublattice, see Appendix A.2, leads to the same integral form (5.15) of the staggered magnetization as for the magnetization in the FM phase.

For a general non-collinear state, there are additional angle corrections in the definition of the staggered magnetization (5.17). For an enlarged magnetic unit cell with p sites, there are p sets of bosonic operators for each sublattice and Equation (5.15) has to be adjusted. The pre-factor $V_{\text{real}}/4$ has to be replaced by V_{real}/p and the sum over i, j goes to p . For an arbitrary d dimensional lattice, the factor $1/(2\pi)^3$ has to be changed to $1/(2\pi)^d$.

5.2.1 Heisenberg-Kitaev phases

The (staggered) magnetization for phases of the Heisenberg-Kitaev model (5.1) on the hyperhoneycomb and honeycomb lattices obtained by linear spin-wave theory is shown in Fig. 5.3. Like for the energy correction, there is no decrease of magnetization for the FM Heisenberg model ($\varphi = \pi$) and the corresponding Klein point ($\varphi = 7\pi/4$). On the other hand, there is a reduced staggered magnetization for the AF Heisenberg model which decreases when a Kitaev coupling is added. The quantum correction to the magnetization is in the 3D system smaller than in the 2D system. This agrees with the usual expectation, that quantum fluctuations get smaller in higher dimensions.

Near the pure Kitaev points, the magnetization gets zero, i.e., the ordered phases get unstable. The values of the critical φ at which the magnetization vanishes give a first estimate for the range of the Kitaev spin liquid. The spin liquid around the AF Kitaev occupies a larger parameter range than the spin liquid at the FM Kitaev point both, in 3D and 2D. This is in contrast to the exact-diagonalization result for the honeycomb model [26], which provides an enlarged spin liquid range in the vicinity of the FM Kitaev point. This may have two reasons. First, we set $S = 1/2$ in the semiclassical calculation, which is the most-quantum case. Thus, higher orders in spin-wave theory are important to get a quantitative better result. Second, spin-wave theory is sensitive only for local instabilities, i.e., for continuous phase transitions. But the transition from an ordered

phase to a spin liquid is in general a first-order transition.

The magnetization diverges also at the transition points zigzag/FM and stripy/Néel. Here, the spin-wave theory becomes unstable and the magnon spectrum has flat bands, see Fig. 5.1 (a). When an eigenvalue $\varepsilon_{\mathbf{q}}^i = 0$, then the corresponding Bogoliubov coefficients diverge. If the gap is closed only at the pseudo-Goldstone mode, then the integrand in Equation (5.15) has a pole of order one and the integral converges in $d \geq 2$. When the bands are flat, there is a manifold of singularities and the integral may diverge.

These complications show that spin-wave theory is a controlled semi-classical expansion for ordered phase. However, it fails near a transition point and it can not reflect the nature of quantum disordered states like spin liquids.

The 3D-2D equivalence for the hyperhoneycomb and honeycomb models does not hold for the quantum corrections to the magnetization. However, the 2D and 3D magnetization curves have qualitatively the same form and break down at approximatively the same critical parameters.

5.2.2 High-field phase

Since we have discussed the classical Heisenberg-Kitaev model in an external field in section 2, we want to study also quantum corrections for this model, in particular, for the high-field phase. Therefore we consider the model Hamiltonian

$$\mathcal{H}_{\text{HK}} = J \sum_{ij} \vec{S}_i \cdot \vec{S}_j + 2K \sum_{\langle ij \rangle_\gamma} S_i^\gamma S_j^\gamma - \vec{h} \cdot \sum_i \vec{S}_i, \quad (5.18)$$

with the magnetic field \vec{h} . However, Equation (5.15) delivers the magnetization in field direction $\vec{m} \cdot \hat{h}$, with \hat{h} be the unit vector in field direction. For a general phase in a magnetic field, the magnetization is not necessarily in the field direction since this is a frustrated problem. For the considered model, the magnetization in the high-field phase is parallel to the field direction.

In the high-field limit, there is no correction to the magnetization since the polarized state is an eigenstate of the Zeeman term. By reducing the field strength, the magnetization decreases. Near a continuous transition, the magnetization is strongly reduced, as displayed in Fig. 5.4 (a). For $\varphi = 0.62\pi$ and $S = 1/2$, the magnetization is reduced to $m_{3\text{D}} = 0.30$ and $m_{2\text{D}} = 0.21$, respectively, at the transition point for the hyperhoneycomb and honeycomb lattices. That means, the magnetization for the three-dimensional lattice is about 50% larger. On the other hand, if there is a first-order phase transition, then the magnetization is much larger at the transition point, as illustrated in Fig. 5.4 (b). The magnetization is $m_{3\text{D}} = 0.40$ and $m_{2\text{D}} = 0.39$ at the transition to canted zigzag for $\varphi = 0.75\pi$, i.e., the difference is much smaller compared to the former case.

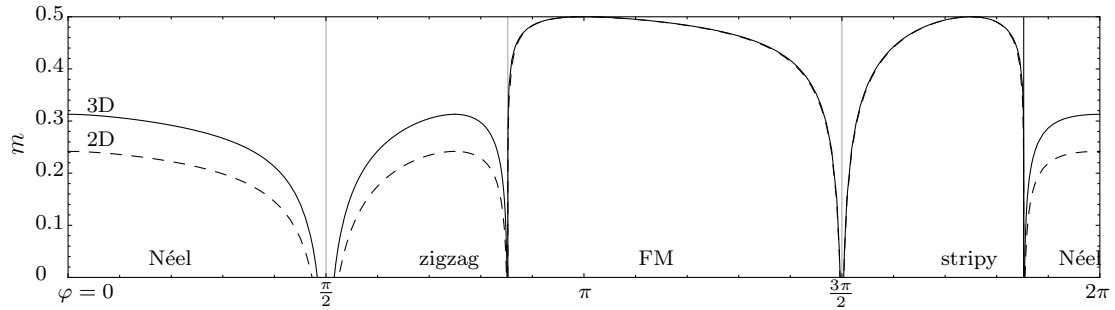


Figure 5.3: The (staggered) magnetization m for the ordered phases of the Heisenberg-Kitaev model on the 3D hyperhoneycomb and 2D honeycomb lattices obtained by linear spin-wave theory for $S = 1/2$.

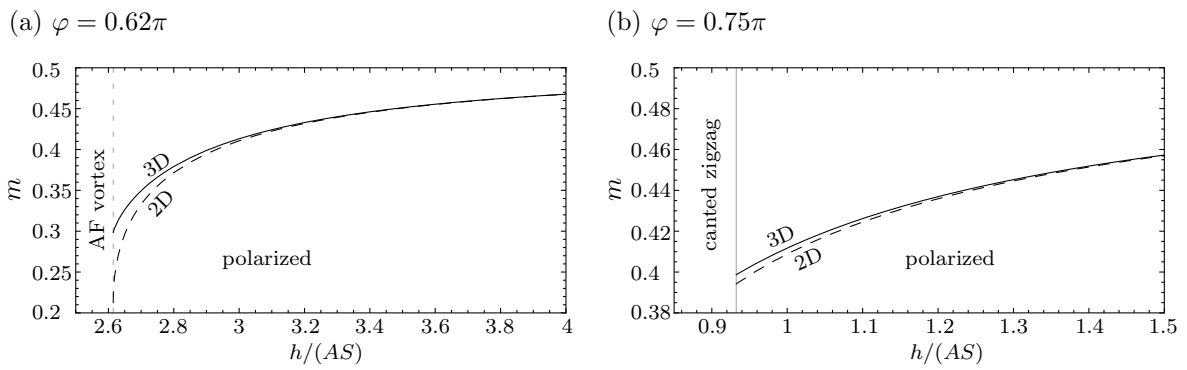


Figure 5.4: Magnetization calculated in linear spin-wave theory for $S = 1/2$ in the high-field polarized phase of the Heisenberg-Kitaev model on the hyperhoneycomb and honeycomb lattices in a $[1, 1, 1]$ magnetic field. The magnetization curves show different qualitative behavior when there is a continuous phase transition ($\varphi = 0.62\pi$) (a) or a first-order phase transition ($\varphi = 0.75\pi$) (b).

Appendix

A Spin-wave theory

A.1 High-field/polarized phase

In this section, we show the calculation for the spin-wave theory in detail. We use the terms defined in section 2.4, where there are explained the Holstein-Primakoff transformation, the rotated spin basis, and the Fourier transformed bosonic operators. With the nearest neighbor vector $\delta_\gamma = \vec{R}_j - \vec{R}_i$, which connects the lattice site i and j , and the number of unit cells N , we find some calculation rules for the quadratic terms in the bosonic operators ξ_i and ξ_i^\dagger

$$\begin{aligned}
\sum_i \xi_i^\dagger \xi_i &= \sum_{\mathbf{q}\mathbf{q}'} \frac{1}{N} \underbrace{\sum_i e^{-i(\mathbf{q}-\mathbf{q}')\mathbf{R}_i}}_{\delta_{\mathbf{q},\mathbf{q}'}} \xi_{\mathbf{q}}^\dagger \xi_{\mathbf{q}} = \sum_{\mathbf{q}} \xi_{\mathbf{q}}^\dagger \xi_{\mathbf{q}}, \\
\sum_{\langle ij \rangle_\gamma} \xi_i^\dagger \tilde{\xi}_j &= \frac{1}{N} \sum_{\mathbf{q}\mathbf{q}'} \sum_{\langle ij \rangle_\gamma} e^{-i\mathbf{q}\mathbf{R}_i} e^{i\mathbf{q}'\mathbf{R}_j} \xi_{\mathbf{q}}^\dagger \tilde{\xi}_{\mathbf{q}'} = \sum_{\mathbf{q}\mathbf{q}'} \frac{1}{N} \underbrace{\sum_i e^{-i(\mathbf{q}-\mathbf{q}')\mathbf{R}_i}}_{\delta_{\mathbf{q},\mathbf{q}'}} e^{i\mathbf{q}'\delta_\gamma} \xi_{\mathbf{q}}^\dagger \tilde{\xi}_{\mathbf{q}'} = \sum_{\mathbf{q}} e^{i\mathbf{q}\delta_\gamma} \xi_{\mathbf{q}}^\dagger \tilde{\xi}_{\mathbf{q}}, \\
\sum_{\langle ij \rangle_\gamma} \xi_i \tilde{\xi}_j^\dagger &= \sum_{\mathbf{q}} e^{-i\mathbf{q}\delta_\gamma} \xi_{\mathbf{q}} \tilde{\xi}_{\mathbf{q}}^\dagger, \\
\sum_{\langle ij \rangle_\gamma} \xi_i \tilde{\xi}_j &= \frac{1}{N} \sum_{\mathbf{q}\mathbf{q}'} \sum_{\langle ij \rangle_\gamma} e^{i\mathbf{q}\mathbf{R}_i} e^{i\mathbf{q}'\mathbf{R}_j} \xi_{\mathbf{q}} \tilde{\xi}_{\mathbf{q}'} = \sum_{\mathbf{q}\mathbf{q}'} \frac{1}{N} \underbrace{\sum_i e^{i(\mathbf{q}+\mathbf{q}')\mathbf{R}_i}}_{\delta_{-\mathbf{q},\mathbf{q}'}} e^{i\mathbf{q}'\delta_\gamma} \xi_{\mathbf{q}} \tilde{\xi}_{\mathbf{q}'} = \sum_{\mathbf{q}} e^{-i\mathbf{q}\delta_\gamma} \xi_{\mathbf{q}} \tilde{\xi}_{-\mathbf{q}}, \\
\sum_{\langle ij \rangle_\gamma} \xi_i^\dagger \tilde{\xi}_j^\dagger &= \sum_{\mathbf{q}} e^{i\mathbf{q}\delta_\gamma} \xi_{\mathbf{q}}^\dagger \tilde{\xi}_{-\mathbf{q}}^\dagger.
\end{aligned} \tag{A.1}$$

Now the Heisenberg term can be expressed in terms of the Fourier transformed creation and annihilation operators,

$$\begin{aligned}
\mathcal{H}_H &= J \sum_{\langle ij \rangle} \vec{S}_i \cdot \vec{S}_j = J \sum_{\langle ij \rangle} \left[\frac{1}{2} (S_i^+ S_j^- + S_i^- S_j^+) + S_i^3 S_j^3 \right] \\
&= JS \sum_{\langle ij \rangle} \left(\xi_i^\dagger \xi_j + \xi_i \xi_j^\dagger - \xi_i^\dagger \xi_i - \xi_j^\dagger \xi_j \right) + \text{const.} + \mathcal{O}(\sqrt{S}) \\
&= JS \sum_{i \in \text{unit cell}} \left[-3 \left(a_i^\dagger a_i + b_i^\dagger b_i + c_i^\dagger c_i + d_i^\dagger d_i \right) + \left(a_i^\dagger b_{i,z} + a_i^\dagger d_{i,x} + a_i^\dagger d_{i,y} + c_i^\dagger d_{i,z} + c_i^\dagger b_{i,x} + c_i^\dagger b_{i,y} \right) \right. \\
&\quad \left. + \left(a_i b_{i,z}^\dagger + a_i d_{i,x}^\dagger + a_i d_{i,y}^\dagger + c_i d_{i,z}^\dagger + c_i b_{i,x}^\dagger + c_i b_{i,y}^\dagger \right) \right] \\
&= JS \sum_{\mathbf{q}} \left[-3 \left(a_{\mathbf{q}}^\dagger a_{\mathbf{q}} + b_{\mathbf{q}}^\dagger b_{\mathbf{q}} + c_{\mathbf{q}}^\dagger c_{\mathbf{q}} + d_{\mathbf{q}}^\dagger d_{\mathbf{q}} \right) \right. \\
&\quad \left. + \left(e^{-i\mathbf{q}\delta_3} a_{\mathbf{q}}^\dagger b_{\mathbf{q}} + e^{-i\mathbf{q}\delta_4} a_{\mathbf{q}}^\dagger d_{\mathbf{q}} + e^{-i\mathbf{q}\delta_5} a_{\mathbf{q}}^\dagger d_{\mathbf{q}} + e^{-i\mathbf{q}\delta_3} c_{\mathbf{q}}^\dagger d_{\mathbf{q}} + e^{-i\mathbf{q}\delta_1} c_{\mathbf{q}}^\dagger b_{\mathbf{q}} + e^{-i\mathbf{q}\delta_2} c_{\mathbf{q}}^\dagger b_{\mathbf{q}} \right) \right. \\
&\quad \left. + \left(e^{i\mathbf{q}\delta_3} a_{\mathbf{q}} b_{\mathbf{q}}^\dagger + e^{i\mathbf{q}\delta_4} a_{\mathbf{q}} d_{\mathbf{q}}^\dagger + e^{i\mathbf{q}\delta_5} a_{\mathbf{q}} d_{\mathbf{q}}^\dagger + e^{i\mathbf{q}\delta_3} c_{\mathbf{q}} d_{\mathbf{q}}^\dagger + e^{i\mathbf{q}\delta_1} c_{\mathbf{q}} b_{\mathbf{q}}^\dagger + e^{i\mathbf{q}\delta_2} c_{\mathbf{q}} b_{\mathbf{q}}^\dagger \right) \right].
\end{aligned} \tag{A.2}$$

Also the Zeeman term can be written in this form

$$\begin{aligned}\mathcal{H}_Z &= -\vec{h} \cdot \sum_i \vec{S}_i = h \sum_i \left(a_i^\dagger a_i + b_i^\dagger b_i + c_i^\dagger c_i + d_i^\dagger d_i \right) + \text{const.} \\ &= h \sum_{\mathbf{q}} \left(a_{\mathbf{q}}^\dagger a_{\mathbf{q}} + b_{\mathbf{q}}^\dagger b_{\mathbf{q}} + c_{\mathbf{q}}^\dagger c_{\mathbf{q}} + d_{\mathbf{q}}^\dagger d_{\mathbf{q}} \right).\end{aligned}\tag{A.3}$$

The expression of the Kitaev term

$$\mathcal{H}_K = 2K \sum_{\gamma} S_i^\gamma S_j^\gamma \tag{A.4}$$

in terms of bosonic operators is more complicated. While the Heisenberg term is $SU(2)$ invariant, it has the same form independently of the chosen basis. However, the Kitaev interaction includes terms, which are explicitly in the $\vec{e}_1, \vec{e}_2, \vec{e}_3$ basis. On the other hand, we use a basis depending on the field direction. With help of Equation (2.13), we can express the $\vec{e}_1, \vec{e}_2, \vec{e}_3$ basis vectors by the $\vec{e}_x, \vec{e}_y, \vec{e}_z$ basis vectors as

$$\begin{pmatrix} \vec{e}_1 \\ \vec{e}_2 \\ \vec{e}_3 \end{pmatrix} = \begin{pmatrix} \cos \theta \cos \phi & \cos \theta \sin \phi & -\sin \theta \\ -\sin \phi & \cos \phi & 0 \\ \sin \theta \cos \phi & \sin \theta \sin \phi & \cos \theta \end{pmatrix} \begin{pmatrix} \vec{e}_x \\ \vec{e}_y \\ \vec{e}_z \end{pmatrix}.\tag{A.5}$$

We can express the spin vector \vec{S}_i by θ and ϕ , which are the spherical coordinates of the magnetic field,

$$\begin{aligned}\vec{S}_i &= \sqrt{\frac{S}{2}} (\xi_i + \xi_i^\dagger) \vec{e}_1 - i \sqrt{\frac{S}{2}} (\xi_i - \xi_i^\dagger) \vec{e}_2 + (S - \xi_i^\dagger \xi_i) \vec{e}_3 \\ &= \left(\cos \theta \cos \phi \sqrt{\frac{S}{2}} (\xi_i + \xi_i^\dagger) + i \sin \phi \sqrt{\frac{S}{2}} (\xi_i - \xi_i^\dagger) + \sin \theta \cos \phi (S - \xi_i^\dagger \xi_i) \right) \vec{e}_x \\ &\quad + \left(\cos \theta \sin \phi \sqrt{\frac{S}{2}} (\xi_i + \xi_i^\dagger) - i \cos \phi \sqrt{\frac{S}{2}} (\xi_i - \xi_i^\dagger) + \sin \theta \sin \phi (S - \xi_i^\dagger \xi_i) \right) \vec{e}_y \\ &\quad + \left(-\sin \theta \sqrt{\frac{S}{2}} (\xi_i + \xi_i^\dagger) + \cos \theta (S - \xi_i^\dagger \xi_i) \right) \vec{e}_z.\end{aligned}\tag{A.6}$$

Thus, the parts of the Kitaev term (A.4) are

$$\begin{aligned}S_i^x S_j^x &= \cos^2 \theta \cos^2 \phi \frac{S}{2} (\xi_i + \xi_i^\dagger)(\xi_j + \xi_j^\dagger) && + i \cos \theta \cos \phi \sin \phi \frac{S}{2} (\xi_i + \xi_i^\dagger)(\xi_j - \xi_j^\dagger) \\ &\quad + \cos \theta \sin \theta \cos^2 \phi \sqrt{\frac{S}{2}} (\xi_i + \xi_i^\dagger)(S - \xi_j^\dagger \xi_j) \\ &\quad + i \cos \theta \cos \phi \sin \phi \frac{S}{2} (\xi_i - \xi_i^\dagger)(\xi_j + \xi_j^\dagger) && - \sin^2 \phi \frac{S}{2} (\xi_i - \xi_i^\dagger)(\xi_j - \xi_j^\dagger) \\ &\quad + i \sin \theta \cos \phi \sin \phi \sqrt{\frac{S}{2}} (\xi_i - \xi_i^\dagger)(S - \xi_j^\dagger \xi_j) \\ &\quad + \cos \theta \sin \theta \cos^2 \phi \sqrt{\frac{S}{2}} (S - \xi_i^\dagger \xi_i)(\xi_j + \xi_j^\dagger) && + i \sin \theta \cos \phi \sin \phi \sqrt{\frac{S}{2}} (S - \xi_i^\dagger \xi_i)(\xi_j - \xi_j^\dagger) \\ &\quad + \sin^2 \theta \cos^2 \phi (S - \xi_i^\dagger \xi_i)(S - \xi_j^\dagger \xi_j),\end{aligned}\tag{A.7}$$

$$\begin{aligned}
S_i^y S_j^y &= \cos^2 \theta \sin^2 \phi \frac{S}{2} (\xi_i + \xi_i^\dagger)(\xi_j + \xi_j^\dagger) & -i \cos \theta \cos \phi \sin \phi \frac{S}{2} (\xi_i + \xi_i^\dagger)(\xi_j - \xi_j^\dagger) \\
&+ \cos \theta \sin \theta \sin^2 \phi \sqrt{\frac{S}{2}} (\xi_i + \xi_i^\dagger)(S - \xi_j^\dagger \xi_j) \\
&-i \cos \theta \cos \phi \sin \phi \frac{S}{2} (\xi_i - \xi_i^\dagger)(\xi_j + \xi_j^\dagger) & -\cos^2 \phi \frac{S}{2} (\xi_i - \xi_i^\dagger)(\xi_j - \xi_j^\dagger) \\
&-i \sin \theta \cos \phi \sin \phi \sqrt{\frac{S}{2}} (\xi_i - \xi_i^\dagger)(S - \xi_j^\dagger \xi_j) \\
&+ \cos \theta \sin \theta \sin^2 \phi \sqrt{\frac{S}{2}} (S - \xi_i^\dagger \xi_i)(\xi_j + \xi_j^\dagger) & -i \sin \theta \cos \phi \sin \phi \sqrt{\frac{S}{2}} (S - \xi_i^\dagger \xi_i)(\xi_j - \xi_j^\dagger) \\
&+ \sin^2 \theta \sin^2 \phi (S - \xi_i^\dagger \xi_i)(S - \xi_j^\dagger \xi_j),
\end{aligned} \tag{A.8}$$

and

$$\begin{aligned}
S_i^z S_j^z &= \sin^2 \theta \frac{S}{2} (\xi_i + \xi_i^\dagger)(\xi_j + \xi_j^\dagger) & -\cos \theta \sin \theta \sqrt{\frac{S}{2}} (\xi_i + \xi_i^\dagger)(S - \xi_j^\dagger \xi_j) \\
&-\cos \theta \sin \theta \sqrt{\frac{S}{2}} (S - \xi_i^\dagger \xi_i)(\xi_j + \xi_j^\dagger) & +\cos^2 \theta (S - \xi_i^\dagger \xi_i)(S - \xi_j^\dagger \xi_j).
\end{aligned} \tag{A.9}$$

Terms of the order S^2 are constant so they can be neglected when computing h_{c0} and the instability wavevector. Terms of the order $S^{3/2}$ are

$$\begin{aligned}
S_i^x S_j^x &= \cos \theta \sin \theta \cos^2 \phi \sqrt{\frac{S}{2}} S (\xi_i + \xi_i^\dagger) + i \cos \theta \cos \phi \sin \phi \sqrt{\frac{S}{2}} S (\xi_i - \xi_i^\dagger) \\
&\cos \theta \sin \theta \cos^2 \phi \sqrt{\frac{S}{2}} S (\xi_j + \xi_j^\dagger) + i \cos \theta \cos \phi \sin \phi \sqrt{\frac{S}{2}} S (\xi_j - \xi_j^\dagger), \\
S_i^y S_j^y &= \cos \theta \sin \theta \sin^2 \phi \sqrt{\frac{S}{2}} S (\xi_i + \xi_i^\dagger) - i \cos \theta \cos \phi \sin \phi \sqrt{\frac{S}{2}} S (\xi_i - \xi_i^\dagger) \\
&\cos \theta \sin \theta \sin^2 \phi \sqrt{\frac{S}{2}} S (\xi_j + \xi_j^\dagger) - i \cos \theta \cos \phi \sin \phi \sqrt{\frac{S}{2}} S (\xi_j - \xi_j^\dagger), \\
S_i^z S_j^z &= -\cos \theta \sin \theta \sqrt{\frac{S}{2}} S (\xi_i + \xi_i^\dagger) - \cos \theta \sin \theta \sqrt{\frac{S}{2}} S (\xi_j + \xi_j^\dagger).
\end{aligned} \tag{A.10}$$

In this order, the operators ξ_i and ξ_j are decoupled and the sum over i, j vanishes. Terms of the order S are

$$\begin{aligned}
S_i^x S_j^x &= \frac{S}{2} \left[r_x^2 \xi_i \xi_j + (r_x^*)^2 \xi_i^\dagger \xi_j^\dagger + \xi_i^\dagger \xi_j + \xi_i \xi_j^\dagger \right] - S \sin^2 \theta \cos^2 \phi (\xi_i^\dagger \xi_i + \xi_j^\dagger \xi_j), \\
S_i^y S_j^y &= \frac{S}{2} \left[r_y^2 \xi_i \xi_j + (r_y^*)^2 \xi_i^\dagger \xi_j^\dagger + \xi_i^\dagger \xi_j + \xi_i \xi_j^\dagger \right] - S \sin^2 \theta \sin^2 \phi (\xi_i^\dagger \xi_i + \xi_j^\dagger \xi_j), \\
S_i^z S_j^z &= \frac{S}{2} \left[r_z^2 \xi_i \xi_j + (r_z^*)^2 \xi_i^\dagger \xi_j^\dagger + \xi_i^\dagger \xi_j + \xi_i \xi_j^\dagger \right] - S \cos^2 \theta (\xi_i^\dagger \xi_i + \xi_j^\dagger \xi_j),
\end{aligned} \tag{A.11}$$

with

$$r_x = \cos \theta \cos \phi + i \sin \phi, \quad r_y = \cos \theta \sin \phi - i \cos \phi, \quad r_z = \sin \theta. \tag{A.12}$$

Terms of higher order in $1/S$ are neglected. Now we can write the Kitaev term (A.4) as following

$$\begin{aligned}
\mathcal{H}_K &= -2SK \sum_i \left(a_i^\dagger a_i + b_i^\dagger b_i + c_i^\dagger c_i + d_i^\dagger d_i \right) + KS \left[|r_x|^2 \sum_x \left(a_i^\dagger d_j + a_i d_j^\dagger + c_i^\dagger b_j + c_i b_j^\dagger \right) \right. \\
&\quad \left. + |r_y|^2 \sum_y \left(a_i^\dagger d_j + a_i d_j^\dagger + c_i^\dagger b_j + c_i b_j^\dagger \right) + |r_z|^2 \sum_z \left(a_i^\dagger b_j + a_i b_j^\dagger + c_i^\dagger d_j + c_i d_j^\dagger \right) \right] \\
&\quad + KS \left[r_x^2 \sum_x (a_i d_j + c_i b_j) + r_y^2 \sum_y (a_i d_j + c_i b_j) + r_z^2 \sum_z (a_i b_j + c_i d_j) \right] \\
&\quad + KS \left[(r_x^*)^2 \sum_x (a_i^\dagger d_j^\dagger + c_i^\dagger b_j^\dagger) + (r_y^*)^2 \sum_y (a_i^\dagger d_j^\dagger + c_i^\dagger b_j^\dagger) + (r_z^*)^2 \sum_z (a_i^\dagger b_j^\dagger + c_i^\dagger d_j^\dagger) \right] \\
&= -2SK \sum_{\mathbf{q}} \left(a_{\mathbf{q}}^\dagger a_{\mathbf{q}} + b_{\mathbf{q}}^\dagger b_{\mathbf{q}} + c_{\mathbf{q}}^\dagger c_{\mathbf{q}} + d_{\mathbf{q}}^\dagger d_{\mathbf{q}} \right) \\
&\quad + KS \sum_{\mathbf{q}} \left[|r_x|^2 \left(e^{-i\mathbf{q}\delta_4} a_{\mathbf{q}}^\dagger d_{\mathbf{q}} + e^{i\mathbf{q}\delta_4} a_{\mathbf{q}} d_{\mathbf{q}}^\dagger + e^{-i\mathbf{q}\delta_1} c_{\mathbf{q}}^\dagger b_{\mathbf{q}} + e^{i\mathbf{q}\delta_1} c_{\mathbf{q}} b_{\mathbf{q}}^\dagger \right) \right. \\
&\quad \left. + |r_y|^2 \left(e^{-i\mathbf{q}\delta_4} a_{\mathbf{q}}^\dagger d_{\mathbf{q}} + e^{i\mathbf{q}\delta_4} a_{\mathbf{q}} d_{\mathbf{q}}^\dagger + e^{-i\mathbf{q}\delta_1} c_{\mathbf{q}}^\dagger b_{\mathbf{q}} + e^{i\mathbf{q}\delta_1} c_{\mathbf{q}} b_{\mathbf{q}}^\dagger \right) \right. \\
&\quad \left. + |r_z|^2 \left(e^{-i\mathbf{q}\delta_3} a_{\mathbf{q}}^\dagger b_{\mathbf{q}} + e^{i\mathbf{q}\delta_3} a_{\mathbf{q}} b_{\mathbf{q}}^\dagger + e^{-i\mathbf{q}\delta_3} c_{\mathbf{q}}^\dagger d_{\mathbf{q}} + e^{i\mathbf{q}\delta_3} c_{\mathbf{q}} d_{\mathbf{q}}^\dagger \right) \right] \\
&\quad + KS \sum_{\mathbf{q}} \left[\left(r_x^2 e^{-i\mathbf{q}\delta_4} a_{-\mathbf{q}} d_{\mathbf{q}} + (r_x^*)^2 e^{-i\mathbf{q}\delta_4} a_{\mathbf{q}}^\dagger d_{-\mathbf{q}}^\dagger + r_x^2 e^{-i\mathbf{q}\delta_1} c_{-\mathbf{q}} b_{\mathbf{q}} + (r_x^*)^2 e^{-i\mathbf{q}\delta_1} c_{\mathbf{q}}^\dagger b_{-\mathbf{q}}^\dagger \right) \right. \\
&\quad \left. + \left(r_y^2 e^{-i\mathbf{q}\delta_5} a_{-\mathbf{q}} d_{\mathbf{q}} + (r_y^*)^2 e^{-i\mathbf{q}\delta_5} a_{\mathbf{q}}^\dagger d_{-\mathbf{q}}^\dagger + r_y^2 e^{-i\mathbf{q}\delta_2} c_{-\mathbf{q}} b_{\mathbf{q}} + (r_y^*)^2 e^{-i\mathbf{q}\delta_2} c_{\mathbf{q}}^\dagger b_{-\mathbf{q}}^\dagger \right) \right. \\
&\quad \left. + \left(r_z^2 e^{-i\mathbf{q}\delta_3} a_{-\mathbf{q}} b_{\mathbf{q}} + (r_z^*)^2 e^{-i\mathbf{q}\delta_3} a_{\mathbf{q}}^\dagger b_{-\mathbf{q}}^\dagger + r_z^2 e^{-i\mathbf{q}\delta_3} c_{-\mathbf{q}} d_{\mathbf{q}} + (r_z^*)^2 e^{-i\mathbf{q}\delta_3} c_{\mathbf{q}}^\dagger d_{-\mathbf{q}}^\dagger \right) \right]. \tag{A.13}
\end{aligned}$$

The total Hamiltonian can be written in the compact matrix notation

$$\mathcal{H}_{\text{SW}} = \mathcal{H}_J + \mathcal{H}_K + \mathcal{H}_Z = \frac{1}{2} \sum_{\mathbf{q}} \left((\vec{\alpha}_{\mathbf{q}}^\dagger)^T \quad (\vec{\alpha}_{-\mathbf{q}})^T \right) \underbrace{\begin{pmatrix} A(\mathbf{q}) & B(\mathbf{q}) \\ B^\dagger(\mathbf{q}) & A^T(-\mathbf{q}) \end{pmatrix}}_{H_{\text{SW}}(\mathbf{q})} \begin{pmatrix} \vec{\alpha}_{\mathbf{q}} \\ \vec{\alpha}_{-\mathbf{q}}^\dagger \end{pmatrix}, \tag{A.14}$$

where the vector $\vec{\alpha}_{\mathbf{q}}^{(\dagger)} = (a^{(\dagger)}, b^{(\dagger)}, c^{(\dagger)}, d^{(\dagger)})^T$ includes the bosonic operators and the spin-wave matrix $H_{\text{SW}}(\mathbf{q})$ contains the blocks

$$A(\mathbf{q}) = \begin{pmatrix} \varepsilon_0 & \lambda_{03}(-\mathbf{q}) & 0 & \lambda_{04}(-\mathbf{q}) + \lambda_{05}(-\mathbf{q}) \\ \lambda_{03}(\mathbf{q}) & \varepsilon_0 & \lambda_{01}(\mathbf{q}) + \lambda_{02}(\mathbf{q}) & 0 \\ 0 & \lambda_{01}(-\mathbf{q}) + \lambda_{02}(-\mathbf{q}) & \varepsilon_0 & \lambda_{03}(-\mathbf{q}) \\ \lambda_{04}(\mathbf{q}) + \lambda_{05}(\mathbf{q}) & 0 & \lambda_{03}(\mathbf{q}) & \varepsilon_0 \end{pmatrix}, \tag{A.15}$$

$$B(\mathbf{q}) = \begin{pmatrix} 0 & \lambda_{13}^*(\mathbf{q}) & 0 & \lambda_{14}^*(\mathbf{q}) + \lambda_{15}^*(\mathbf{q}) \\ \lambda_{13}^*(-\mathbf{q}) & 0 & \lambda_{11}^*(-\mathbf{q}) + \lambda_{12}^*(-\mathbf{q}) & 0 \\ 0 & \lambda_{11}^*(\mathbf{q}) + \lambda_{12}^*(\mathbf{q}) & 0 & \lambda_{13}^*(\mathbf{q}) \\ \lambda_{14}^*(-\mathbf{q}) + \lambda_{15}^*(-\mathbf{q}) & 0 & \lambda_{13}^*(-\mathbf{q}) & 0 \end{pmatrix}, \tag{A.16}$$

which are defined by the following relations

$$\varepsilon_0 = \frac{\hbar}{S} - 3J - 2K, \tag{A.17}$$

$$\lambda_{0\alpha} = \begin{cases} (J + K|r_x|^2)e^{i\mathbf{q}\delta_\alpha} & , \alpha = 1, 4 \\ (J + K|r_y|^2)e^{i\mathbf{q}\delta_\alpha} & , \alpha = 2, 5 \\ (J + K|r_z|^2)e^{i\mathbf{q}\delta_\alpha} & , \alpha = 3 \end{cases}, \quad \lambda_{1\alpha} = \begin{cases} Kr_x^2 e^{i\mathbf{q}\delta_\alpha} & , \alpha = 1, 4 \\ Kr_y^2 e^{i\mathbf{q}\delta_\alpha} & , \alpha = 2, 5 \\ Kr_z^2 e^{i\mathbf{q}\delta_\alpha} & , \alpha = 3. \end{cases} \tag{A.18}$$

For $h = 0$, the spin-wave Hamiltonian defined by Equation (A.14) agrees with the Hamiltonian for the FM phase since both phases are adiabatically connected.

A.2 Néel phase

The spin-wave theory in the Néel phase differs from the one in the FM phase. Here, neighboring spins are antiparallel. For alignment of spins parallel to the z direction, i.e., spins on sublattices A and C have z component $+S$ while spins on sublattices B and D have z components $-z$, the Holstein-Primakoff transformation can be defined as

$$S_i^- = \sqrt{2S}a_i^\dagger \sqrt{1 - \frac{a_i^\dagger a_i}{2S}}, \quad S_i^+ = \sqrt{2S} \sqrt{1 - \frac{a_i^\dagger a_i}{2S}} a_i, \quad S_i^z = S - a_i^\dagger a_i \quad (\text{analogously for } c) \quad (\text{A.19})$$

and

$$S_j^- = \sqrt{2S} \sqrt{1 - \frac{b_j^\dagger b_j}{2S}} b_j, \quad S_j^+ = \sqrt{2S} b_j^\dagger \sqrt{1 - \frac{b_j^\dagger b_j}{2S}}, \quad S_j^z = -S + b_j^\dagger b_j \quad (\text{analogously for } d), \quad (\text{A.20})$$

which leads in the large S limit to

$$S_i^- = \sqrt{2S}a_i^\dagger, \quad S_i^+ = \sqrt{2S}a_i, \quad S_i^z = S - a_i^\dagger a_i \quad (\text{A.21})$$

and

$$S_j^- = \sqrt{2S}b_j, \quad S_j^+ = \sqrt{2S}b_j^\dagger, \quad S_j^z = S - b_j^\dagger b_j. \quad (\text{A.22})$$

Again, using the rotated spin basis (A.5), we can calculate the spin-wave Hamiltonian for any spin direction in the Néel phase. The convention is to define the Fourier transformed operators with a different sign in the exponential function. This leads to

$$a_i = \frac{1}{\sqrt{N}} \sum_i e^{i\mathbf{q}\mathbf{R}_i} a_{\mathbf{q}}, \quad b_j = \frac{1}{\sqrt{N}} \sum_j e^{-i\mathbf{q}\mathbf{R}_j} b_{\mathbf{q}}, \quad c_k = \frac{1}{\sqrt{N}} \sum_k e^{i\mathbf{q}\mathbf{R}_k} c_{\mathbf{q}}, \quad d_l = \frac{1}{\sqrt{N}} \sum_l e^{-i\mathbf{q}\mathbf{R}_l} d_{\mathbf{q}}. \quad (\text{A.23})$$

The calculation of Hamiltonian in Fourier space is quiet analogous to the previous calculation in the high-field and FM phases. Thus the spin-wave Hamiltonian for the Néel phase an be written as

$$\mathcal{H}_{\text{SW}}^{\text{Néel}} = \frac{1}{2} \sum_{\mathbf{q}} \left(\begin{pmatrix} \vec{\beta}_{\mathbf{q}}^\dagger & \vec{\beta}_{-\mathbf{q}} \end{pmatrix}^T \underbrace{\begin{pmatrix} A^{\text{Néel}}(\mathbf{q}) & B^{\text{Néel}}(\mathbf{q}) \\ (B^{\text{Néel}})^\dagger(\mathbf{q}) & (A^{\text{Néel}})^T(-\mathbf{q}) \end{pmatrix}}_{H_{\text{SW}}^{\text{Néel}}(\mathbf{q})} \begin{pmatrix} \vec{\beta}_{\mathbf{q}} \\ \vec{\beta}_{-\mathbf{q}}^\dagger \end{pmatrix} \right), \quad (\text{A.24})$$

with

$$\vec{\beta}_{\mathbf{q}} = \begin{pmatrix} a_{\mathbf{q}} \\ b_{-\mathbf{q}} \\ c_{\mathbf{q}} \\ d_{-\mathbf{q}} \end{pmatrix}, \quad (\text{A.25})$$

$$A^{\text{Néel}}(\mathbf{q}) = \begin{pmatrix} \epsilon_0^{\text{Néel}} & \lambda_{13}^*(\mathbf{q}) & 0 & \lambda_{14}^*(\mathbf{q}) + \lambda_{15}^*(\mathbf{q}) \\ \lambda_{13}(\mathbf{q}) & \epsilon_0^{\text{Néel}} & \lambda_{11}(\mathbf{q}) + \lambda_{12}(\mathbf{q}) & 0 \\ 0 & \lambda_{11}^*(\mathbf{q}) + \lambda_{12}^*(\mathbf{q}) & \epsilon_0^{\text{Néel}} & \lambda_{13}^*(\mathbf{q}) \\ \lambda_{14}(\mathbf{q}) + \lambda_{15}(\mathbf{q}) & 0 & \lambda_{13}(\mathbf{q}) & \epsilon_0^{\text{Néel}} \end{pmatrix}, \quad (\text{A.26})$$

$$B^{\text{Néel}}(\mathbf{q}) = \begin{pmatrix} 0 & \lambda_{03}(-\mathbf{q}) & 0 & \lambda_{04}(-\mathbf{q}) + \lambda_{05}(-\mathbf{q}) \\ \lambda_{03}(\mathbf{q}) & 0 & \lambda_{01}(\mathbf{q}) + \lambda_{02}(\mathbf{q}) & 0 \\ 0 & \lambda_{01}(-\mathbf{q}) + \lambda_{02}(-\mathbf{q}) & 0 & \lambda_{03}(-\mathbf{q}) \\ \lambda_{04}(\mathbf{q}) + \lambda_{05}(\mathbf{q}) & 0 & \lambda_{03}(\mathbf{q}) & 0 \end{pmatrix}, \quad (\text{A.27})$$

and

$$\epsilon_0^{\text{Néel}} = 3J + 2K. \quad (\text{A.28})$$

The spin-wave Hamiltonians for the x , y , z stripy and zigzag phases can be built by combining the FM and Néel spin-wave Hamiltonians. For a FM bond, we use the corresponding element of the FM spin matrix, while for a AF bond, we use the element of the Néel spin matrix. For the generalized stripy and zigzag phases, which are not colinear, there must be considered also angle corrections.

B Analytical parametrization of the magnetic unit cell

To obtain the phase diagram for the Heisenberg-Kitaev model on the hyperhoneycomb lattice in an external field, see Sections 2.5.1 and 2.5.2, we make a combination of analytical parametrization of spins and numerical minimization for different geometries of the magnetic unit cells.

The interaction between pairs of nearest-neighbor spins \vec{S}_i and \vec{S}_j can be written in compact form

$$H_{\langle ij \rangle} = \vec{S}_i^T \mathcal{H}_{\langle ij \rangle \gamma} \vec{S}_j, \quad (\text{B.1})$$

with $\gamma = x, y, z$, \vec{S}_i and \vec{S}_j are the spin vectors given in the $(\vec{e}_x, \vec{e}_y, \vec{e}_z)$ basis and

$$\mathcal{H}_{\langle ij \rangle x} = \begin{pmatrix} J+K & 0 & 0 \\ 0 & J & 0 \\ 0 & 0 & J \end{pmatrix}, \quad \mathcal{H}_{\langle ij \rangle y} = \begin{pmatrix} J & 0 & 0 \\ 0 & J+K & 0 \\ 0 & 0 & J \end{pmatrix}, \quad \mathcal{H}_{\langle ij \rangle z} = \begin{pmatrix} J & 0 & 0 \\ 0 & J & 0 \\ 0 & 0 & J+K \end{pmatrix} \quad (\text{B.2})$$

are the bond-dependent interaction matrices.

The model contains a magnetic field $\vec{h} = h(\vec{e}_x \sin \theta \cos \phi + \vec{e}_y \sin \theta \sin \phi + \vec{e}_z \cos \theta)$. So it is convenient to introduce a coordinate system aligned according to the magnetic field direction,

$$\begin{pmatrix} \vec{e}_1 \\ \vec{e}_2 \\ \vec{e}_3 \end{pmatrix} = \begin{pmatrix} \cos \theta \cos \phi & \cos \theta \sin \phi & -\sin \phi \\ -\sin \phi & \cos \phi & 0 \\ \sin \theta \cos \phi & \sin \theta \sin \phi & \cos \theta \end{pmatrix} \begin{pmatrix} \vec{e}_x \\ \vec{e}_y \\ \vec{e}_z \end{pmatrix} = R \begin{pmatrix} \vec{e}_x \\ \vec{e}_y \\ \vec{e}_z \end{pmatrix}, \quad (\text{B.3})$$

where \vec{e}_3 is aligned in the field direction.

The spin \vec{S}_i on the lattice site i can be parametrized by two angles θ_i and ϕ_i as

$$\vec{S}'_i = S(\vec{e}_1 \sin \theta_i \cos \phi_i + \vec{e}_2 \sin \theta_i \sin \phi_i + \vec{e}_3 \cos \theta_i), \quad (\text{B.4})$$

where S is the length of the spin and the prime denotes the expression in the $(\vec{e}_1, \vec{e}_2, \vec{e}_3)$ basis.

In the $(\vec{e}_1, \vec{e}_2, \vec{e}_3)$ basis, the interaction term (B.1) transforms to

$$H_{\langle ij \rangle} = \vec{S}'_i{}^T \mathcal{H}'_{\langle ij \rangle \gamma} \vec{S}'_j, \quad (\text{B.5})$$

with $\vec{S}'_i = R\vec{S}_i$ and $\mathcal{H}'_{\langle ij \rangle \gamma} = R\mathcal{H}_{\langle ij \rangle \gamma}R^T$. This form seems to be unnecessarily complicated compared to (B.1). Though, θ_i describes the canting angle of the spin \vec{S}'_i to the magnetic field direction, what makes the interpretation of the spin direction in the rotated basis easier.

A commensurate magnetic structure can have one or several ordering wave-vectors corresponding to single- \mathbf{Q} and multi- \mathbf{Q} states, respectively. For a single- \mathbf{Q} state with the ordering wave-vector \mathbf{Q} and a crystallographic lattice vector \mathbf{R} , the condition

$$e^{i\mathbf{Q}\cdot\mathbf{R}} = 1 \quad (\text{B.6})$$

is sufficient, that \mathbf{R} is also a lattice vector of the magnetic lattice. For a multi- \mathbf{Q} state, \mathbf{R} has to satisfy the condition (B.6) for all ordering wave-vectors.

The simplest magnetic structure occurs for $\mathbf{Q} = \Gamma$. Here, the magnetic unit cell corresponds to the crystallographic unit cell with four sites and has thus the geometry displayed in Fig. 2.1. Spins on sublattice A are connected with spins on sublattice D over x and y bonds and also with spins on sublattice B over z bonds. On the other hand, spins on sublattice C are connected with spins on sublattice B over x and y bonds while

C and D are connected by z bonds. Thus, we can write the energy of a $\mathbf{Q} = \mathbf{\Gamma}$ state as

$$\begin{aligned}
E = & \vec{S}'_a{}^T \mathcal{H}'_{\langle ij \rangle_x} \vec{S}'_d + \vec{S}'_a{}^T \mathcal{H}'_{\langle ij \rangle_y} \vec{S}'_d + \vec{S}'_a{}^T \mathcal{H}'_{\langle ij \rangle_z} \vec{S}'_b \\
& + \vec{S}'_c{}^T \mathcal{H}'_{\langle ij \rangle_x} \vec{S}'_b + \vec{S}'_c{}^T \mathcal{H}'_{\langle ij \rangle_y} \vec{S}'_b + \vec{S}'_c{}^T \mathcal{H}'_{\langle ij \rangle_z} \vec{S}'_d \\
& - h(\cos \theta_a + \cos \theta_b + \cos \theta_c + \cos \theta_d).
\end{aligned} \tag{B.7}$$

The last line involves the Zeeman term $-\vec{h} \cdot \vec{S}'_i$, which reduces to $-hS'_3$ since the field lies in the \vec{e}_3 direction. The spins \vec{S}'_i can be expressed with Equation (B.4) by two parameters θ_i and ϕ_i . Thus, the energy is a function of 8 parameters, which can be minimized numerically.

We also include geometries with larger unit cells. On the hyperhoneycomb lattice, we find 7 different geometries with an 8-site unit cell, which correspond to the ordering wave-vectors $\mathbf{Y} = (0, -\frac{1}{2}, 0)$, $\mathbf{Z} = (0, 0, -\frac{1}{2})$, $\mathbf{T} \sim (-\frac{1}{2}, 0, 0)$, $\mathbf{L} = (-\frac{1}{4}, -\frac{1}{4}, -\frac{1}{4})$, $(-\frac{1}{4}, -\frac{1}{4}, \frac{1}{4})$, $(-\frac{1}{4}, \frac{1}{4}, -\frac{1}{4})$, and $(\frac{1}{4}, -\frac{1}{4}, -\frac{1}{4})$. Further, there are 13 different geometries with a 12-site unit cell. The corresponding wave-vectors are $(\frac{1}{3}, 0, 0)$, $(0, \frac{1}{3}, 0)$, $(0, 0, \frac{1}{3})$, $(\frac{1}{3}, \frac{1}{3}, 0)$, $(\frac{1}{3}, 0, \frac{1}{3})$, $(0, \frac{1}{3}, \frac{1}{3})$, $(\frac{1}{6}, \frac{1}{6}, \frac{1}{6})$, $(\frac{1}{6}, \frac{1}{6}, -\frac{1}{6})$, $(\frac{1}{6}, -\frac{1}{6}, \frac{1}{6})$, $(-\frac{1}{6}, \frac{1}{6}, \frac{1}{6})$, $(\frac{1}{6}, -\frac{1}{6}, -\frac{1}{2})$, $(-\frac{1}{6}, -\frac{1}{2}, \frac{1}{6})$, and $(-\frac{1}{2}, \frac{1}{6}, -\frac{1}{6})$. For the magnetic unit cells with 8 and 12 spins, the energy term (B.7) is a function of 16 and 24 parameters, respectively.

C Luttinger-Tisza Approach

The Luttinger-Tisza approach is a method to find the classical ground state of quadratic spin Hamiltonians, that was introduced by Luttinger and Tisza [35] for Bravais lattices and later extended by Lyons and Kaplan [36] for models with inequivalent spins. However, there may be cases for that the method does not work.

We consider a lattice with a primitive unit cell that includes p spins of equal length. Let \mathbf{R}_n be a lattice vector and ρ_ν the position inside the unit cell, then $\mathbf{S}_{n\nu}$ is the spin on lattice site $\mathbf{R}_{n\nu} = \mathbf{R}_n + \rho_\nu$. The energy of a given spin configuration can be written as

$$E = \frac{1}{2} \sum_{\substack{n\nu, m\mu \\ \alpha\beta}} S_{n\nu}^\alpha J_{n\nu, m\mu}^{\alpha\beta} S_{m\mu}^\beta = \mathbf{S}^\dagger \mathbf{J} \mathbf{S}, \quad (\text{C.1})$$

where $S_{n\nu}^\alpha$ denotes the α component of the spin $\mathbf{S}_{n\nu}$ and $J_{n\nu, m\mu}^{\alpha\beta}$ is a matrix element that contains the interaction term between $S_{n\nu}^\alpha$ and $S_{m\mu}^\beta$. The last term is a compact matrix notation, where \mathbf{S} is a vector that includes all components of all pN spins on the lattice. Thus, it is a $3pN$ -component vector while \mathbf{J} is the $3pN \times 3pN$ interaction matrix. The identity $\mathbf{S}^T = \mathbf{S}^\dagger$ is true since \mathbf{S} is a real vector. Note that this quadratic form does not capture, for instance, a Zeeman term. Due to the lattice translation symmetry, the interaction depends only on the relative position of the spins, i.e.,

$$J_{n\nu, m\mu}^{\alpha\beta} = J_{\nu\mu}^{\alpha\beta}(\mathbf{R}_m - \mathbf{R}_n). \quad (\text{C.2})$$

All spins have the same length, i.e., they fulfill the strong spin constraint

$$\mathbf{S}_{n\nu} \cdot \mathbf{S}_{n\nu} = \sum_{\alpha} S_{n\nu}^\alpha S_{n\nu}^\alpha = 1 \quad \forall n, \nu. \quad (\text{C.3})$$

This strong spin constraint can be replaced by the weak spin constraint

$$\sum_{n\nu} \mathbf{S}_{n\nu} \cdot \mathbf{S}_{n\nu} = \sum_{\substack{n\nu \\ \alpha}} S_{n\nu}^\alpha S_{n\nu}^\alpha = \mathbf{S}^\dagger \mathbf{S} = pN, \quad (\text{C.4})$$

i.e., the average length square of the spins is 1. The advantage of this constraint is that \mathbf{S} satisfies the weak constraint (C.4) still after a unitary transformation, what is generally not the case for the strong constraint (C.3). We use the translation symmetry of the lattice and define the Fourier transformation

$$Q_{\mathbf{k}\nu}^\alpha = \frac{1}{\sqrt{N}} \sum_n e^{-i\mathbf{k}\mathbf{R}_{n\nu}} S_{n\nu}^\alpha \quad \iff \quad \mathbf{Q} = \mathcal{F} \mathbf{S}, \quad (\text{C.5})$$

where the first equation defines the Fourier transformation of each component and the second equation is in matrix form with the $3pN \times 3pN$ Fourier transformation matrix \mathcal{F} . The vector \mathbf{Q} is the Fourier transformation of \mathbf{S} . Since the Fourier transformation is a unitary transformation, the inverse Fourier transformation is defined as $\mathcal{F}^{-1} = \mathcal{F}^\dagger$. Now we can write the energy (C.1) in terms of \mathbf{Q} as

$$E = \frac{1}{2} \sum_{\substack{\nu\mu, \mathbf{k}\mathbf{k}' \\ \alpha\beta}} Q_{\nu\mathbf{k}}^\alpha L_{\nu\mu, \mathbf{k}\mathbf{k}'}^{\alpha\beta} Q_{\mu\mathbf{k}'}^\beta = \mathbf{Q}^\dagger L \mathbf{Q}, \quad (\text{C.6})$$

with the matrix $L = \mathcal{F} \mathcal{J} \mathcal{F}^\dagger$. Using the completeness relation of the Fourier transformation, the corresponding matrix elements of L are

$$L_{\mu\nu, \mathbf{k}\mathbf{k}'}^{\alpha\beta} = \sum_{\mathbf{R}_m - \mathbf{R}_n} e^{i\mathbf{k}(\mathbf{R}_{m\mu} - \mathbf{R}_{n\nu})} J_{\nu\mu}^{\alpha\beta}(\mathbf{R}_m - \mathbf{R}_n) \delta_{\mathbf{k}, \mathbf{k}'}. \quad (\text{C.7})$$

The matrix L is thus blockdiagonal with respect to \mathbf{k} and \mathbf{k}' . That reduces the diagonalization problem of a $3pN \times 3pN$ matrix to the diagonalization of N different $3p \times 3p$ matrices. We will write $L_{\mu\nu}^{\alpha\beta}(\mathbf{k}) = L_{\mu\nu, \mathbf{k}\mathbf{k}}^{\alpha\beta}$ to denote this $3p \times 3p$ matrix in the following, to avoid confusion with the indices. We write the energy term (C.6) in diagonal form

$$E = \mathbf{Q}'^\dagger D \mathbf{Q}', \quad (\text{C.8})$$

with $\mathbf{Q}' = U\mathbf{Q}$ and $D = ULU^\dagger$, where U is a unitary matrix. Since L is blockdiagonal, U is also blockdiagonal and $U(\mathbf{k}) = (U_{\mu\nu}^{\alpha\beta})_{\mathbf{k}\mathbf{k}}$ diagonalizes the corresponding matrix $L(\mathbf{k})$. Note that $\mathbf{Q}' = U\mathcal{F}S$ satisfies $\mathbf{Q}'^\dagger \mathbf{Q}' = pN$, which is equivalent to the weak spin constraint (C.4). Since the norm of \mathbf{Q}' is fixed, the minimization of the energy term (C.6) is simple. If the minimal eigenvalue of D is $\lambda_{\min} = D_{\nu\nu, \mathbf{k}\mathbf{k}}^{\alpha\alpha}$ for $\nu = \nu_{\min}$, $\mathbf{k} = \mathbf{k}_{\min}$, and $\alpha = \alpha_{\min}$, then the choice of the corresponding $Q'_{\nu\mathbf{k}}^\alpha$ as the only non-zero element of \mathbf{Q}' will minimize the energy. Due to symmetry reasons, there is also a minimum eigenvalue for $\mathbf{k} = -\mathbf{k}_{\min}$. Thus, a convenient choice of \mathbf{Q}' is

$$Q'_{\nu\mathbf{k}}^\alpha = \begin{cases} \sqrt{\frac{pN}{2}} e^{\pm i\varphi}, & \mathbf{k} = \pm \mathbf{k}_{\min}, \nu = \nu_{\min}, \alpha = \alpha_{\min}, \\ 0, & \text{otherwise.} \end{cases} \quad (\text{C.9})$$

There is a phase as a free parameter and the \pm choice in the phase factor verifies that \mathbf{S} is real. The real space spin configuration can be derived by the transformation $\mathbf{S} = \mathcal{F}^\dagger U^\dagger \mathbf{Q}'$. Let Ψ and Ψ^* be the corresponding normalized eigenvectors of $U^\dagger(\mathbf{k}_{\min})$ and $U^\dagger(-\mathbf{k}_{\min})$ for the eigenvalue λ_{\min} , respectively. The vector \mathbf{Q} then becomes

$$Q_{\nu\mathbf{k}}^\alpha = \begin{cases} \sqrt{\frac{pN}{2}} e^{i\varphi} \Psi_{\nu\mathbf{k}}^\alpha, & \mathbf{k} = \mathbf{k}_{\min}, \\ \sqrt{\frac{pN}{2}} e^{-i\varphi} \Psi_{\nu\mathbf{k}}^{*\alpha}, & \mathbf{k} = -\mathbf{k}_{\min}, \\ 0, & \text{otherwise,} \end{cases} \quad (\text{C.10})$$

and the spin state arises with the help of Equation (C.5) to

$$S_{n\nu}^\alpha = \sqrt{\frac{p}{2}} \left[\Psi_\nu^\alpha e^{i(\mathbf{k}_{\min} \mathbf{R}_{n\nu} + \varphi)} + \Psi_\nu^{*\alpha} e^{-i(\mathbf{k}_{\min} \mathbf{R}_{n\nu} + \varphi)} \right]. \quad (\text{C.11})$$

This state fullfills the weak spin constraint (C.4) and has to be checked for the strong spin constraint (C.3). If this is also satisfied, then the exact ground state has been found. However, if the strong spin constraint is not fullfilled, the Luttinger-Tisza approach has been failed. Since all configurations, which satisfy the strong constraint, also satisfy the weak constraint, the eigenvalue $\lambda_{\min} = E/(pN)$ is a strict lower bound to the real ground-state energy.

Some models may have a degenerate ground-state manifold, i.e., the Heisenberg model posses a $SU(2)$ symmetry. First, there can be several wave-vectors which simultaneously minimize the energy, in particular, for symmetry-connected wave-vectors. Second, the eigenvalue λ_{\min} of the matrix $L(\mathbf{k}_{\min})$ can belong to a higher-dimensional subspace, where the dimension of the subspace belongs to the degeneracy of the ground-state manifold.

For the problem in Section 4, the Heisenberg-Kitaev- Γ model is of the form

$$\mathcal{H}_{\text{HK}\Gamma} = \sum_{\langle ij \rangle_\gamma} \left[J \vec{S}_i \cdot \vec{S}_j + K S_i^\gamma S_j^\gamma \pm \Gamma \left(S_i^\alpha S_j^\beta + S_i^\beta S_j^\alpha \right) \right], \quad (\text{C.12})$$

with the sign structure for the hyperhoneycomb lattice described in Fig. 3.7 (a), and for the projected lattice

in Fig. 3.8 (a). For the hyperhoneycomb lattice, we have $p = 4$, so the corresponding $L(\mathbf{k})$ is a 12×12 matrix. With the help of Equation (C.7), we can write $L(\mathbf{k})$ as

$$L(\mathbf{k}) = \begin{pmatrix} J + K_1 & \Gamma_3 & \Gamma_2 \\ \Gamma_3 & J + K_2 & \Gamma_1 \\ \Gamma_2 & \Gamma_1 & J + K_3 \end{pmatrix}, \quad (\text{C.13})$$

where J , K_1 , K_2 , K_3 , Γ_1 , Γ_2 , and Γ_3 are 4×4 matrices. J contains all Heisenberg interaction terms. The blocks K_1 , K_2 , and K_3 include all interaction terms of the Kitaev type $S^x S^x$, $S^y S^y$, and $S^z S^z$, while Γ_1 , Γ_2 , and Γ_3 contain the $S^y S^z$, $S^z S^x$, and $S^x S^y$ Γ interactions, respectively. These matrices are defined as following

$$J = \begin{pmatrix} 0 & J_z & 0 & J_x^I + J_y^I \\ J_z^* & 0 & J_x^{*II} + J_y^{*II} & 0 \\ 0 & J_x^{II} + J_y^{II} & 0 & 0 \\ J_x^{*I} + J_y^{*I} & 0 & J_z^* & 0 \end{pmatrix}, \quad (\text{C.14})$$

$$K_1 = \begin{pmatrix} 0 & 0 & 0 & K_x^I \\ 0 & 0 & K_x^{*II} & 0 \\ 0 & K_x^{II} & 0 & 0 \\ K_x^{*I} & 0 & 0 & 0 \end{pmatrix}, K_2 = \begin{pmatrix} 0 & 0 & 0 & K_y^I \\ 0 & 0 & K_y^{*II} & 0 \\ 0 & K_y^{II} & 0 & 0 \\ K_y^{*I} & 0 & 0 & 0 \end{pmatrix}, K_3 = \begin{pmatrix} 0 & K_z & 0 & 0 \\ K_z^* & 0 & 0 & 0 \\ 0 & 0 & 0 & K_z \\ 0 & 0 & K_z^* & 0 \end{pmatrix}, \quad (\text{C.15})$$

and

$$\Gamma_1 = \begin{pmatrix} 0 & 0 & 0 & -\Gamma_x^I \\ 0 & 0 & \Gamma_x^{*II} & 0 \\ 0 & \Gamma_x^{II} & 0 & 0 \\ -\Gamma_x^{*I} & 0 & 0 & 0 \end{pmatrix}, \Gamma_2 = \begin{pmatrix} 0 & 0 & 0 & \Gamma_y^I \\ 0 & 0 & -\Gamma_y^{*II} & 0 \\ 0 & -\Gamma_y^{II} & 0 & 0 \\ \Gamma_y^{*I} & 0 & 0 & 0 \end{pmatrix}, \quad (\text{C.16})$$

$$\Gamma_3 = \begin{pmatrix} 0 & \Gamma_z & 0 & 0 \\ \Gamma_z^* & 0 & 0 & 0 \\ 0 & 0 & 0 & \Gamma_z \\ 0 & 0 & \Gamma_z^* & 0 \end{pmatrix}.$$

The matrix entries are

$$\begin{aligned} J_x^{II} &= J e^{-i\mathbf{k}\delta_1}, & K_x^{II} &= K e^{-i\mathbf{k}\delta_1}, & \Gamma_x^{II} &= \Gamma e^{-i\mathbf{k}\delta_1}, \\ J_y^{II} &= J e^{-i\mathbf{k}\delta_2}, & K_y^{II} &= K e^{-i\mathbf{k}\delta_2}, & \Gamma_y^{II} &= \Gamma e^{-i\mathbf{k}\delta_2}, \\ J_z &= J e^{-i\mathbf{k}\delta_3}, & K_z &= K e^{-i\mathbf{k}\delta_3}, & \Gamma_z &= \Gamma e^{-i\mathbf{k}\delta_3}, \\ J_x^I &= J e^{-i\mathbf{k}\delta_4}, & K_x^I &= K e^{-i\mathbf{k}\delta_4}, & \Gamma_x^I &= \Gamma e^{-i\mathbf{k}\delta_4}, \\ J_y^I &= J e^{-i\mathbf{k}\delta_5}, & K_y^I &= K e^{-i\mathbf{k}\delta_5}, & \Gamma_y^I &= \Gamma e^{-i\mathbf{k}\delta_5}, \end{aligned} \quad (\text{C.17})$$

for the hyperhoneycomb model. For the projected model, we replace the original nearest-neighbor vectors on the hyperhoneycomb lattice by the nearest-neighbor vectors on the honeycomb lattice, i.e., $\delta_1, \delta_4 \rightarrow \delta_x$, $\delta_2, \delta_5 \rightarrow \delta_y$ and $\delta_3 \rightarrow \delta_z$.

We have to find the minimum eigenvalue of $L(\mathbf{k})$ for all wave-vectors \mathbf{k} inside the Brillouin zone. This can be done numerically. The corresponding spin state can be reproduced with Equation (C.11) and has to be checked for the strong spin constraint (C.3).

D Single-Q ansatz

The single- \mathbf{Q} ansatz is a method, which may find a spiral ground state. It is used to find the phases of the model in Section 4.2. We can write the spin $\vec{S}_a(\mathbf{r})$ at the lattice site \mathbf{r} on the sublattice a as

$$\vec{S}_a(\mathbf{r}) = \sin \eta_a [\hat{\mathbf{e}}_a^x \cos(\mathbf{Q} \cdot \mathbf{r}) + \hat{\mathbf{e}}_a^y \sin(\mathbf{Q} \cdot \mathbf{r})] + \cos \eta_a \hat{\mathbf{e}}_a^z, \quad (\text{D.1})$$

with the ordering wave-vector \mathbf{Q} . Here, η_a is a canting angle and $\{\hat{\mathbf{e}}_a^x, \hat{\mathbf{e}}_a^y, \hat{\mathbf{e}}_a^z\}$ is an arbitrary coordinate system. These parameters are defined independently on the four sublattices of the hyperhoneycomb lattice. For a non-vanishing $\sin \eta_a \neq 0$, the first term describes a spin component rotating around the $\hat{\mathbf{e}}_a^z$ axis, while $\cos \eta_a \neq 0$ is the finite sublattice magnetization. The coordinate system $\{\hat{\mathbf{e}}_a^x, \hat{\mathbf{e}}_a^y, \hat{\mathbf{e}}_a^z\}$ can be parametrized by three Euler angles. In total, this leads to 16 free minimization parameters and additionally d free components of the wave-vector \mathbf{Q} for a d dimensional lattice.

Since the $\{\hat{\mathbf{e}}_a^x, \hat{\mathbf{e}}_a^y, \hat{\mathbf{e}}_a^z\}$ basis does not generally agree with the $[\hat{\mathbf{x}}, \hat{\mathbf{y}}, \hat{\mathbf{z}}]$ basis of the Kitaev and Γ interactions, we have to couple the $\hat{\alpha} \cdot \vec{S}_a(\mathbf{r})$ components to calculate the energy of the corresponding spin state. In the following, \mathbf{r} denotes a lattice vector, \mathbf{m}, \mathbf{n} are the relative positions inside a unit cell and $\hat{\alpha}, \hat{\beta} \in \{\hat{\mathbf{x}}, \hat{\mathbf{y}}, \hat{\mathbf{z}}\}$ are the unit vectors in the $[\hat{\mathbf{x}}, \hat{\mathbf{y}}, \hat{\mathbf{z}}]$ basis. Thus, a typically $S_a^\alpha S_b^\beta$ interaction term decouples with the help of the ansatz (D.1) to

$$\begin{aligned} S_a^\alpha S_b^\beta &= \left\{ \hat{\alpha} \cdot \vec{S}_a(\mathbf{r} + \mathbf{m}) \right\} \left\{ \hat{\beta} \cdot \vec{S}_b(\mathbf{r} + \mathbf{n}) \right\} = \\ &(\hat{\alpha} \cdot \hat{\mathbf{e}}_a^x)(\hat{\beta} \cdot \hat{\mathbf{e}}_b^x) \sin \eta_a \sin \eta_b \cos[\mathbf{Q}(\mathbf{r} + \mathbf{m})] \cos[\mathbf{Q}(\mathbf{r} + \mathbf{n})] \\ &+ (\hat{\alpha} \cdot \hat{\mathbf{e}}_a^x)(\hat{\beta} \cdot \hat{\mathbf{e}}_b^y) \sin \eta_a \sin \eta_b \cos[\mathbf{Q}(\mathbf{r} + \mathbf{m})] \sin[\mathbf{Q}(\mathbf{r} + \mathbf{n})] \\ &+ (\hat{\alpha} \cdot \hat{\mathbf{e}}_a^x)(\hat{\beta} \cdot \hat{\mathbf{e}}_b^z) \sin \eta_a \cos \eta_b \cos[\mathbf{Q}(\mathbf{r} + \mathbf{m})] \\ &+ (\hat{\alpha} \cdot \hat{\mathbf{e}}_a^y)(\hat{\beta} \cdot \hat{\mathbf{e}}_b^x) \sin \eta_a \sin \eta_b \sin[\mathbf{Q}(\mathbf{r} + \mathbf{m})] \cos[\mathbf{Q}(\mathbf{r} + \mathbf{n})] \\ &+ (\hat{\alpha} \cdot \hat{\mathbf{e}}_a^y)(\hat{\beta} \cdot \hat{\mathbf{e}}_b^y) \sin \eta_a \sin \eta_b \sin[\mathbf{Q}(\mathbf{r} + \mathbf{m})] \sin[\mathbf{Q}(\mathbf{r} + \mathbf{n})] \\ &+ (\hat{\alpha} \cdot \hat{\mathbf{e}}_a^y)(\hat{\beta} \cdot \hat{\mathbf{e}}_b^z) \sin \eta_a \cos \eta_b \sin[\mathbf{Q}(\mathbf{r} + \mathbf{m})] \\ &+ (\hat{\alpha} \cdot \hat{\mathbf{e}}_a^z)(\hat{\beta} \cdot \hat{\mathbf{e}}_b^x) \cos \eta_a \sin \eta_b \cos[\mathbf{Q}(\mathbf{r} + \mathbf{n})] \\ &+ (\hat{\alpha} \cdot \hat{\mathbf{e}}_a^z)(\hat{\beta} \cdot \hat{\mathbf{e}}_b^y) \cos \eta_a \sin \eta_b \sin[\mathbf{Q}(\mathbf{r} + \mathbf{n})] \\ &+ (\hat{\alpha} \cdot \hat{\mathbf{e}}_a^z)(\hat{\beta} \cdot \hat{\mathbf{e}}_b^z) \cos \eta_a \cos \eta_b. \end{aligned} \quad (\text{D.2})$$

Because we have to sum over all lattice vectors \mathbf{r} , we can use the completeness relation of the Fourier transformation to simplify this expression. In the expression of the coupling $S_a^\alpha S_b^\beta$ there are mixing terms of cos and sin functions. The pure cos and sin terms can be expressed as in the following,

$$\sum_{\mathbf{r}} \cos[\mathbf{Q}(\mathbf{r} + \mathbf{m})] = \frac{1}{2} \sum_{\mathbf{r}} \left(e^{i\mathbf{Q}(\mathbf{r} + \mathbf{m})} + e^{-i\mathbf{Q}(\mathbf{r} + \mathbf{m})} \right) = \frac{N}{2} \delta_{\mathbf{Q},0} (e^{i\mathbf{Q}\mathbf{m}} + e^{-i\mathbf{Q}\mathbf{m}}) = N \delta_{\mathbf{Q},0} \quad (\text{D.3})$$

and

$$\sum_{\mathbf{r}} \sin[\mathbf{Q}(\mathbf{r} + \mathbf{m})] = \frac{1}{2i} \sum_{\mathbf{r}} \left(e^{i\mathbf{Q}(\mathbf{r} + \mathbf{m})} - e^{-i\mathbf{Q}(\mathbf{r} + \mathbf{m})} \right) = \frac{N}{2i} \delta_{\mathbf{Q},0} (e^{i\mathbf{Q}\mathbf{m}} - e^{-i\mathbf{Q}\mathbf{m}}) = 0. \quad (\text{D.4})$$

The mixed cos and sin terms in (D.2) can be transformed to terms of the form (D.3) and (D.4) with the help of simple trigonometric identities. This leads to the relations

$$\begin{aligned} \sum_{\mathbf{r}} \cos[\mathbf{Q}(\mathbf{r} + \mathbf{m})] \cos[\mathbf{Q}(\mathbf{r} + \mathbf{n})] &= \frac{1}{2} \sum_{\mathbf{r}} \left(\cos[\mathbf{Q}(2\mathbf{r} + \mathbf{m} + \mathbf{n})] + \cos[\mathbf{Q}(\mathbf{m} - \mathbf{n})] \right) \\ &\stackrel{(D.3)}{=} \frac{N}{2} \left(\delta_{2\mathbf{Q},0} \cos[\mathbf{Q}(\mathbf{m} + \mathbf{n})] + \cos[\mathbf{Q}(\mathbf{m} - \mathbf{n})] \right), \end{aligned} \quad (D.5)$$

$$\begin{aligned} \sum_{\mathbf{r}} \sin[\mathbf{Q}(\mathbf{r} + \mathbf{m})] \sin[\mathbf{Q}(\mathbf{r} + \mathbf{n})] &= \frac{1}{2} \sum_{\mathbf{r}} \left(-\cos[\mathbf{Q}(2\mathbf{r} + \mathbf{m} + \mathbf{n})] + \cos[\mathbf{Q}(\mathbf{m} - \mathbf{n})] \right) \\ &\stackrel{(D.3)}{=} \frac{N}{2} \left(-\delta_{2\mathbf{Q},0} \cos[\mathbf{Q}(\mathbf{m} + \mathbf{n})] + \cos[\mathbf{Q}(\mathbf{m} - \mathbf{n})] \right), \end{aligned} \quad (D.6)$$

and

$$\begin{aligned} \sum_{\mathbf{r}} \sin[\mathbf{Q}(\mathbf{r} + \mathbf{m})] \cos[\mathbf{Q}(\mathbf{r} + \mathbf{n})] &= \frac{1}{2} \sum_{\mathbf{r}} \left(\sin[\mathbf{Q}(2\mathbf{r} + \mathbf{m} + \mathbf{n})] + \sin[\mathbf{Q}(\mathbf{m} - \mathbf{n})] \right) \\ &\stackrel{(D.4)}{=} \frac{N}{2} \left(\delta_{2\mathbf{Q},0} \sin[\mathbf{Q}(\mathbf{m} + \mathbf{n})] + \sin[\mathbf{Q}(\mathbf{m} - \mathbf{n})] \right). \end{aligned} \quad (D.7)$$

Using the expressions (D.3) - (D.7), the \mathbf{r} dependence of interaction term $S_a^\alpha S_b^\beta$ in Equation (D.2) vanishes if the sum over \mathbf{r} is performed. Note, there are some terms which contribute only for some special \mathbf{Q} vectors, e.g., terms where $\delta_{\mathbf{Q},0}$ vanishes for all wave-vectors except $\mathbf{Q} = \mathbf{\Gamma}$. The $\delta_{2\mathbf{Q},0}$ terms are non-vanishing for $\mathbf{Q} = \mathbf{\Gamma}$ and for wave-vector for which $2\mathbf{Q}$ is a reciprocal lattice vector and thus can be folded back to the $\mathbf{\Gamma}$ point.

For the Heisenberg-Kitaev- Γ model on the hyperhoneycomb lattice discussed in Section 4, there are six types of $S_a^\alpha S_b^\beta$ interaction for each nearest-neighbor bond and in total six inequivalent bonds per unit cell. Thus, the energy of a state corresponds to a sum of 36 different terms of the type (D.2), which are weighted with the coupling constants. The sum over all lattice vectors \mathbf{r} can be performed with the help of Equations (D.3) to (D.7). This is still a function of the η_a , $\{\hat{\mathbf{e}}_a^x, \hat{\mathbf{e}}_a^y, \hat{\mathbf{e}}_a^z\}$ ($a = 1, 2, 3, 4$) and the wave-vector \mathbf{Q} , which are the free parameters in the energy minimization.

Bibliography

- [1] W. Heisenberg, Z. Physik **49**, 619 (1928).
- [2] L. Capriotti, A. E. Trumper, and S. Sorella, Phys. Rev. Lett. **82**, 3899 (1999).
- [3] A. Kitaev, Annals of Physics **321**, 2 (2006).
- [4] H. Takagi, T. Takayama, G. Jackeli, G. Khaliullin, and S. E. Nagler, Nature Rev. Phys. **1**, 264 (2019).
- [5] A. Banerjee *et al.*, Nat. Mater. **15**, 733 (2016).
- [6] G. Jackeli and G. Khaliullin, Phys. Rev. Lett. **102**, 017205 (2009).
- [7] S. Trebst, arXiv:1701.07056.
- [8] S. M. Winter, A. A. Tsirlin, M. Daghofer, J. van den Brink, Y. Singh, P. Gegenwart, and R. Valentí, J. Phys.: Condens. Matter **29**, 493002 (2017).
- [9] X. Zhou, H. Li, J. A. Waugh, S. Parham, H.-S. Kim, J. A. Sears, A. Gomes, H.-Y. Kee, Y.-J. Kim, and D. S. Dessau, Phys. Rev. B **94**, 161106 (2016).
- [10] Y. Singh and P. Gegenwart, Phys. Rev. B **82**, 064412 (2010).
- [11] S. C. Williams, R. D. Johnson, F. Freund, S. Choi, A. Jesche, I. Kimchi, S. Manni, A. Bombardi, P. Manuel, P. Gegenwart, and R. Coldea, Phys. Rev. B **93**, 195158 (2016).
- [12] A. Biffin, R. D. Johnson, S. Choi, F. Freund, S. Manni, A. Bombardi, P. Manuel, P. Gegenwart, and R. Coldea, Phys. Rev. B **90**, 205116 (2014).
- [13] A. Biffin, R. D. Johnson, I. Kimchi, R. Morris, A. Bombardi, J. G. Analytis, A. Vishwanath, and R. Coldea, Phys. Rev. Lett. **113**, 197201 (2014).
- [14] L. Janssen and M. Vojta, J. Phys.: Condens. Matter **31**, 423002 (2019).
- [15] E. K.-H. Lee, R. Schaffer, S. Bhattacharjee, and Y. B. Kim, Phys. Rev. B **89**, 045117 (2014).
- [16] S.-B. Lee, E. K.-H. Lee, A. Paramakanti, and Y. B. Kim, Phys. Rev. B **89**, 014424 (2014).
- [17] E. K.-H. Lee and Y. B. Kim, Phys. Rev. B **91**, 064407 (2015).
- [18] E. K.-H. Lee, J. G. Rau, and Y. B. Kim, Phys. Rev. B **93**, 184420 (2016).
- [19] I. Kimchi, J. G. Analytis, and A. Vishwanath, Phys. Rev. B **90**, 205126 (2014).
- [20] I. Kimchi, R. Coldea, and A. Vishwanath, Phys. Rev. B **91**, 245134 (2015).
- [21] S. Ducatman, I. Rousochatzakis, and N. B. Perkins, Phys. Rev. B **97**, 125125 (2018).
- [22] I. Rousochatzakis and N. B. Perkins, Phys. Rev. B **97**, 174423 (2018).
- [23] K. A. Modic *et al.*, Nat. Commun. **5**, 4203 (2014).

-
- [24] T. Takayama, A. Kato, R. Dinnebier, J. Nuss, H. Kono, L. S. I. Veiga, G. Fabbris, D. Haskel, and H. Takagi, *Phys. Rev. Lett.* **114**, 077202 (2015).
- [25] J. Chaloupka, G. Jackeli, and G. Khaliullin, *Phys. Rev. Lett.* **105**, 027204 (2010).
- [26] J. Chaloupka, G. Jackeli, and G. Khaliullin, *Phys. Rev. Lett.* **110**, 097204 (2013).
- [27] I. Kimchi and A. Vishwanath, *Phys. Rev. B* **89**, 014414 (2014).
- [28] T. Holstein and H. Primakoff, *Phys. Rev.* **58**, 1098 (1940).
- [29] E. R. Mucciolo, A. H. Castro Neto, and C. Chamon, *Phys. Rev. B* **69**, 214424 (2004).
- [30] L. Janssen, E. C. Andrade, and M. Vojta, *Phys. Rev. Lett.* **117**, 277202 (2016).
- [31] J. Chaloupka and G. Khaliullin, *Phys. Rev. B* **92**, 024413 (2015).
- [32] S. M. Winter, Y. Li, H. O. Jeschke, and R. Valentí, *Phys. Rev. B* **93**, 214431 (2016).
- [33] L. Janssen, E. C. Andrade, and M. Vojta, *Phys. Rev. B* **96**, 064430 (2017).
- [34] C. E. Agrapidis, J. van den Brink, and S. Nishimoto, *Phys. Rev. B* **99**, 224418 (2019).
- [35] J. M. Luttinger and L. Tisza, *Phys. Rev.* **70**, 954 (1946).
- [36] D. H. Lyons and T. A. Kaplan, *Phys. Rev.* **120**, 1580 (1960).
- [37] J. G. Rau, E. K.-H. Lee, and H.-Y. Kee, *Phys. Rev. Lett.* **112**, 077204 (2014).
- [38] J. G. Rau and H.-Y. Kee, arXiv:1408.4811.
- [39] P. P. Stavropoulos, A. Catuneanu, and H.-Y. Kee, *Phys. Rev. B* **98**, 104401 (2018).
- [40] P. W. Anderson, *Phys. Rev.* **86**, 694 (1952).
- [41] T. Barnes, E. Dagotto, J. Riera, and E. S. Swanson, *Phys. Rev. B* **47**, 3196 (1993).
- [42] Z. Weihong, J. Oitmaa, and C. J. Hamer, *Phys. Rev. B* **44**, 11869 (1991).
- [43] J. G. Rau, P. A. McClarty, and R. Moessner, *Phys. Rev. Lett.* **121**, 237201 (2018).
- [44] W. G. F. Krüger, M. Vojta, and L. Janssen, arXiv:1907.05423.

Acknowledgment

First, I want to thank Matthias Vojta for offering this interesting topic and for enabling working on this master thesis.

Second, I thank Carsten Timm for being the co-proofreader of my master thesis.

In particular, I want to thank Lukas Janssen for being my first contact person for physical relevant questions. I think, our discussions have been very enlightening for both of us. He has also given me a critical feedback to an advanced version of this thesis.

I also want to thank my roommate Paul Wunderlich for general discussions about physics and technical details in \LaTeX and Mathematica.

Last, I want to thank my other roommate Stefan Koch since our discussions have also been a critical repetition of my own calculations.

Based on the results of this thesis, Matthias Vojta, Lukas Janssen, and I have written a paper [44].

Erklärung

Hiermit erkläre ich, dass ich die vorliegende Arbeit im Rahmen der Betreuung am Institut für Theoretische Physik ohne unzulässige Hilfe Dritter verfasst habe und alle verwendeten Quellen als solche gekennzeichnet habe.

Wilhelm G. F. Krüger
Dresden, Oktober 2019